DNA-assisted Heterogeneous Integration of Micro- and Nanoelectronic Devices: Modeling, Control, and Rational Design of Selective Attachment

by

Joshy Puthenparambil Yesudas

A thesis submitted in partial fulfillment of the requirements for the degree of

Doctor of Philosophy

in

Microsystems and Nanodevices

Department of Electrical and Computer Engineering
University of Alberta

Abstract

Heterogeneous integration is an electronic packaging approach that enables the fabrication and assembly of complete electronic subsystems from components fabricated with different substrates and processes. Current commercial techniques like robotic pick-and-place, fluidic self-assembly, and flip-chip bonding limit the size of parts to the 100 μm scale. Materials in the micro-and nanoscale exhibit novel characteristics (optical, magnetic, chemical, and electrical) and thereby have potential for a wide range of applications. This limitation can be surmounted with assembly techniques based on biomolecular approaches. This thesis describes a DNA-assisted self-assembly technique that utilizes the highly specific binding of complementary DNA strands to attach devices to specific locations on a host substrate. Commercialization of this technique will require that the process be modeled, controlled, and rationally designed. In the first part of the thesis, a modeling tool using molecular dynamics simulation and a three-dimensional molecular theory of solvation is validated and explored to study the behavior of various parameters that could influence this DNA hybridization technique. The second part of the thesis describes methods developed to fabricate the micro/nano-Si devices, attach the DNA strands to the patterned Si substrate, and characterize the DNA-assisted assembly of the devices on the substrate. The assembly of near-micron-sized Si devices is challenging, and the problems encountered during the experimental procedures are discussed. The theoretical and experimental work performed builds a basis for further research into biomolecular-assisted self-assembly and contributes to the medical, electronic, and sensing fields of research.

Preface

The main elements and results of the theoretical work in chapter 3 of this thesis is published as J. P. Yesudas, N. Blinov, S. K. Dew and A. Kovalenko "Calculation of binding free energy of double stranded oligonucleotides using MM/3D-RISM-KH approach," *J. Mol. Liq.*, 2015. I was responsible for the simulation work, data analysis as well as the manuscript composition. N. Blinov assisted with the data analysis and contributed to manuscript edits. A. Kovalenko was the supervisory author and was involved with concept formation and manuscript composition.

The main experimental work of this thesis in chapter 4 is published as "J. P. Yesudas, T. Olsen, J. Ng, A. Kovalenko, and S. K. Dew "Deoxyribonucleic acid mediated heterogeneous integration of micro- and nanoscale devices," *J. Nanosci. Nanotechnol.*, vol. 16, (7), pp. 7301-7313, 2016. I was responsible for the development of DNA attachment procedure, characterization techniques, the self-assembly experiment, calculations, data analysis and manuscript composition. J. Ng assisted in developing the procedure for fabricating of the microchips. T. Olsen performed the avidin-biotin interaction experiment and developed the front side release method for the fabrication of microtiles. S. K. Dew was the supervisory author and was involved with concept formation and manuscript composition.

Acknowledgements

I express sincere appreciation to my supervisors Dr. Steven K. Dew and Dr. Andriy Kovalenko for their excellent guidance, immense encouragement, and financial support throughout the course of this doctoral research. I thank members of the Theory and Modeling Group at the National Institute for Nanotechnology (NINT) for their kind support and guidance, and members of the Thin Film and Metallization group at the University of Alberta for their kind assistance. I am grateful to Jason Ng for his support and for assistance with experimental work in the Chemical Preparation Lab, and to Nickolay Blinov for guiding me with the MD simulation and 3D-RISM calculations. I am thankful to Trevor Olsen for his effort in developing the alternate procedures to fabricate microtiles for use in a related avidin-biotin based self-assembly method. The calculations were performed on HPC resources provided by WestGrid - Compute/Calcul Canada. I thank staff in the nanoFAB facility at the University of Alberta for giving me the training and support needed to perform micro/nanofabrication experiments, staff in ACSES at the University of Alberta for helping me to examine samples with XPS, SEM, and ToF-SIMS, and staff in the Biochemistry Lab at NINT for giving me the training to perform fluorescence microscopy. I am grateful for financial support provided by the Natural Sciences and Engineering Research Council (NSERC) of Canada. In addition, I would like to thank my family for their continuous support throughout this project.

Table of Contents

List of Tables

List of Figures

1 Introduction

1.1 Heterogeneous integration of micro/nanodevices: Overview

Advances in micro/nanofabrication technologies, like those in lithography and etching, have enabled the development of miniaturized multifunctional systems in the electronics industry. Micro- and nanoscale modules like actuators, sensors, transceivers, and devices with micro-fluidic, and optoelectronic components are applied widely in data processing, power management, medical diagnostics, and automotive industries. MEMS are used for tire pressure sensors, accelerometers for airbag sensing, and flow sensors for engines in the automotive industry and are called bio-MEMS when used in pacemakers, hearing-aids, blood pressure sensors, and drug-eluting implants.

To build heterogeneous multifunction systems using nanoelectronics, different MEMS/NEMS modules, and sensors, a reliable packaging technology is needed. Heterogeneous integration (HI) is a packaging approach in which the components of a complex system are fabricated separately under optimal conditions and then assembled to construct a functioning system [1]. Advanced devices and circuits are comprised of materials from different origins, as shown in Figure 1-1 [2].

Each component must undergo a separate fabrication process because it might contain materials or processes that are incompatible with those of other components. For example, optoelectronic components used in communications and sensing applications are mainly made of III-V semiconductor materials such

as GaAs, GaP, InAs, and InSb. On the other hand, MEMS and data processing elements are usually based on silicon and silicon compounds. Combining these capabilities onto a common substrate is very desirable, but the materials are not compatible at typical (high) processing temperatures due to decomposition, diffusion, side-reactions and melting. Hence, it is necessary to fabricate optoelectronic devices and silicon ones separately and subsequently assemble them onto a common substrate near room temperature. The size and shape of the components can make them difficult to handle and are thus limiting factors in currently available heterogeneous integration technologies.

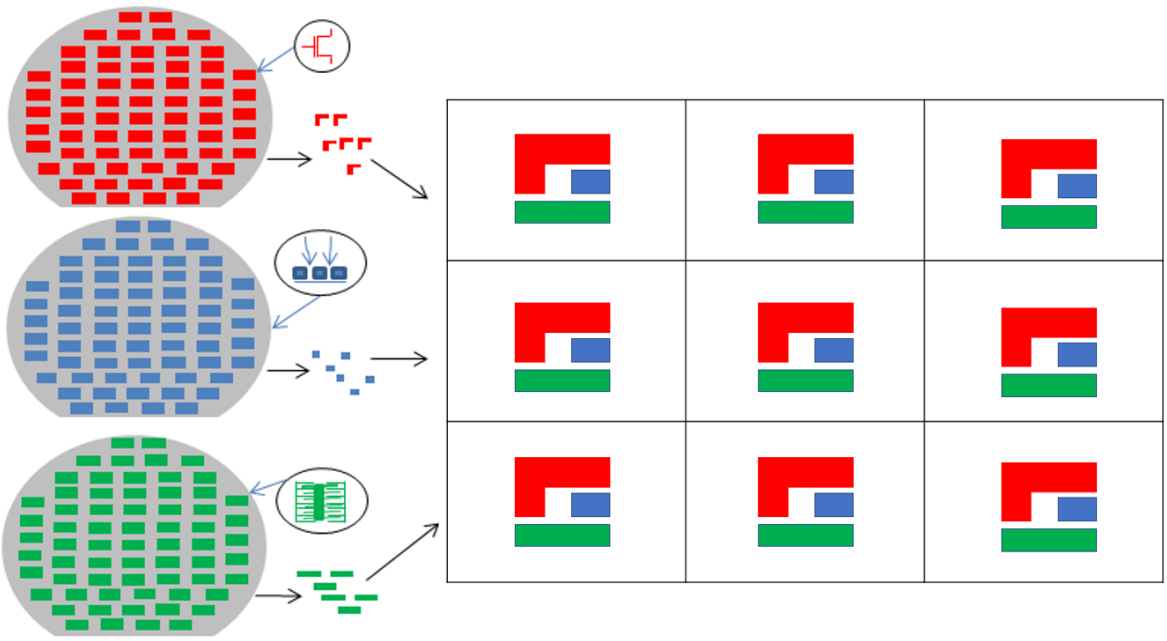

Figure 1-1 Parallel micro-assembly: Multiple microscale components for electronics, photonics, and MEMS are built in parallel using standard fabrication processes. They are positioned and combined with other components on a hybrid pallet. Based on [2].

1.2 Existing assembly techniques

Existing heterogeneous integration technologies and their advantages and disadvantages are reviewed in sections 1.2.1–1.2.3.

1.2.1 Robotic pick-and-place

Powerful pick-and-place machines equipped with advanced robotic features, including vision systems capable of distinguishing between several types of components, are used to manufacture electronic printed circuit boards (PCB) and multichip modules. In this method, the components are placed serially. Modern pick-and-place machines are capable of handling 54,000 or more surface mount electrical parts per hour with part sizes ranging from 300 μm to 80 mm (model PUMA, Essemtec, Switzerland, Figure 1-2, [3]). These machines are fast and can achieve respectable positioning accuracy (~±50 μm) over 50 cm sized (or larger) PCB boards, meaning an error that is no worse than ±0.01%. However, an error of ±50 μm on a part that is, say, only 500 μm means we now have a ±10% error. So, the limiting factor as parts continue to shrink in size is that this error of ±50 μm is constant (for a given machine) and makes the percentage error (which we could deem the precision) worse as the part size is reduced. Although there has been progress with serial handling using higher precision optical tweezers for micro- and nanoscale components [4-6], the scalability of such techniques is limited.

Figure 1-2 A robotic pick-and-place machine [3].

1.2.2 Flip-chip bonding

The flip-chip bonding [8] technique is a successful heterogeneous integration technique developed by IBM. When devices are not handled individually and are held together with an intermediate substrate or the mother substrate, bumps can be used for bonding. This technique involves using bumps to physically and electrically connect incompatible devices and substrates. Bumps can be made as small as 2–3 μm in diameter and can be as dense as a few million bumps/cm^2 (Figure 1-3). These bumps have reasonable cost and an alignment resolution of a few microns over a few centimeters. This technology allows die-level integration transfer of components fabricated in separate processes. When the bump size is kept above 10 to 15 μm, the flip-chip process has excellent yield and can lead to chip assembly at acceptable cost. The dimensions of the host chip are generally

less than a few centimeters on a side. Amkor Technology provides a flip-chip package technique [9].

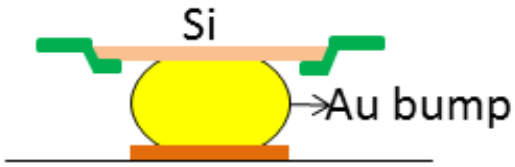

Figure 1-3 An example of a flip-chip joint using an Au bump.

The advantages of flip-chip bonding involve applicability to a large spectrum of devices and materials, testability of both mother and host substrates prior to bonding, a repeatable metallurgical process base with a well-developed pick-and-place (flip-chip aligner bonder) equipment base, a robust device performance with little degradation, and a high yield bond product. However, flip-chip aligners are limited to handling devices larger than ~ 1 mm and must operate sequentially. Moreover, the flip-chip bump introduces a parasitic capacitance which, for some applications such as fast light detection, may unacceptably dominate the receiver circuit performance. Also, the pick-and-place ability of flip-chip bonding is limited in that it can handle only chips that are at least several hundred microns on a side. These characteristics make flip-chip bonding inadequate for the anticipated needs of nanoelectronics.

1.2.3 Self-assembly techniques

The assembly rate of serial methods increases as the component size is reduced from meters to centimeters to millimeters, but decreases when the size is further reduced (Figure 1-4) [10].

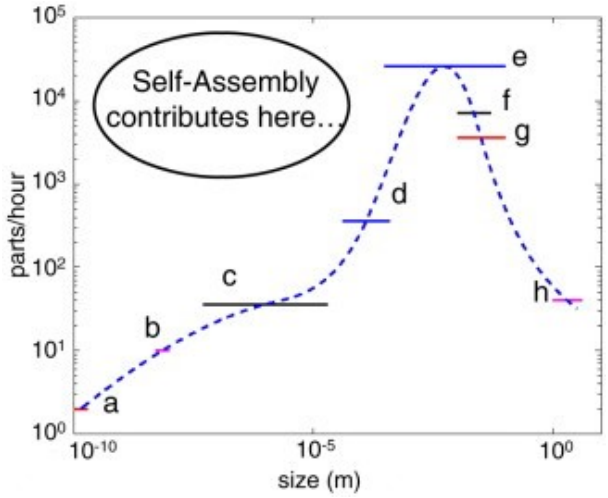

Figure 1-4 Approximate speed of assembly (in parts per hour) vs. part size for different types of assembly methods [10] © 2005, IEEE. (a) individual atom placement by scanning tunnel microscope (STM) (b) polymer memory storage device (c) optical tweezers assembly (d) 3-D microassembly (e) robotic pick-and-place printed wiring board assembly (f) robotic assembly of a grease gun coupler (g) robotic assembly of automobile wheel bearings (h) robotic assembly of an automobile body and chassis.

As the size of the components evolves to even smaller dimensions there is a need for self-assembly to overcome the limitations of current integration. Self-assembly is defined as the "spontaneous organization of molecules or objects into stable aggregates under equilibrium conditions" [11]. In a self-assembled approach, the parts that constitute the final system are made independently and then induced to self-assemble/self-package to form the final system. Some self-assembly techniques are described in the following sections.

1.2.3.1 Fluidic self-assembly

Fluidic self-assembly (FSA) is a self-assembly technique that enables the efficient placement of very large numbers of small components across a surface in a single operation [11, 12]. Figure 1-5 shows the schematic representation of GaAs light-emitting diodes being self-assembled onto a silicon substrate.

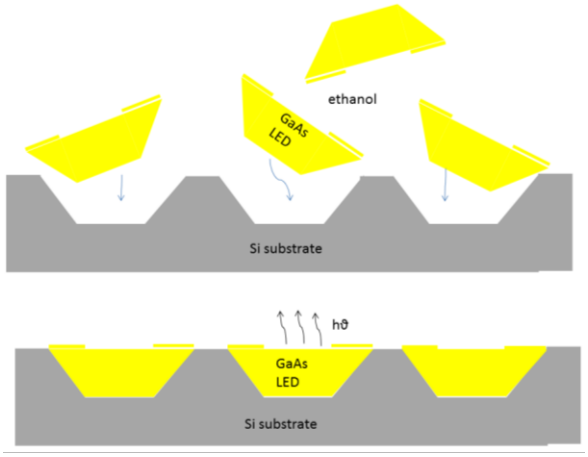

Figure 1-5 Schematic representation of gravitational force driven fluidic self-assembly of GaAs light-emitting diodes integrated onto a Si substrate.

As shown in Figure 1-5, the host substrate (Si) surface is textured with an anisotropic etch that produces ~ 10 μm deep trapezoidal holes in the surface of the Si. The devices are then suspended in an inert carrier fluid which is dispersed over the surface of the silicon substrate until the devices become trapped in the trapezoidal holes in the Si host substrate. The forces are generated via gravity and the selectivity is assured by geometric compatibility of the complementary parts. Alien Technology uses this fluidic self-assembly technique to assemble tiny integrated circuits for radio frequency identification tags at a rate of around 2,000,000 per hour [13]. FSA has the potential to fabricate densely packed III-V devices on a substrate and then sparsely integrate the devices over a larger area of the host substrate. In addition, several different types of devices can be positioned selectively in parallel. This method can be used to assemble micron sized devices. Fluidic self-assembly relies only on weak forces resulting from gravity and on simple geometric selectivity. These aspects limit the applicability of fluidic self-assembly in terms of scalability, yield, and generality.

1.2.3.2 Capillary force assisted fluidic self-assembly

In capillary force assisted fluidic self-assembly [14, 15] (Figure 1-6), the interfacial surface energy minimization between the devices and an adhesive liquid at binding sites on the substrate helps the assembly and alignment. This method is capable of arranging thousands of components per minute with sub-micrometer precision [14]. Difficulties such as tilting or rotation of parts at a binding site that can interfere with the precision of the alignment are addressed by changing parameters such as the adhesive lubricant thickness and the shape of the binding site. Jacobs et al, demonstrated various improvements and challenges associated with surface tension-directed fluidic self-assembly which uses a liquid medium for transport and utilizes the surface energy of molten solder bumps for the self-assembly of microscopic chips [16]. Recently, Xiao et al, utilized surface tension driven fluidic self-assembly along with micro pick and place methods to self-assemble photonic devices of a few hundred microns size onto a Si host substrate [17].

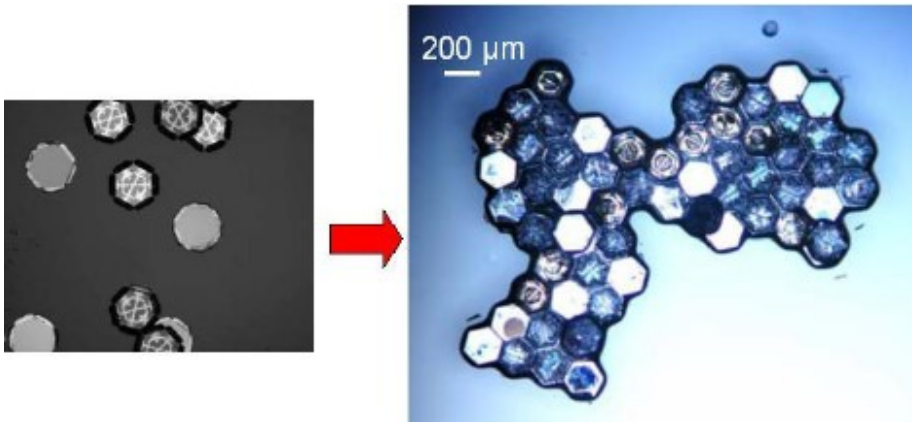

Figure 1-6 Optical microscope image of a collection of silicon components with embedded electrical interconnects supported at the air-water interface. Capillary forces have brought the elements together to form an ordered lattice [14] © 2002, IEEE.

1.2.3.3 Electrostatic force assisted self-assembly

Electrostatic forces have been used to align and position parts. Bohringer and coworkers experimentally demonstrated that small parts can be accurately positioned in parallel with electrostatic traps [2] (Figure 1-7). They showed that friction and adhesion between small parts can be overcome by ultrasonic vibration. Porta et al, applied this technique to sort metallic and glass microspheres with diameters varying from 0.6 to 1.2 mm [18].

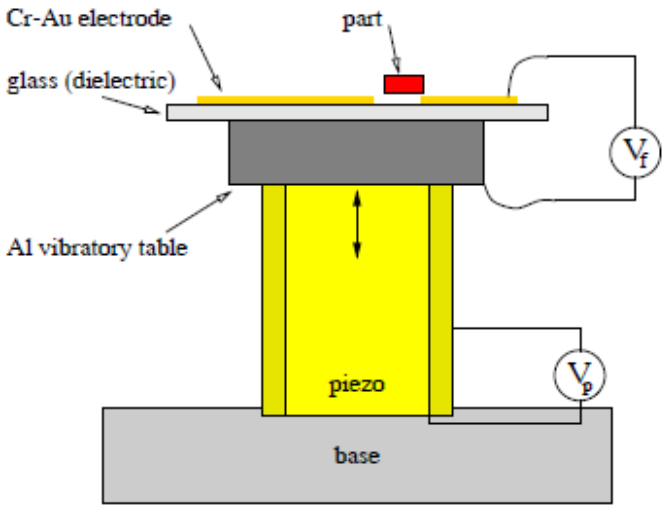

Figure 1-7 Schematic representation of an experimental apparatus for performing self-assembly using electrostatic traps. A vibratory table with a gold covered dielectric is attached to a piezoelectric actuator. The aperture in the upper electrode creates a fringing field that causes polarization in the part. The part is attracted to the aperture [2].

With a combination of dielectrophoresis (DEP) and electrohydrodynamics, silicon resistors were self-assembled with gold/chromium layers onto a template with sub-micron precision [19] (Figure 1-8). A problem with this method is the difficulty in controlling the charge on individual freestanding microcomponents.

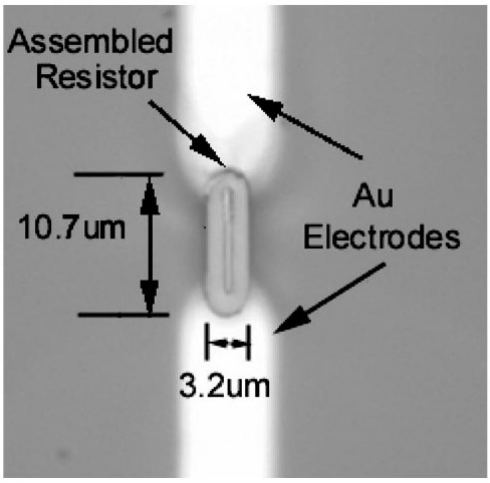

Figure 1-8 Silicon resistor self-assembled using DEP [19].

1.2.3.4 Self-assembly using DNA hybridization

Double helices of deoxyribonucleic acid (DNA) are becoming useful for molecular electronics [21-29]. Mirkin and coworkers self-assembled 13 nm sized colloidal gold nanoparticles using two complementary DNA strands [20]. The same DNA hybridization technique was exploited for the self-assembly of micro-electronic components by Esener and coworkers in 1998 [21]. There have been successful attempts to attach DNA covalently to particles and substrates [22-24, 29, 30] (Figure 1-9).

To assemble the required components, they are attached to single stranded DNA. The single stranded DNA then binds to a complementary DNA strand which is attached to the host substrate. The DNA attached to the substrate was patterned using UV light (λ = 255 nm) through a patterned mask [24]. When the components and substrate are brought together through DNA hybridization, the components are assembled on the substrate based on the pattern generated by the UV light. Multiple DNA sequences can be used to assemble multiple components, adding selectivity to the self-assembly method.

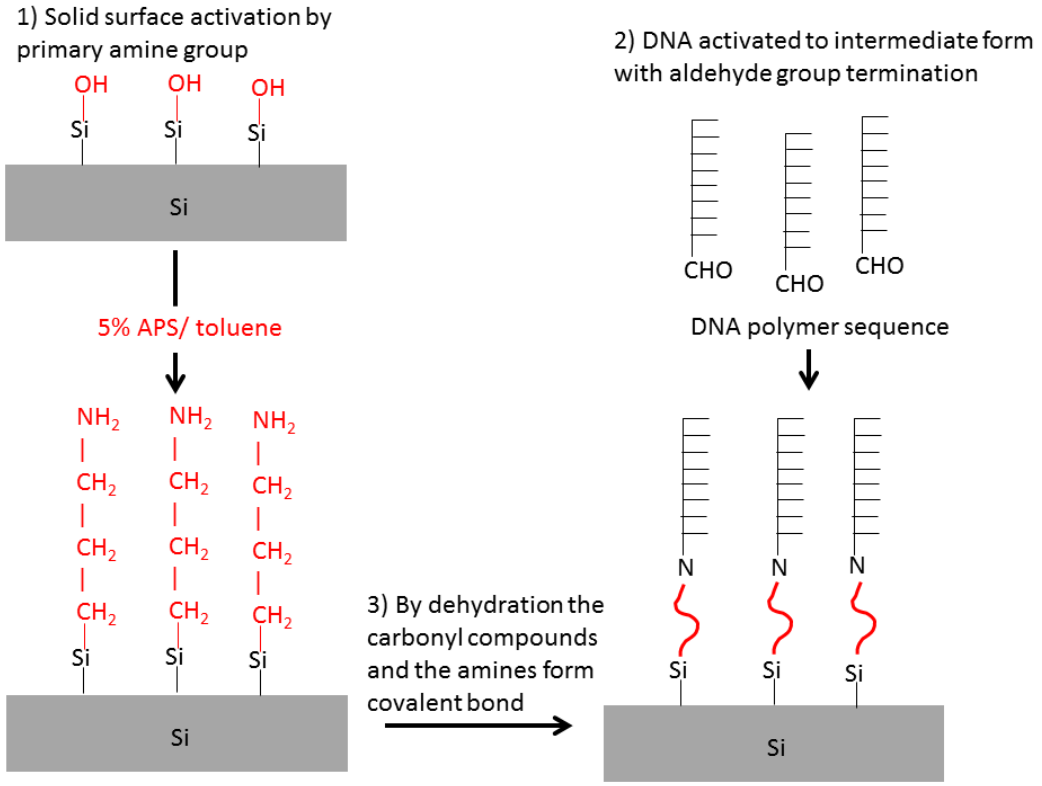

Figure 1-9 A method to attach DNA covalently to a substrate. Silicon is first treated with dilute sodium hydroxide. The materials are then derivatized for covalent coupling with the attachment sequences by treatment with 3-aminopropyl triethoxy silane (3-APTES). Dialdehyde derivative attached oligomers are bonded to the 3-aminopropyltriethoxy-silane (APS) derivatized materials in a sodium phosphate buffer [21].

It is expected that devices from 10 nm to 300 μm can be assembled using this technique [21]. In another work, the selective attachment of 0.11–0.87 μm diameter particles [24] with selective to nonselective binding ratios > 20:1 was reported; approximately 350 and 4500 DNA strands were needed to bind small and larger particles, respectively. McNally and coworkers demonstrated a method for attaching 0.8 μm diameter sized polystyrene beads onto a patterned gold surface [25]. The parts were attached to each other using DNA and an avidin-biotin system, one of the most specific protein-small molecule binding relationships known (Figure 1-10).

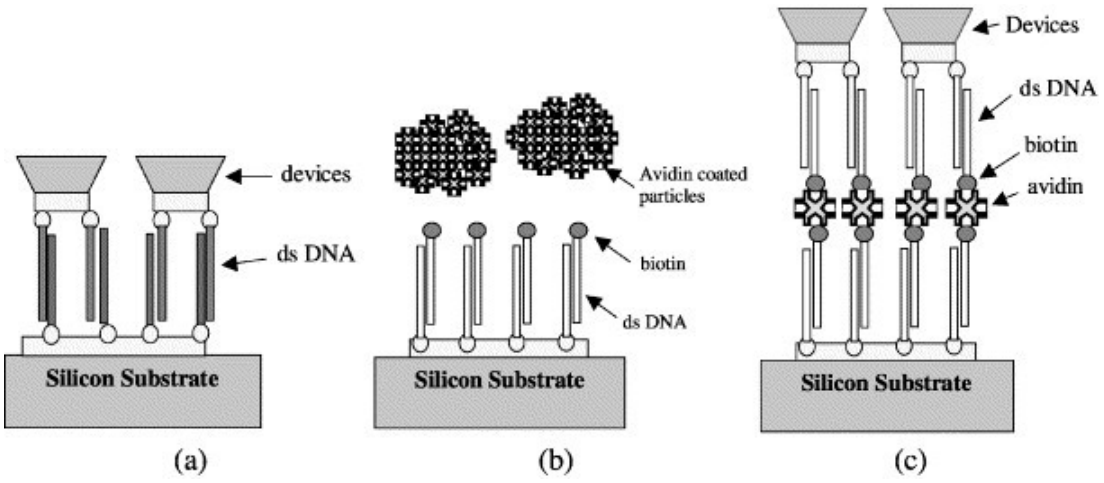

Figure 1-10 Schematic representations of biomolecule assisted self-assembly, the figures are not to scale and the actual sizes are 2-6 nm for the biomolecules and tens of nm to tens of μm for the devices. "(a) DNA on both devices and substrates, (b) use of biotinylated-DNA on substrate and avidin on particles, (c) use of biotinylated-ds-DNA on both substrate and devices and avidin as linking element" [25].

The relatively large size of proteins, and their sensitivity to pH and temperature changes, makes them less suitable than DNA for nanocomponent binding [24]. The high packing density achieved on both substrates and particles makes DNA a preferable material to realize strong particle-substrate attachment.

The feasibility of self-assembly of micro components using DNA hybridization was explored by attaching different sized polystyrene beads ranging from 1 μm to 6 μm onto glass substrates. It was found that more time is needed for the assembly as the size of the microspheres increases [27] . Alberti et al successfully assembled 1 μm sized silica beads which are denser than polystyrene beads using DNA-DNA hybridization and suggested this technique could be used to assemble electronic chips smaller than 100 μm in size [31].

Pairs of silicon micro parts were assembled successfully using the DNA hybridization technique, demonstrating the initial steps toward 3D self-assembly of Si based building blocks that could enable the construction of more complex 3D

devices in the future [25, 29]. Kim et al, demonstrated the fabrication of a metal-pentacene-insulator-silicon (MPIS) capacitor (Figure 1-11) using the formation of a self-assembled monolayer of gold nanoparticles using DNA hybridization [28]. In addition, using DNA-grafted polymer as a spacer between the micro-components and the substrate for self-assembly, researchers demonstrated the self-assembly of micro components onto gold coated Si substrates, using temperature as a control for selective self-assembly (Figure 1-12) [32] .

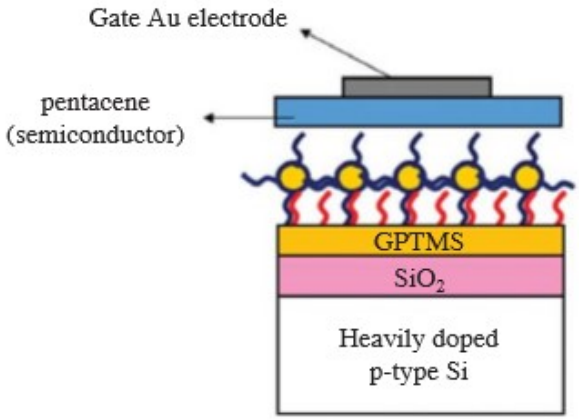

Figure 1-11 Schematic representation of the MPIS capacitor fabricated by Kim et al [28]. In this approach, the pentacene layer is deposited by evaporation on top of the gold nanoparticles (5 nm size) which are self-assembled using DNA hybridization.

DNA polymers are inexpensive and can be rapidly and efficiently synthesized with automated instruments. They can be both covalently and noncovalently linked to solid surfaces including glass, metals, silicon, organic polymers, and biopolymers and they are compatible with solvents such as acetone that are used in microfabrication. Thus, DNA-assisted micro-assembly promises to be a cost effective and fast self-assembly technique in the near future. However, the use of this technique to assemble multiple components has so far been unsuccessful, for

example, with two types of components using two different sequences of DNA strands [24].

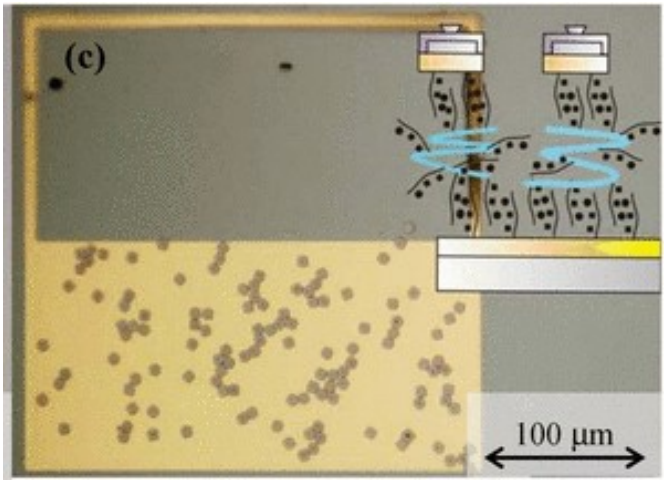

Figure 1-12 Optical photomicrograph of an assembly experiment using DNA-grafted polymer as a spacer between components and the substrate [32] © 2009, IEEE.

Research is required to fully characterize and to bridge the gap between current silicon packaging processing and biologically-assisted self-assembly [24, 25, 33]. The major challenges for DNA-assisted self-assembly are to perform the assembly of the devices onto a substrate patterned with probe DNA strands, and to demonstrate the selective binding using technologically relevant silicon devices rather than polystyrene beads. There are many successful demonstrations of DNA-assisted self-assembly of nano-particles suspended in solution [20, 25, 27] but when the assembly of the micro/nano sized flat silicon parts onto a flat macroscopic substrate is different and more challenging. Non-parallel surfaces and nonselective binding or partial hybridization between noncomplementary DNA strands leads to undesired binding (Figure 1-13).

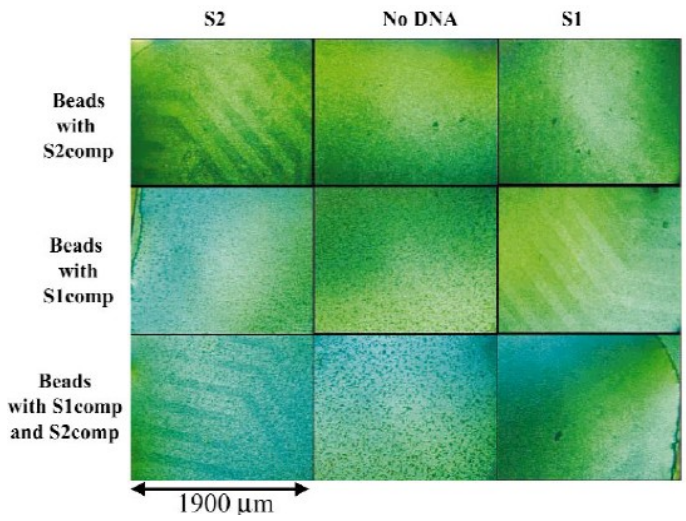

Figure 1-13 Image (using bright-field, transmitted light, DIC) of 0.87 µm diameter polystyrene beads patterned on substrates using selective DNA attachment [24]. The three rows show pictures of three different substrates. Right column: right side of substrates with a DNA sequence S1. Middle column: middle portion of substrates with no DNA. Left column: left side of substrates with DNA sequence S2. Top row: complementary DNA strand of S2 (S2comp)-labeled beads hybridize only to the left side. Middle row: complementary DNA strand of S1 (S1comp)-labeled beads hybridize only to the right side. Bottom row: complementary DNA strands S1- and S2-labeled beads hybridize only to the left side.

A need has been identified to fully characterize DNA-assisted microassembly and extend the technique to the self-assembly of nanocomponents on a common substrate. The progress in this DNA-based assembly technique depends on improved understanding of the mechanisms of DNA self-assembly and control over the hybridization [32, 34]. Factors to explore include ensuring adequate binding and preventing non-specific binding (attachment between surfaces not coated in complementary DNA pairs). Understanding the control mechanism of self-assembly will reduce error rates, improve yield and make the technique more efficient. Factors like surface density of attached DNA, salt concentration, temperature, and oligonucleotide length influence the DNA attachment. Surface density and orientation of DNA tethered to the solid surface will be critical for success but could be limited due to steric hindrance and non-complementary

binding. Unlike Mirkin's experiment [20], the DNA strands need to be in contact with the DNA functionalized surface of the substrate. Growing ordered and patterned structures of DNA strands and performing hybridization with another existing complementary DNA pair already tethered to a device is challenging. Hence, understanding the hybridization kinetics of the attachment of the DNA strands is important.

In brief, the validation of the concept of using DNA to attach pieces together has been achieved, but only for nanoparticles and microspheres. However, it has not been demonstrated for micron-sized blocks of silicon where parallel surfaces must come together flat. As well, no one has explored the limitations of the process, nor the factors that affect speed, accuracy, repeatability, yield, reliability. In addition, the issue of non-specific binding of the DNA strands is a hindrance for the application of this technique to assemble multi-components. Moreover, there is a need to identify the key variables and factors that have to be explored like surface preparation, density and orientation of DNA, length of the sequence, geometry (flatness and size), steric hindrance, temperature, time, ion concentration and pH, factors affecting non-specific binding, contaminants and cleanliness, and annealing conditions. Further, there is a need to develop various characterization methods to assess success of the process at every step.

1.3 Objective of the thesis

In this thesis, the primary objective is to extend the technique of DNA-assisted self-assembly by experimentally developing a process sequence leading to the first ever validation of DNA attachment of a technologically relevant block of silicon

from a patterned wafer. This helps to take another research step by validating the concept of DNA-assisted self-assembly using Si model devices rather than using micro-beads or nanoparticles which could provide us insight into various challenges and procedural limitations arising for further development of this technique in the electronics packaging industry.

Additionally, in this present work a set of appropriate characterization techniques will be developed to understand the state of the surfaces/system at each step of the process sequence developed. This will be critical for the assessment of yield at each process step involved and for any subsequent improvement.

Finally, development of some theoretical tools will help better understand the state of the process and explore some of the vast parameter space. In this work, a theoretical modeling tool using the MM/3D-RISM-KH (Molecular Mechanics and three-dimensional Reference Interaction Site Model using Kovalenko-Hirata Closure) approach will be introduced to calculate some of the key thermodynamic parameters like binding free energy, temperature and salt concentration effect on the ds-DNA strands. This model is validated against other similar approaches like continuum solvation models. This is an initial exploration, and will leave to others for the full validation and optimization task.

1.4 Organization of the thesis

This Chapter has provided an introduction to heterogeneous integration technology; applications to micro/nanoelectromechanical systems (MEMS/NEMS) are described. Advantages and disadvantages of commercially

available assembly techniques are reviewed and the need for self-assembly techniques is discussed in terms of the types currently available and their limitations. The current state of the art of of DNA-assisted self-assembly is reviewed.

In chapter 2, the fundamentals of DNA-assisted self-assembly are explored. The properties of DNA, especially DNA melting and hybridization, are explained in relation to its applications in micro/nanoelectronics. Examples of DNA attachment to a silicon substrate using a self-assembled monolayer and a gold-thiol reaction are given, and technical problems with DNA-assisted self-assembly are discussed.

The theoretical approach to heterogeneous integration technology is explained and discussed in chapter 3, starting with an introduction to molecular dynamics (MD) simulation. The theoretical modeling tool using MM/3D-RISM-KH approach to calculate the binding energy of DNA strands is validated and contrasted to other continuum solvation models like the generalized Born surface area (GBSA) method. The MM/3D-RISM-KH modeling procedure is further validated with two methods of performing MD simulation named “Run 1 MD” and “Run 3 MD”. In addition, this model is used to calculate the binding energy of the double stranded DNA used for the DNA-assisted self-assembly experiment in Chapter 4 (refer to section 3.4.6). Moreover, the role of salt concentration in DNA binding energy is discussed using the MM/GBSA method in section 3.4.7. Further, DNA melting temperature prediction using a semi-empirical tool is also discussed for the ds-DNA used in the experiment.

The principles of microfabrication, the procedures used to develop silicon micro/nanochips, and the techniques used to characterize our results are presented in chapter 4. Single-stranded DNA was attached to model Si nanochips. Si substrates were patterned to prepare the host substrate for the self-assembly experiment. Photolithography and evaporation techniques were exploited to produce the gold patterned host substrate. The stages involved in the attachment of the DNA strands to the host substrate were analyzed using physicochemical characterization techniques. The experiment is also performed using gold nanoparticles instead of Si chips to validate the DNA hybridization technique. Finally, DNA-assisted self-assembly performed using Si model devices fabricated with an alternate approach is presented.

Conclusions drawn from the theoretical modeling and experimental analyses are summarized in Chapter 5, and several possible extensions to the work are suggested for future study.

2 DNA-assisted self-assembly

2.1 The DNA molecule and its properties

Single-stranded DNA (ss-DNA) fragments generated by heating ds-DNA can bind specifically to complementary sequences of ss-DNA in a process termed hybridization. The complementary base pairs of double stranded DNA polymers provide an inherent self-organization mechanism. An adenine (A) base on one strand will hybridize only with a thymine (T) base on the other, while a guanine (G) base is complementary to a cytosine (C) base. Hydrogen bonding is the force that holds complementary bases to each other to form the double strand, which is helical in shape when all the bases in the single strands are paired. Figure 2-1 shows the structure of a ds-DNA molecule and illustrates the complementary nature of the base pairing. The complementary nature of the DNA base pairs is inherent in the hydrogen bonding properties of the base pairs, and provides a programmable alignment of micro- and even nanoscale devices. The diameter of a single strand of DNA is less than 1 nm, and that of a double strand is ~2 nm. Seeman showed that specific recognition between single strands of DNA allows them to form well-ordered nanoscale structures [42, 43]. DNA molecules are chemically very robust which is important for compatibility with solvents used in microfabrication such as acetone; their frequent use in molecular biology applications has significantly reduced the cost of these applications because large amounts of native and modified DNA molecules can be rapidly synthesized at relatively low cost.

The unique recognition and special structuring of DNA strands suggests its use for self-assembly in the frame of molecular electronics.

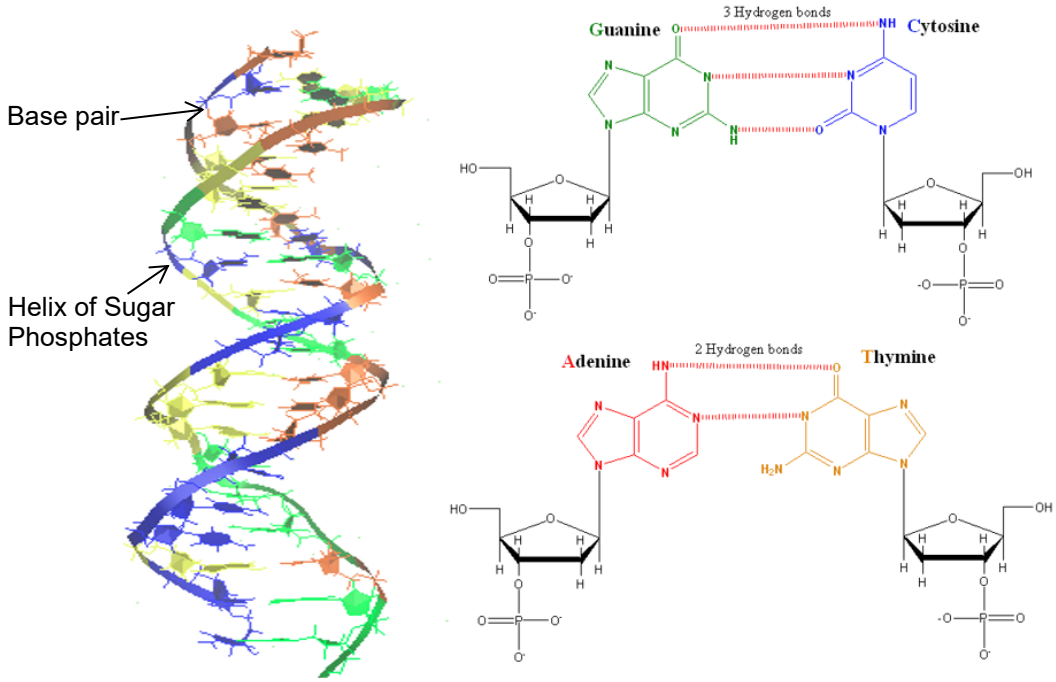

Figure 2-1 A schematic representation of the helical structure of a ds-DNA molecule and its nitrogenous bases (A)denine, (T)hymine, (G)uanine, and (C)ytosine.

Molecular recognition refers to the capability of a molecule to form selective bonds with other molecules or substrates, based on the information stored in the structural features of the interacting partners. Self-assembly, the capability of molecules to spontaneously organize themselves into supramolecular aggregates under suitable experimental conditions can drive the design of well-structured systems [44]. Molecular recognition processes can play a key role in molecular devices by (a) driving the fabrication of devices and integrated circuits from elementary building blocks, (b) incorporating devices into supramolecular arrays, (c) allowing for selective operations on given species that potentially act as

dopants, and (d) controlling the response to external perturbations represented by interacting partners or applied fields.

2.1.1 Electrical properties of DNA

DNA has been reported to demonstrate proximity-induced superconducting [46, 48, 49], insulating [50-52], and semiconducting [54, 55] behavior and therefore is a good candidate electrical material for molecular devices. Proximity-induced superconductivity (the penetration of the superconducting state into an adjacent normal conductor) has been observed when DNA molecules were deposited across two superconducting electrodes in a transport experiment [45, 48]. Each DNA molecule possesses an inherent energy level and the electric state of DNA can be controlled by the base sequence. Depending on the energetics of the DNA base sequence and on the overall structural aspects of the system under investigation, several DNA conducting mechanisms have been proposed [56-59].

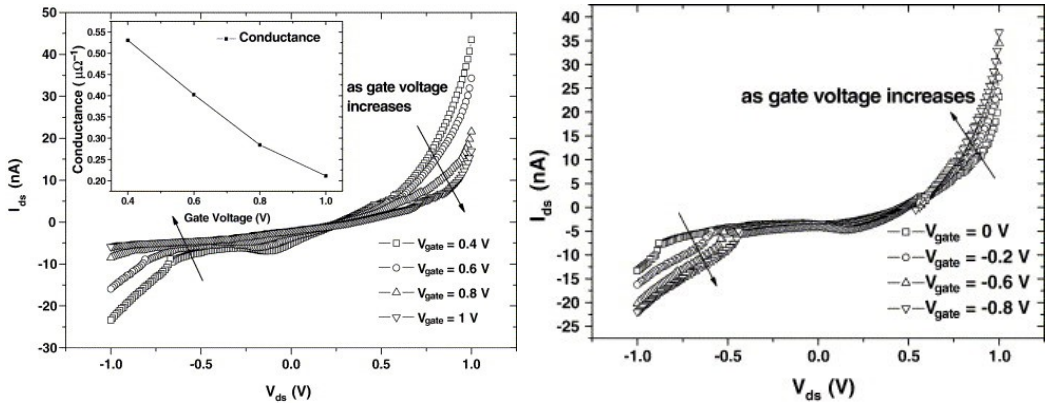

(a) (b)

Figure 2-2 (a) Effect of positive gate voltage on the source drain current, I_{DS}, of poly(dG)-poly(dC) DNA. (b) The effects of negative gate voltage on the IDS of poly(dG)-poly(dC) DNA. The current level decreases as the magnitude of negative gate voltage increases [60].

Recognition of the inherent ability of DNA to carry charge promulgated an interest in using the DNA molecule for nanoelectronics. The effect of gate voltage on the characteristics of source-drain current through DNA molecules has been studied (Figure 2-2) [60] by Kim *et al.* who suggested that a DNA poly (dG)-poly (dC) long chain with G-C base pairs acts as a p-type semiconducting material and a DNA poly (dA)-poly (dT) long chain with A-T base pairs behaves as an n-type semiconducting material under the influence of gate voltage. This confirmed the possibility that poly (dG)-poly (dC) and poly (dA)-poly (dT) DNA might be used to fabricate a nanometer scale field effect transistor.

2.1.2 Ability of DNA to form DNA superstructures

Recently, novel DNA nanostructures have been utilized for self-assembly as well as for templates in the fabrication of functional nanopatterned materials. H. Yan and coworkers from Duke University prototyped a DNA “cross structure” (Figure 2-3) with 4-fold symmetry that self-assembles into tetragonal 2D lattices and utilized the tetragonal 2D lattices as templates for highly conductive metallic nanowires [61] . DNA lattices can also be used to scaffold assembly of nanoelectronic components, especially metallic nanoparticles, which can help in the development of nanomechanical devices. The DNA nanotube is a new self-assembling superstructure composed of DNA tiles. Triple-crossover (TX) tiles modified with thiol-containing ds-DNA stems projected out of the tile plane were utilized as the basic building block (Figure 2-4) [61].

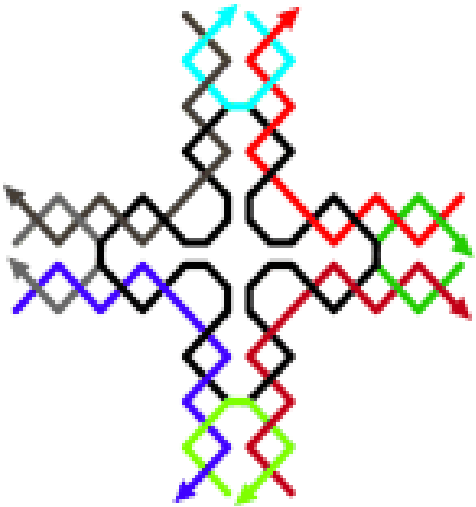

Figure 2-3 Strand structure of the cross DNA nanostructure [61].

DNA nanotubes represent a potential breakthrough in the self-assembly of nanometer scale circuits for electronics layout because they can be targeted to connect at specific locations on larger scale structures and can subsequently be metallized to form nanometer scale wires. Nanotubes are suitable for applications involving the interconnection of molecular scale devices with macroscale components fabricated by conventional photolithographic methods.

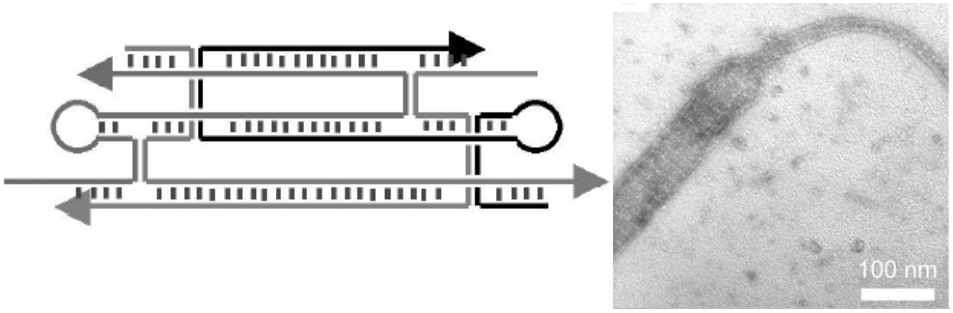

Figure 2-4 Schematic representation of a TX DNA tile utilized for the construction of the nanotube (left) and a transmission electron microscopy image (right) of a section of a TX DNA nanotube constructed using the TX DNA tile shown on left [61].

2.2 Attachment of DNA to surfaces

DNA polymers can be both covalently and noncovalently linked to solid surfaces such as glass (SiO_2), silicon (Si), metals (Au, Ag, Al), organic polymers, and biopolymers. Covalent DNA attachment can be achieved with the use of chemical reactions.

2.2.1 DNA attachment using carbinolamine formation

Glass, silicon, and aluminum can be prepared for DNA attachment in the following manner [21]. Glass and silicon are first treated with dilute sodium hydroxide (NaOH) and aluminum is treated with dilute hydrogen fluoride (HF). The materials are then derivatized by treatment with 3-amino-propyl-triethoxy-silane (APS) to activate the solid surface with amine groups. Aldehyde group terminated DNA strands are then covalently attached to the amine group terminated substrate by dehydration (Figure 1-10). The carbonyl group of the aldehyde terminated DNA reacts with the amine group of the substrate to form a carbinolamine.

2.2.2 DNA attachment using a bifunctional cross-linker

Selective covalent attachment of DNA to Si [62] is similar to the above mentioned APS method. The Si surface is reacted with (3-aminopropyl)triethoxysilane (3-APTES) to yield a self-assembled monolayer of amine groups on the Si surface (Figure 2-5) [63].

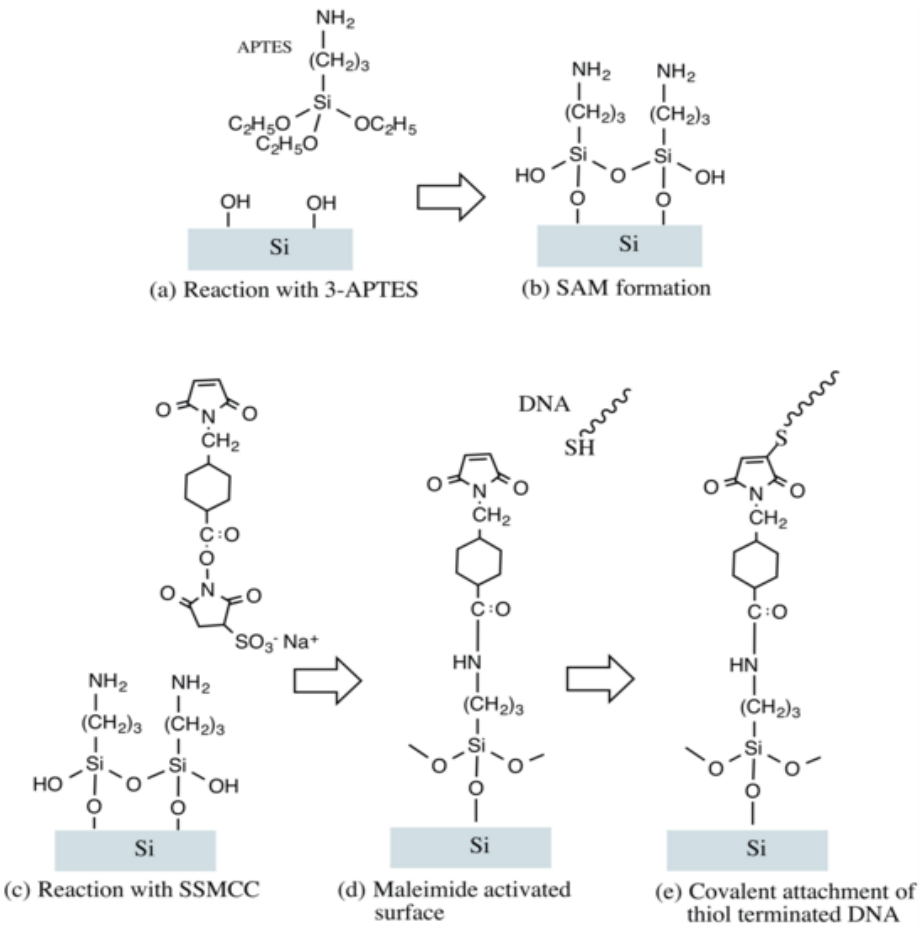

Figure 2-5 Schematic representation of the covalent attachment of DNA to a Si substrate (a) The Si surface is reacted with 3-APTES. (b) Formation of a self-assembled monolayer of 3-APTES on the Si surface. (c) The APTES-modified surface is reacted with the bifunctional crosslinker sulfosuccinimidyl 4-[N-maleimidomethyl] cyclohexane-1-carboxylate (SSMCC). (d) The maleimide-activated surface is coupled with thiol-linked DNA. (e) Formation of a DNA attached Si substrate. Based on [63] .

The APTES modified surface is then reacted with the bifunctional cross linker sulfosuccinimidyl 4-[N-maleimidomethyl]-cyclohexane-1-carboxylate (SSMCC) to activate the surface with the maleimide group. The maleimide activated surface is subsequently coupled with thiol-linked DNA leading to the covalent attachment of DNA on the Si substrate. This method was adopted in our experiments because the silicon surfaces modified by this method are more selective and stable than those prepared with other methods. Milton et al, used Undecylenic acid N-

hydroxysuccinimide ester as the linker to functionalize the Si substrate to attach the amino linked DNA molecules [64] .

2.2.3 Selective DNA attachment between SiO_2 and SiH

When dealing with multiple substrate surfaces, selectivity is a major goal. The DNA molecule can be adsorbed onto SiO_2 by adding $MgCl_2$ to an aqueous DNA solution due to the presence of Mg^{2+} ions. For a substrate patterned with SiO_2 and SiH, selective adsorption of the DNA onto the SiO_2 can be achieved by adjusting the concentration of $MgCl_2$. The selective adsorption of DNA is also based on the chemical property differences between SiO_2 and SiH [65]. $MgCl_2$ at an optimum concentration of 0.1 mM promotes the selective adsorption of DNA onto the SiO_2 surface of the SiO_2/SiH pattern.

2.2.4 Molecular liftoff process for DNA attachment

K. Sarveswaran and coworkers performed a molecular liftoff method to create a pattern called DNA rafts with high fidelity at line widths of about 100 nm [66]. Using 3-APTES aqueous solution a self-assembled monolayer (SAM) is deposited in the trench bottoms where no PMMA is present. Poly-methyl-methacrylate (PMMA), a working lithography resist, was dissolved in dichloromethane (CH_2Cl_2) for 3 min, and the surface was rinsed with water. Next, 20 µl of DNA raft solution (1 M) was deposited on the surface and left for about 4 hours. After the DNA rafts selectively attached to the APTES patterns, the surface was rinsed with water, dried with nitrogen, and imaged with atomic force microscopy (AFM).

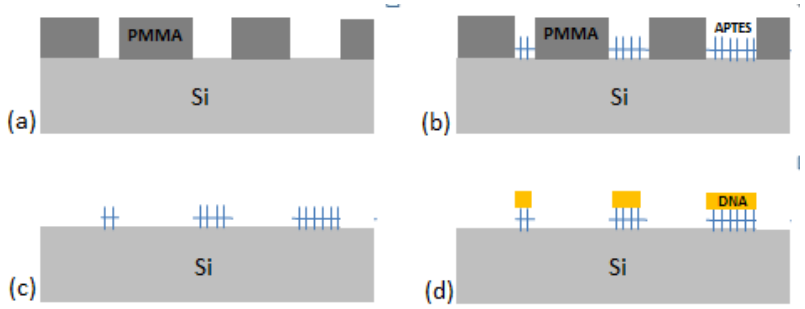

Figure 2-6 Schematic representation of the molecular liftoff process of DNA attachment [66]. (a) Formation of a pattern on the Si substrate using PMMA. (b) Treatment with APTES forming a self-assembled monolayer on the Si exposed surface. (c) Liftoff process of PMMA by dissolving with CH_2Cl_2. (d) Attachment of the DNA raft onto the SAM rich region of the silicon substrate.

A schematic representation of the molecular liftoff process for DNA attachment is shown in Figure 2-6. In this study [66], control experiments along with X-ray photoelectron spectroscopy measurements showed that APTES offers excellent adhesion and coverage uniformity on smooth SiO_2.

2.2.5 Attachment of DNA to a gold surface

Self-assembled DNA monolayers can be formed on gold surfaces using hetero bifunctional compounds anchored to gold with thiolate bonds [67]. A thiol modified DNA strand can be chemisorbed to a chemically inert gold surface through gold-thiol bonding [68]. The biological macromolecule can be derivatized by introducing thiol groups. In 1996, Mirkin and coworkers self-assembled colloidal gold nanoparticles using DNA as the linker molecules (Figure 2-7) [20]. Nowadays, thiol-modified DNA is widely used for functionalization of gold nanoparticles (AuNPs). However, the thiol-gold bond is susceptible to oxidation in air and water, resulting in compromised long-term stability.

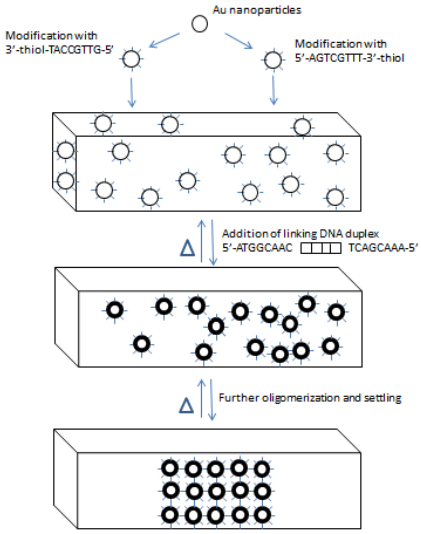

Figure 2-7 Schematic representation of self-assembly of gold nanoparticles with DNA strands using the DNA hybridization principle. Based on [20].

To attach thiol-modified DNA onto a Si substrate, a gold surface can be created on a Si substrate through an evaporation deposition process. Better adhesion of gold on silicon can be achieved by introducing a layer of chromium before depositing the Au. Thiol terminated DNA reacts with the gold surface resulting in the desired DNA attachment to the substrate (Figure 2-8).

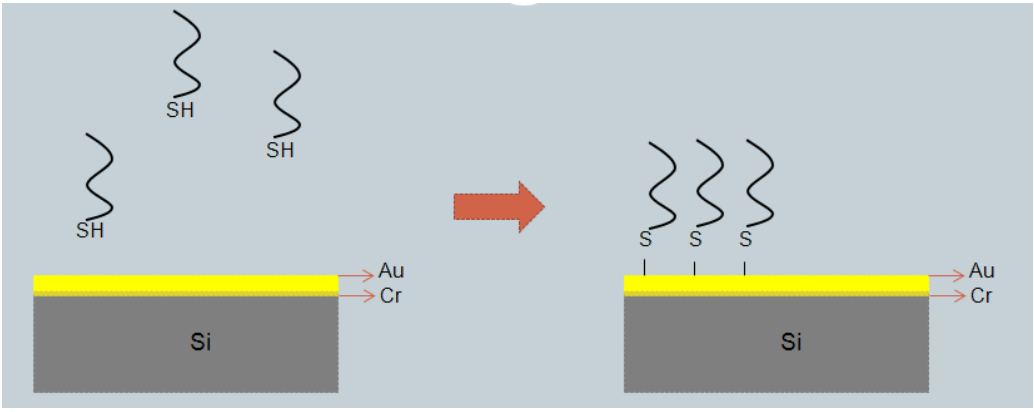

Figure 2-8 Schematic representation of the attachment of thiol-modified DNA onto a Si substrate coated with Au using thiol-gold bonding.

2.3 DNA for micro/nanoelectronics

Molecular electronics, using individual molecules as wires, switches, rectifiers, and memories, drives one of the most exciting interdisciplinary efforts in nanoscience. The Aviram-Ratner model of a molecular rectifier is considered to be the first example in molecular electronics [69]. Semiconductor devices are a fundamental paradigm of electronics at the present time, however, their miniaturization and acceleration will reach a physical limit in the future. To develop ultra-high performance devices further, it is necessary to develop nanometer sized systems. Molecular devices can be constructed by "top down" technology, which fabricates a material in a sub-micrometer or nanometer size, or "bottom up" technology in which a wide range of molecular construction is achieved by self-assembly and molecular recognition and a functional macromolecule is synthesized using an organic chemical method. In recent years there has been increasing interest in the utilization of biological tools for nanotechnological applications that are not related to biology, such as micro/nanoelectronics, micro/nanofluidics, and micro/nanoelectro-mechanical systems. Biological building blocks include proteins, peptides, nucleic acids (DNA and RNA), bacteriophages, and plant viruses. Biological molecules could be used to create nanostructures with applications in fields like electronics, telecommunication, and medical and materials engineering. A few of these applications of DNA are reviewed below.

2.3.1 Fabrication of metal nanowires

DNA's sequence specific recognition properties and related self-assembling capability might be employed to wire electronic materials in a programmable way [51, 70]. An early application of DNA for the formation of nanowires in 1998 involved the metallization of ds-DNA between two electrodes to form a conductive silver nanowire [71]. More specifically, researchers used complementary ss-DNA to bridge a 12 μM gap between two gold electrodes. The use of metal coated DNA molecules was also demonstrated for DNA-assisted wiring of gold electrodes on silicon wafers. These patterned and directed metallization schemes hold promise for novel applications in the design and manufacture of nanoelectronic devices in the future.

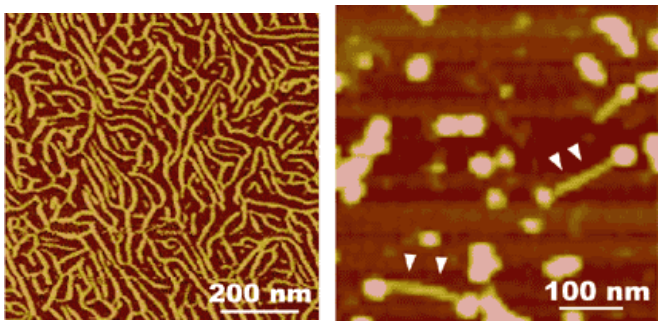

Figure 2-9 STM images of G-wires assembled under various conditions (left) and G-wires bonded to gold nanoparticles (right) [72].

G-wires are DNA superstructures based on quartet formation by four guanine (G) bases and developed using the concept of reciprocal exchange between DNA double helices or hairpins to produce branched DNA motifs, like a Holiday junction, or related structures such as double crossover, triple crossover, paranemic crossover, and DNA parallelogram motifs [72]. G-wires are interesting materials for nanotechnology due to their underlying DNA backbone, their

stiffness, and their proposed improved electrical conductivity compared to double-stranded DNA (Figure 2-9). Recently, Kondo et al, assembled silver-DNA hybrid nanowires 2 nm thick which could be applied as a thin electrical cable [73] .

2.3.2 Molecular lithography

Molecular lithography is another area of research where defined DNA sequences can be utilized for higher resolution patterning involving specific binding proteins [74]. Although lithography methods are constantly being improved, template-assisted nanowire formation may be useful for making interconnections between lithographically defined elements [75].

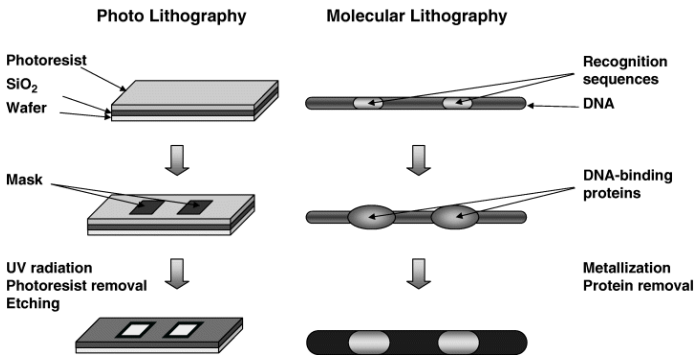

Figure 2-10: Schematic representation of the use of DNA binding proteins for 'molecular lithography.' In photolithography, a photoresist layer is deposited on the silicon dioxide surface. The use of a mask allows differential treatment of the photoresist and the etching of specific parts of the layer. In molecular lithography, the specific DNA sequence is the equivalent of a mask, and the DNA binding protein serves as the resist [76].

In the schematic representation shown in Figure 2-10, RecA, a sequence-specific DNA binding protein, was allowed to bind to a specific region on an aldehyde derivatized DNA template. The sample is then incubated in silver nitrate solution to form silver aggregates on the exposed DNA template region. The RecA protein act as a mask for the silver aggregate formation, thus serving as the equivalent of a 'resist.' As the metallization process proceeded, only non-covered

parts of the DNA molecule were coated, thus achieving a nanoscale patterned metallization of the DNA molecule.

2.3.3 DNA nanomechanical devices

Controlled mechanical movement in molecular scale devices is a key goal in nanotechnology. DNA is an excellent candidate for the construction of such devices due to its robust physicochemical properties and the specificity of the base pairing. A variety of DNA based molecular machines displaying rotational and open/close movements have recently been demonstrated [77].

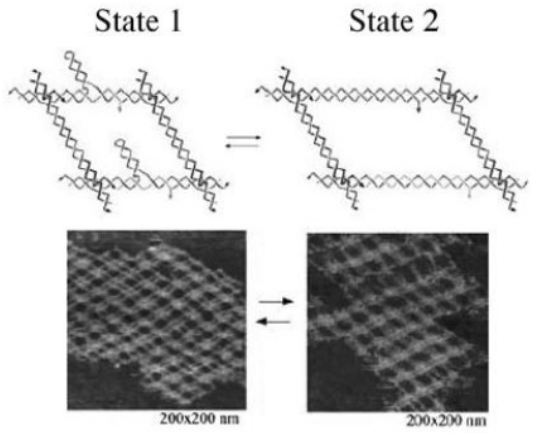

Figure 2-11 Schematic drawing of the two states of a lattice unit structure which can be called a DNA actuator [61].

Reversible shifting of equilibrium between two conformational states can be triggered by changing the experimental conditions. Incorporation of such DNA devices into arrays could lead to complex structural states suitable for nanorobotic applications if each individual device can be addressed separately. Recently, researchers constructed a nanoactuator that can exist in two states [61]. State one is a shortened state with a bulged three-arm DNA branch junction; state two is an

elongated state with two perfectly complementary strands of DNA (Figure 2-11). Bulged 3-arm DNA branch junctions have been well characterized and extensively used in DNA nano-construction and as topographic markers in self-assembly of 2D DNA lattices. Thus, a DNA device based on a bulged three-arm junction is an excellent candidate to serve as an actuator for lattices. In addition, recently Massey et al, developed DNA-based logic gates with fluorophores as a signal indicator, which could have further potential Boolean logic application in the field of biosensing [78] .

2.3.4 DNA-assisted micro/nano-assembly

As described in chapter 1, heterogeneous integration techniques refer to a body of processes and methods that are used to bring together, in a highly integrated fashion, structures at the chip (circuit) device or material levels that cannot be fabricated together using conventional processing techniques due to geometric, process or material incompatibilities. The assembly technique used to handle the structure and position it onto the host substrate, and the grafting steps, govern the reliability, applicability, and overall cost of the approach. This method can be utilized to assemble large numbers of devices of different identities using the strong forces between two complementary strands of DNA to bind the parts together [27-31, 33] . The DNA hybridization technique exploited by Mirkin and coworkers [20] to self-assemble 13 nm sized colloidal gold nanoparticles could be exploited for the self-assembly of micro components according to Esener *et al.* [21].

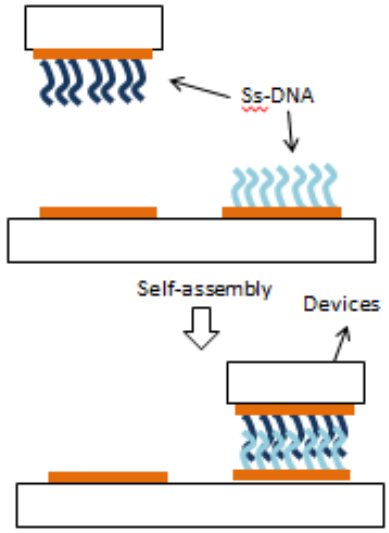

Figure 2-12 Schematic representation of DNA-assisted self-assembly of microdevices. Based on [26].

Microdevices are derivatized with a single stranded DNA that captures a complementary DNA strand attached to the host substrate. The covalent attachment of DNA to different surfaces [22, 62-65, 79] has been demonstrated. The DNA attached to the substrate can be patterned using UV light (λ = 255 nm) through a patterned mask [24] or other lithographic process. The UV light exposed DNA is damaged and loses its ability to hybridize with the complementary DNA strands. Thus, only the non-exposed DNA strands where the mask was opaque will be viable for hybridization with the complementary DNA strands. If DNA derivatized microdevices with complementary DNA bound are released in a solution above a host substrate, the DNA strands will naturally tend to hybridize resulting in the automatic self-alignment and assembly of the microdevices on the substrate (Figure 2-12. When the device components and substrate are brought together, the DNA hybridizes and the components are assembled on the substrate only at points where the complementary DNA is present.

McNally and coworkers demonstrated a similar biomolecular based method for attaching 0.8 μm diameter sized polystyrene beads onto a patterned gold surface using DNA and avidin-biotin binding (Figure 1-9) [25]. Many researchers tested this technique using gold nanoparticles as well [28, 31, 64]. DNA is less sensitive than protein to pH and temperature changes. For assembling multiple numbers of components, multiple nucleotide sequences can be used and expected to self-assemble devices from 10 nm to 300 μm in size [21].

2.4 Research Scope

Research is required to bridge the gap between current silicon packaging and biologically assisted self-assembly [24, 25, 33]. The major problem for DNA-assisted self-assembly is lack of control on the technique. There is a possibility of nonselective binding, i.e., partial hybridization can lead to binding between non-complementary DNA strands. Such undesired binding was observed when an attempt was made to attach polystyrene beads to a patterned gold surface [25] when two separate sequences of DNA strands were attempted to simultaneously bond the beads to the substrate (see Figure 1-13 for details) [24]. The researchers believed that the beads with multiple components clumped together. Since we are expecting our self-assembly technique to assemble multiple components, this problem is of major concern. One solution to these problems is simulated hybridization using annealing and agitation, which utilizes several heating and cooling cycles carried out during the hybridization process (Figure 2-13). Tanemura et al, demonstrated the application of temperature control to self-assemble multiple components by using a DNA grafted polymer between micro-

chips and a substrate and found shorter DNA lengths result in a faster self-assembly rate [32]. Also, the formation of dimers between the microchips itself is also a concern that needs to be considered [29]. During the heating cycle, weakly hybridized components are dissociated to increase the chances of the substrate DNA forming stronger bonds with the complementary DNA. This should reduce the likelihood of nonspecific binding. To gain better control over this technique it is necessary to understand mechanisms and factors contributing to DNA hybridization. Understanding role of factors like binding energy, salt concentration and temperature could help us to have more control over this technique.

Binding of the DNA strands is the basic feature behind the feasibility of the using oligonucleotides for the self-assembly of heterogeneous integration of Si micro-/nanochips. Binding energy of the DNA strands is the mechanical work needed to keep the DNA strands bound. Binding energy calculation helps us to find the strength of binding of a particular configuration of DNA strands. Since these experiments involving the DNA hybridization occur in aqueous solution, we need account for the solvation free energy for the proper calculation of the binding free energy. In this thesis, a theoretical modeling approach called MM/3D-RISM-KH is used for the first time to calculate the binding energy of the DNA strands. In chapter 3, this MM/3D-RISM-KH method is evaluated by comparing to the existing continuum solvation models.

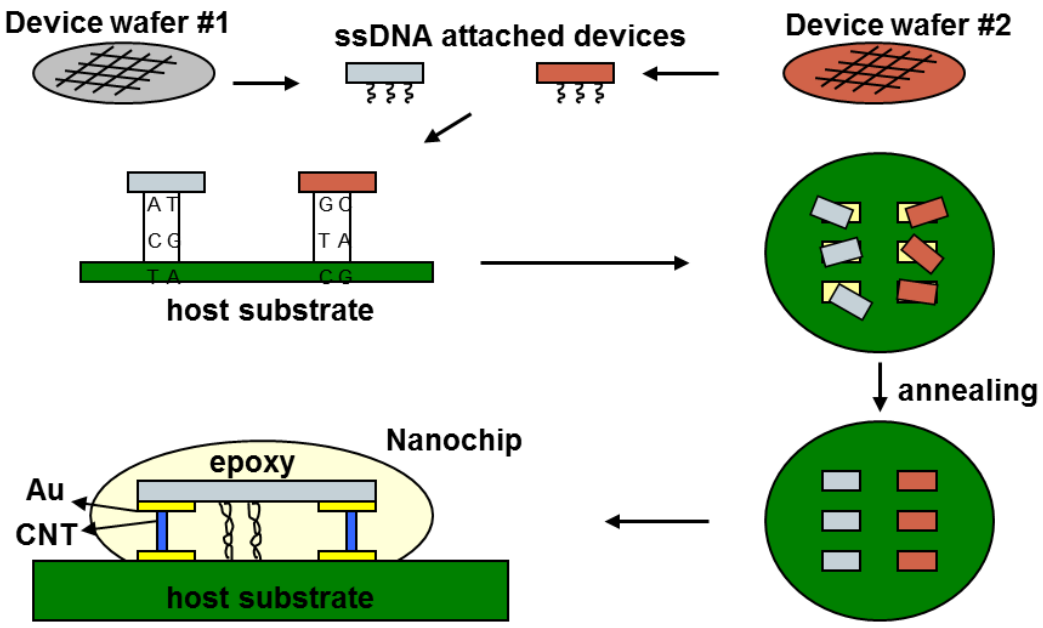

Figure 2-13 Schematic representation of DNA-assisted self-assembly of silicon devices obtained from multiple mother substrates. Each device type is derivatized with DNA of different sequence and will bind onto the host substrate patterned with the respective complementary strand. Nonspecific binding will lead to nonalignment of the devices, an undesirable situation that can be rectified using several heating and cooling cycles. Once the devices are in place by self-assembly, epoxy can be used to permanently hold them in place.

In this thesis, ds-DNA is modelled in a free state in a pure water solution. This representation could evolve further in future to resemble more closely the experimental situation of the DNA strand tethered to Si or other solid substrates and including various solvents such as hybridization buffer. In addition, this theoretical model is applied to calculate the binding free energy of the ds-DNA in free state used for the experimental work in chapter 4. Moreover, the energy values obtained are used to find a temperature range that could be used for performing the annealing step using simulated hybridization for DNA-assisted self-assembly experiments (section 3.4.6). Furthermore, the role of salt concentration is also shown for the ds-DNA used in the experimental work using MM/GBSA method and a semi-empirical tool (section 3.4.7).

Most of the DNA-assisted self-assembly reported has been attempted using various types of beads [24, 25, 27, 31] and gold nanoparticles [28, 33, 64] , but it will be very interesting to know what are the limitations and challenges ahead when this technique is applied using more realistic Si devices [29, 32, 33, 80]. In this thesis, an experimental study is conducted by performing this technique with wafer fabricated silicon-based model devices. In addition, the attachment of DNA strands on silicon and gold surfaces is experimentally tested using various characterization techniques. This experimental approach could provide more insight into the procedural requirements needed to overcome various challenges for the successful application of this technique in the micro/nano-electronic field.

The outcome of theoretical work in this thesis provides a theoretical modeling approach to calculate the binding free energy more efficiently and accurately than other approaches like continuum solvation models. There are semi-empirical tools available to predict the binding energy or the melting temperature of the free ds-DNA strands, but in our situation where the DNA strands are tethered to solid surfaces, this approach may not be reliable. Additionally, DNA-assisted self-assembly of Si micro-/nanochips has the involvements of various kinds of solvents during each experimental step. In chapter 4, we can see, the use of TCE (trichloroethylene) to dissolve the black wax, there is hybridization buffer, and occasional use of acetone as solvents. Maybe in future developments in this field there may be different types of solvent involved. In this thesis, for this theoretical model pure water with salt ions is used as the solvent for DNA hybridization, but this MM/3D-RISM-KH model can be evolved further by considering different types of solvents instead of water alone [81, 82]. Hence, this theoretical model

could advance further to be used as a potential tool to predict the parameters like temperature and salt concentration for performing simulated hybridization to avoid undesired binding for the DNA-assisted heterogeneous integration technique.

On the other hand, the outcome of the experimental study in this thesis validates the concept of using DNA strands for the self-assembly of Si model chips on to a host substrate. The experimental results should provide the various possible challenges while using Si model devices for DNA-assisted self-assembly. This experiment tests a procedure to fabricate the Si model devices and release them from the mother substrate and its effect on the subsequent steps involved in the self-assembly experiment. Similarly, it shows the various characterization techniques that could potentially be used to test the derivatization of the DNA strands onto solid surfaces like Si and Au. Moreover, this experiment could provide some insight into the role of different chemical and physical factors that need to be controlled. Further, this experiment could provide some details of selectivity and yield of assembly of Si devices using this DNA hybridization technique.

Finally, altogether this thesis should help to direct another step for future research to gain more control on the DNA based self-assembly mechanism and thereby contribute to the development of sophisticated micro/nanoelectronic devices and systems, including biological and chemical sensors, optical components and processing elements, and to reduce the time and cost of micro/nanodevice integration.

2.5 Methodologies and Rationale

Figure 2-14 is a summary of the approaches used in this project, as described in the following steps. As part of the theoretical work, (1) a theoretical model is implemented to calculate the binding free energy of the ds-DNA strands and is validated against continuum solvation models; (2) this model is used to predict the temperature range for performing simulated hybridization; (3) MM/GBSA and a semi-empirical tool is used to find the effect of salt concentration on the binding energy and melting temperature for the ds-DNA used for the experiment.

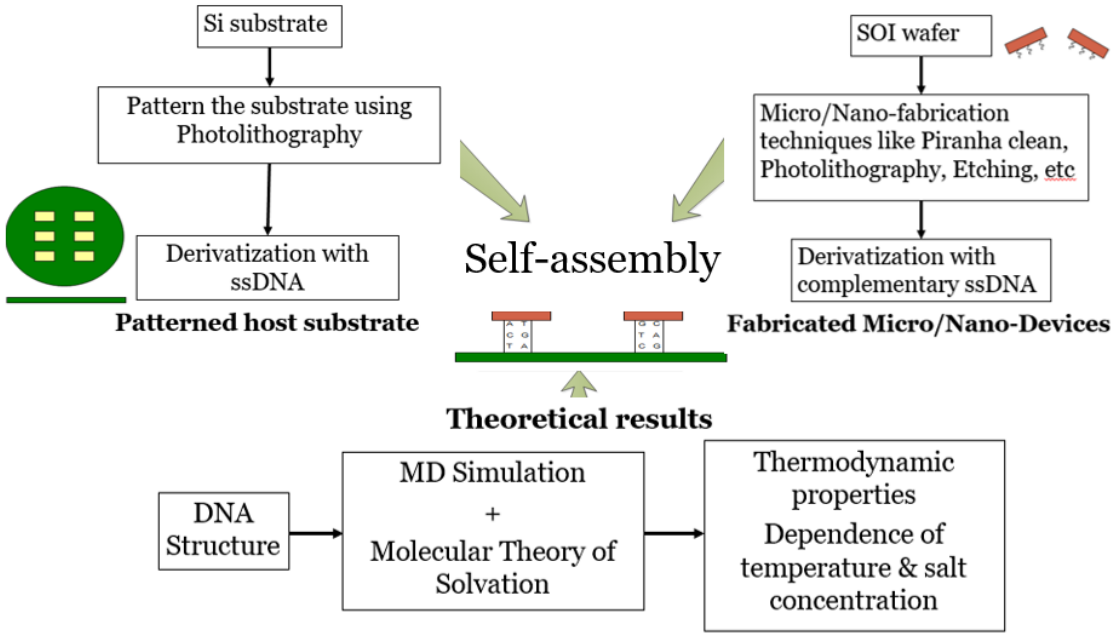

Figure 2-14 A summary of the theoretical approach and experimental work for this project.

To complement this theoretical approach, in the experimental part of the work, (1) micro/nano-techniques were utilized to fabricate devices for DNA-assisted self-assembly; (2) Si nanochips were derivatized, and photolithography was used to pattern the host substrate surface with two complementary single strands of DNA; (3) attachment of the DNA strands onto the silicon surface was verified with x-ray

photoelectron spectroscopy (XPS), fluorescence microscopy, and time-of-flight secondary ion mass spectrometry (ToF-SIMS); (4) DNA self-assembly was performed and the result was examined with optical or scanning electron microscopy.

2.5.1 Theoretical work overview

There has been considerable progress in the study of nucleic acids using molecular dynamics simulations [83-86]. Wong and Pettitt's molecular dynamics simulation of double stranded DNA (ds-DNA) on a silica surface showed that the ds-DNA on the surface had both tilted and upright conformations [84]. Molecular dynamics studies by Lee *et al*. suggested that interactions between DNA strands on a gold surface might increase the melting temperature [86] of the double helix. For this thesis, MD simulation is used to create trajectories for the energy calculations. Studies showed that both counter ions and solvent play major roles in stabilizing the double helix and determining its overall conformation [83]. So, MD simulation is performed using counter ions in water as an explicit solvent. MM/3D-RISM-KH method is used for the calculations of binding free energies of protein-ligand complexes [37, 87, 88] and is introduced in this thesis to calculate the binding free energy of ds-DNA strands. In addition, this method is validated against continuum solvation models like MM/GBSA and MM/PBSA [37, 89-91]. Studies of the behavior of counter ions in the presence of DNA showed that K^+ ions move faster than Na^+ ions [85]. MM/GBSA and MELTING [40], a semi-empirical tool, is used to find the effect of salt concentration change on binding energy and melting temperature for the ds-DNA used for the experimental part of this thesis.

More details regarding the theoretical approach and the computational results are explained in chapter 3.

2.5.2 Experimental work overview

Fabrications of Si nanochips and the patterned Si host substrate were achieved using photolithography, buffered oxide etch (BOE), and inductively coupled plasma reactive ion etch (ICPRIE). The steps involved in developing the micro/nanodevices (micro/nanotiles) for conducting the experiments were developed by Ng and Dew [92] from a 100 mm silicon-on-insulator (SOI) wafer. More information regarding this approach is provided in section 4.3.1 of chapter 4. In addition, microtiles fabricated using Olsen's method [93] are also utilized in a later stage of this project. Functionalization of the nanodevices and the host substrate by covalent attachment of DNA were achieved with the method published by Hamers *et al.* [62]. Fluorescence microscopy, time-of-flight secondary ion mass spectroscopy (ToF-SIMS), x-ray photoelectron spectroscopy (XPS), and contact angle measurements were applied to validate each step in the process of attaching the DNA strands to the devices to be aligned and to the substrate. Attachment of the self-assembled monolayer onto the Si surface was detected with XPS which detects the presence of nitrogen atoms on the surface. Binding of the bifunctional cross linker SSMCC was validated using XPS by monitoring the presence of the C=O bonds on the surface. Fluorophore-terminated (Alexafluor 546) DNA was used so that attachment of the DNA to the Si substrate could be validated with fluorescence microscopy [94, 95]. An analysis of the presence of PO_2 and PO_3 groups by ToF-SIMS was utilized to monitor the

attachment of DNA to the Si substrate. Self-assembly of the devices onto the substrate was performed using the fabricated Si model devices and gold nanoparticles for this thesis to validate this DNA hybridization technique. Optical microscopy and scanning electron microscopy (SEM) were used to obtain images to validate the self-assembly of the devices and the gold nanoparticles on the substrate. Relevant experimental methods and the results obtained are discussed in chapter 4.

3 Theoretical Study

3.1 Introduction

In order to perform the DNA-assisted self-assembly of the micro and nano-devices, it is helpful to understand the thermodynamic behavior of the DNA hybridization. In particular, it would be useful to have insight into the effect of the temperature and salt concentration on the binding of the DNA strands used for the self-assembly experiment. Understanding these dependencies on the binding and unwinding of the DNA strands will help design heating and cooling cycles and buffer solutions to increase attachment strength and selectivity.

To understand the behavior of DNA strands on thermodynamic parameters, the binding free energies which represents the mechanical work needed to keep the DNA strands in a hybridized state, need to be calculated. Molecular dynamics simulation was utilized to create the trajectories of the dynamic DNA strands and further post processing of these trajectories was done to calculate the binding free energy. Solvation energy plays a major role in calculating the binding free energy for which three-dimensional molecular theory of solvation is used.

The higher binding free energy [96] of complementary DNA strands compared to the binding of mismatched bases provides the selectivity of DNA-assisted integration of micro/nanoelectronic devices. Careful control of DNA hybridization kinetics can expand the achieved selectivity. DNA duplex stability can be predicted from the quantitative information of thermodynamic parameters [39, 97, 98]. Methods such as the nearest neighbor model [39, 99, 100] can be used to estimate

the thermodynamics of the DNA hybridization reaction but it does not consider a modified system with potentially fewer degrees of steric freedom.

Since most biological processes take place in an aqueous environment, it is important to assess the effects of solvents on the thermodynamic properties of reactions that involve these processes. Molecular dynamics simulations using explicit solvent models can accurately represent the experimental conditions; however, the calculations are computationally time consuming. In the last few years, molecular dynamics (MD) has become an important source of data regarding the structure and flexibility of DNA due to the lack of reliable experimental data [101]. The MD simulation of DNA has been performed to study nucleic acid flexibility [102], nucleic acid protein complex formation [103], and DNA functionalized gold nanoparticles [104]. Methods based on the dielectric continuum solvent approach [105-108], which considers solvent as a continuous medium rather than individual solvent molecules, involving empirical parameterization do not treat the nonpolar contribution to the solvation free energy [91, 109], which corresponds to reversible work required to insert the solute in the solvent with zero atomic partial charges.

We analyzed the thermodynamics of oligonucleotide solvation using the three-dimensional reference interaction site model (3D-RISM) with the Kovalenko-Hirata (KH) closure approximation [38, 110, 111], which can be used to describe the thermodynamics and structural properties of biological macromolecules under various solvent conditions [87, 88, 112]. According to 3D-RISM, the solvent degrees of freedom in the statistical-mechanical representation of the free energy can be partially integrated out and can then be treated in terms of the density-

density distribution functions which can be derived using Ornstein-Zernike theory [113]. A successful implementation of the KH closure approximation reproduces both electrostatic and non-electrostatic effects and features of the solvation structure. The level of description inherent in the 3D-RISM-KH theory allows one to represent solvation in terms of the three-dimensional distribution functions of solvent molecules. With much less computational effort this method accounts for solvation effects from the first principles of statistical mechanics in full molecular detail, with accuracy comparable to that of explicit solvation molecular dynamics approaches. Further, it yields the thermodynamics of macromolecule solvation, including the solvation free energy, its energy-entropy decomposition (giving access to temperature effects), and solvation volumetrics. The 3D-RISM replaces MM/PB(GB)SA post-processing that empirically describes nonpolar terms of the solvation free energy with an MM/3D-RISM-KH statistical mechanical evaluation of the solvation thermodynamics along the simulation trajectory. Molecular dynamics (MD) simulation with an explicit solvent is used to produce the conformations, and the 3D-RISM-KH molecular theory of solvation, as implemented in the Assisted Model Building with Energy Refinement (AMBER) Molecular Dynamics Package [114], is then applied to obtain the solvation free energy and thereby the binding energy of the nucleic acid strands.

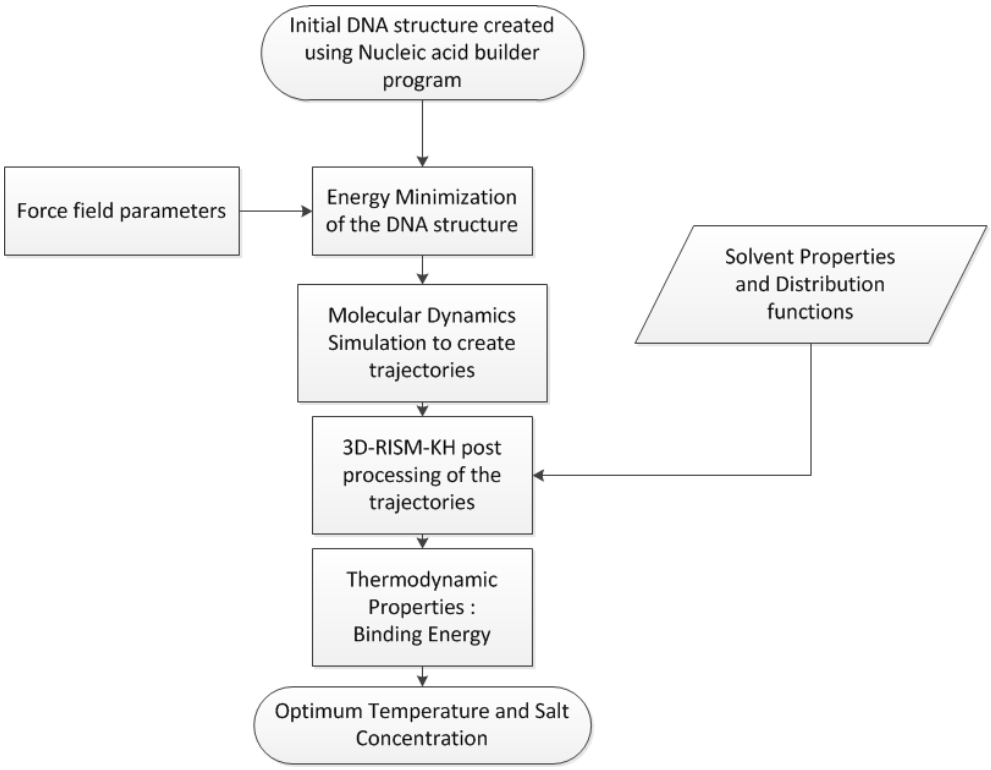

Figure 3-1 A flow chart summarizing theoretical work to obtain the optimum temperature and salt concentration for DNA-assisted self-assembly.

The flow chart in Figure 3-1 summarizes the steps involved in performing the theoretical work for this project. The initial structure of DNA is developed and force fields are applied to represent the system on which the molecular dynamics simulation will be performed to create the molecular trajectories that will be post-processed. Post-processing of the trajectories using the 3D-RISM extracts the thermodynamic properties required to calculate the binding energy of the system, thereby helping us to determine the optimum temperature and salt concentration for the DNA-assisted assembly of components on a surface. The work described in this chapter has been published in the Journal of Molecular Liquids [115].

3.2 Theoretical Background

3.2.1 Binding energy calculations

Hybridization reaction of the single stranded oligonucleotides can be represented by:

$$ss_1 + ss_2 \leftrightarrow DS \tag{3.1}$$

where ss_1 is the single strand target oligonucleotide and the ss_2 is the complementary probe oligonucleotide and DS is the complex double stranded DNA. The free energy of the reaction, ΔG_{bind}, difference between bound and unbound states of two complementary strands of ss-DNA molecules in solution is calculated from the canonical distribution:

$$\Delta G_{bind} = \langle G_{ds} \rangle - \langle G_{ss1} \rangle - \langle G_{ss2} \rangle. \tag{3.2}$$

The free energy G is estimated according to:

$$G = H - TS_{MM}\,, \tag{3.3}$$

where ΔH is the enthalpy, T is the absolute temperature and ΔS_{MM} is the entropy. The conformational entropy part TS_{MM} of the free energy is obtained using the normal mode analysis performed using the NMODE module in the AMBER package [116]. The enthalpy part H can be given by:

$$H = E_{MM} + G_{sol}, \tag{3.4}$$

where E_{MM} is the molecular mechanics total gas-phase energy and G_{sol} is the solvation free energy. So, equation 3.3 can be re-written as:

$$G = E_{MM} + G_{sol} - TS_{MM}. \tag{3.5}$$

In general, the total gas-phase energy E_{MM} can be defined as:

$$E_{MM} = E_{bonded} + E_{non-bonded}, \quad (3.6)$$

where E_{bonded} is the force relating to the atoms linked by covalent bonds which can be given as:

$$E_{bonded} = E_{bond} + E_{angles} + E_{dihedrals}, \quad (3.7)$$

and $E_{non-bonded}$ is the force of the atoms that describes the long-range electrostatics and van der Waals forces represented as the following equation:

$$E_{non-bonded} = E_{elec} + E_{vdW}, \quad (3.8)$$

where, E_{elec} is the electrostatic energy and E_{vdW} is the van der Waals energy of the DNA strands[117].

The free energy of solvation energy G_{sol} in equation 3.5 can be expressed as:

$$G_{sol} = G_{pol} + G_{np}, \quad (3.9)$$

consisting of polar (G_{pol}) and nonpolar (G_{np}) contributions. Using equation 3.5 and 3.9, equation 3.2 can be expressed as:

$$\Delta G_{bind} = \langle \Delta E_{MM} \rangle + \langle \Delta G_{pol} \rangle + \langle \Delta G_{np} \rangle - \langle T \Delta S_{MM} \rangle. \quad (3.10)$$

The solvation free energy change ΔG_{sol} was estimated using the 3D-reference interaction site model (3D-RISM) complemented with the Kovalenko-Hirata (KH) closure approximation, and the values are compared to the Poisson-Boltzmann (PB) and generalized-Born (GB) approximation methods. The Poisson-Boltzmann equation provides electrostatic potentials, solvation energies, and forces by modeling the solvent as a featureless, dielectric material, and the mobile ions as a continuous distribution of charge [109] . The nonpolar part G_{np} of the solvation energy is computed from the solvent-accessible surface area (SASA) for the PB/GB method given by:

$$G_{np} = \sigma\,(SASA) + \varphi, \qquad (3.11)$$

where σ is the solvation parameter of the atom and φ is the offset value. The popular SASA method cannot accurately describe nonpolar solvation forces at atomic length scales and may not be accurate or transferable enough for high resolution modeling studies of protein folding and binding [91].

Each of the three free energies in Equation 3.2 were calculated from three individually separate simulations, of the ds-DNA and the two single stranded DNAs, as well as simulating the ds-DNA complex and then calculating all three free energies in Equation 3.2 from the simulation. The results obtained by these two methods were compared to test the accuracy of the assumption that the conformation of the DNA strands does not change significantly upon attachment.

3.2.2 Molecular dynamics simulation

Molecular dynamics (MD) is an in-silico technique that can provide a complete description of a chemical structure and its dynamic evolution. MD simulations permit the study of complex dynamic processes that occur in a biological system, including protein stability, conformational changes, protein folding, molecular recognition, and ion transport. MD simulations have many applications, including investigation of the interaction between ions and DNA and the ion distribution around DNA. MD simulations are widely used in x-ray and NMR structure determinations. The molecular dynamics method was introduced by Alder and Wainwright in the late 1950s [118, 119] to study the interactions of hard spheres. MD simulations compute atomic trajectories by solving equations of motion using empirical force fields. Numerical integration of the equation of motion makes

possible the dynamic characterization and exploration of the conformational energy of biomolecules and their surroundings. The force field mathematically describes the actual atomic potential force the system will experience. As a result of molecular dynamics simulation, we can obtain detailed information about molecular interactions as a function of time, which can explain and complement experimental results. In this thesis, MD simulation is used to derive the dynamic evolution of the DNA structure.

MD simulation treats all atoms as classical particles and the dynamic behavior of molecules can be depicted based on Newton's second law of motion:

$$F = ma = m\frac{dv}{dt} = m\frac{d^2r}{dt^2}, \tag{3.12}$$

where m is the mass of the particle, a is the acceleration of the particle, v is the velocity of the particle and r is the position or coordinates of the atoms. The force F acting on each atom can be obtained from the potential energy $E(r)$, which is a function of all atomic positions:

$$F = -\frac{\partial E(r)}{\partial r}. \tag{3.13}$$

The potential energy $E(r)$ is usually defined by a force field developed out of a combination of pair-wise interactive terms. Force field functions are derived from quantum mechanical calculations and/or from semi-empirical or analytical forms representing physical behaviour. Then the force field parameters are optimized to fit the results of the simulation with this force field to experimental data for the physical properties of the system. The AMBER force field is widely used for the MD simulation of our DNA system. The functional form of the AMBER force field can be defined as:

$$E(r^N) = \sum_{bonds} k_b(l - l_0)^2 + \sum_{angles} k_a(\theta - \theta_0)^2 \qquad (3.14)$$

$$+ \sum_{dihedrals} \frac{V_n}{2} [1 + cos(n\emptyset - \gamma)]$$

$$+ \sum_{i<j} \left(\frac{A_{ij}}{R_{ij}^{12}} - \frac{B_{ij}}{R_{ij}^{6}}\right) + \sum_{i<j} \frac{q_i\, q_j}{4\pi\varepsilon_0 R_{ij}},$$

where $l, l_0, \theta,$ and θ_0 represent bond lengths and angles and their equilibrium values, k_b, k_a and V_n are force constant, and $\emptyset,\ \gamma,$ and n represent dihedral angles, phase shift, and periodicity, respectively. The fourth part of the equation 3.14 is the Lennard Jones potential, representing van der Waals interactions, where A and B are constants determined by the atom types of the atoms i, j involved, and R_{ij} is the distance between the atoms. The last term of equation 3.14 represent the Columbic interactions where $q_i\,, q_j$ are the partial charges of the atoms i and j, and ε_0 is the effective dielectric function for the medium.

With defined initial velocities and positions, the equation 3.13 can be integrated numerically in discrete time steps using finite difference methods for all the particles in the simulated system to yield the positions and momenta of these particles as function of time, which we call a trajectory. In particular, one of the most common is velocity Verlet which is an integration algorithm approximated by a Taylor series expansion [120]; it is used to simulate the system to determine the positions, velocities, and accelerations with time step ∂t. The velocity Verlet algorithm is given by equations and :

$$r(t + \partial t) = r(t) + v(t)\partial t + \frac{1}{2}\, a(t)\partial t^2, \qquad (3.15)$$

$$v(t + \partial t) = v(t) + \frac{1}{2}\,[a(t) + a(t + \partial t)]\partial t, \tag{3.16}$$

where r is the position, $v(t)$ and $a(t)$ are respectively the velocity and acceleration of the particle at time t.

If the system is allowed to evolve in time indefinitely, it will eventually pass through all the possible states. With these trajectories and using statistical mechanics, the average structural, dynamic, and thermodynamic properties of the system are calculated. For example, the average potential energy V is expressed as:

$$V = \langle V \rangle = \frac{1}{M}\sum_{i=1}^{M} V_i, \tag{3.17}$$

where M is the number of configurations in the molecular dynamics trajectory, and V_i is the potential energy of each configuration i. In this study, the trajectories of the DNA strands in explicit solvent and ion conditions are obtained using MD simulation and post-processed to extract the thermodynamic properties in equation 3.5 using MM/GBSA, MM/PBSA and MM/3D-RISM-KH methods to calculate the average binding energy of the strands.

3.2.3 Three-dimensional molecular theory of solvation

To calculate the solvation energy G_{sol} term in equation 3.5, 3D-RISM-KH calculations were performed on the trajectories obtained from MD simulation. Molecular theory of solvation, also known as the reference interaction site model (RISM) [121, 122] is based on the first principles foundation of statistical mechanics and Ornstein-Zernike (OZ) type integral equation theory of molecular

liquids [121]. It provides a firm platform to handle complex chemical and biomolecular systems in solution. As distinct from molecular simulations which explore the phase space of a molecular system by direct sampling, RISM theory operates with spatial distributions rather than trajectories of molecules and is based on analytical summation of the free energy diagrams which yields the solvation structure and thermodynamics in the statistical-mechanical ensemble. It yields the solvation structure by solving the RISM integral equations for the correlation functions and then the solvation thermodynamics analytically as a single integral of a closed form in terms of the correlation functions obtained.

The three-dimensional (3D) molecular theory of solvation, also known as the 3D reference interaction site model (3D-RISM), provides a detailed information on solvation shells in the form of 3D maps of the equilibrium statistical mechanical distributions of interaction sites of solvent molecules around a given solute [122] macromolecule or supramolecule. Coupled with the Kovalenko-Hirata (KH) closure relation [123], the 3D-RISM-KH molecular theory of solvation can yield solvation thermodynamic properties such as the free energy of solvation, entropy-enthalpy decomposition, and partial molar volume for biomolecules including DNA [124-128]. The 3D-RISM integral equation can be derived [123] from the six dimensional-molecular Ornstein-Zernike (OZ) equation [121] for a solute-solvent mixture. The 3D-RISM integral equation is:

$$h_\gamma(r) = \sum_\alpha \int dr'\, c_\alpha(r - r')\, \chi_{\alpha\gamma}(r'), \tag{3.18}$$

where $h_\gamma(r)$ is the total correlation function of solvent molecules site γ at the 3D space position r, which is related to the 3D site distribution function of solvent around the solute:

$$g_\gamma(r) = h_\gamma(r) + 1. \tag{3.19}$$

The 3D direct correlation function $c_\alpha(r)$ is the asymptote of the solute-solvent site-interaction potential. The site-site susceptibility $\chi_{\alpha\gamma}(r')$ of the pure solvent can be obtained from one dimensional RISM integral equation theory and is given by:

$$\chi_{\alpha\gamma}(r') = \omega_{\alpha\gamma}(r) + \rho_\alpha h_{\alpha\gamma}(r), \tag{3.20}$$

where $\omega_{\alpha\gamma}(r)$ is the intramolecular distribution function specifying the geometry of the solvent molecules, $h_{\alpha\gamma}(r)$ is the intermolecular site-site total correlation function of the bulk solvent, and ρ_α is the bulk solvent site-number density.

It is necessary to have a closure that relates to the total and direct correlation functions to complement the 3D-RISM integral equation 3.18. The general closure relation is [121]:

$$g_\gamma(r) = \exp\left[-\beta u_\gamma(r) + h_\gamma(r) - c_\gamma(r) + b_\gamma(r)\right], \tag{3.21}$$

where β is given by:

$$\beta = 1/k_B T, \tag{3.22}$$

where k_B is the Boltzmann constant, and T is the solution temperature, and $u_\gamma(r)$ is the 3D interaction potential between the whole solute molecule and solvent site γ specified by a molecular force field. The bridge function $b_\gamma(r)$ contains multiple integrals, which makes calculations cumbersome. Kovalenko and Hirata proposed a closure approximation (KH closure) given by:

$$g_\gamma(r) = \begin{cases} \exp\left(-\beta u_\gamma(r) + h_\gamma(r) - c_\gamma(r)\right) & for \quad g_\gamma(r) \le 1, \\ 1 - \beta u_\gamma(r) + h_\gamma(r) - c_\gamma(r) & for \quad g_\gamma(r) > 1. \end{cases} \quad (3.23)$$

As distinct from other closure approximations, such as the hypernetted-chain (HNC) closure, the KH closure does not have difficulties with highly asymmetric particle sizes and converges to stable solutions for all stable parts of the phase diagram. The 3D-RISM with the KH closure approximation can effectively describe the thermodynamic and solvation structural properties of biological macromolecules including DNA [125-128] and under various solvent conditions.

The 3D-KH closure underestimates the height of strong associative peaks of the 3D site distribution functions because of the MSA linearization applied to them [123, 129]. However, it somewhat widens the peaks and so 3D-RISM-KH quite accurately reproduces the coordination numbers of the solvation structure in different systems, including micro-micelles in water-alcohol solutions [130, 131] solvation shells of metal-water [38, 123] ,metal oxide-water [132], and mixed organic solvent-clay [133] interfaces, and structural water solvent localized in biomolecular confinement [128, 134]. For example, the coordination numbers of water strongly bound to the MgO surface are calculated from the 3D-RISM-KH theory with 90% accuracy and the peak positions within a 0.5 Å deviation, compared to MD simulations [132]. The 3D solvation map $g_\gamma(r)$ of function-related structural water in the GroEL chaperon complex obtained in an expensive MD simulation with explicit solvent involving ~1 million atoms is reproduced from the 3D-RISM-KH theory in a relatively short calculation on a workstation with an accuracy of over 90% correlation for the 3D density map and about 98%

correlation for the 3D density maxima. Much as with the HNC approximation, the 3D-KH closure (Equation 3.23) to the 3D-RISM integral equation (Equation 3.18) has an exact differential of the solvation free energy, and allows one to analytically perform Kirkwood's thermodynamic integration gradually switching on the solute-solvent interaction. This gives the solvation free energy of the solute macro- or supra-molecule in multicomponent solvent in a closed analytical form in terms of the 3D site total and direct correlation functions $h_\gamma(r)$ and $c_\gamma(r)$ [38, 123, 130]. The solvation chemical potential $\mu_{\text{solv}}^{\text{KH}}$ keeps an analytical form for 3D-RISM integral equation 3.18 with the Kovalenko-Hirata closure approximation (equation 3.23) given by:

$$\Delta G_{sol,3DRISMKH} = \mu_{solv}^{KH} \tag{3.24}$$

$$= \rho_\gamma k_B T \sum_\gamma \int dr \left[\frac{1}{2} \left(h_\gamma(r) \right)^2 \Theta \left(-h_\gamma(r) \right) \right.$$

$$\left. - c_\gamma(r) - \frac{1}{2} h_\gamma(r) c_\gamma(r) \right],$$

where $\Theta(x)$ is the Heaviside step function:

$$\Theta(x) = \begin{cases} 1 & for\ x > 0 \\ 0 & for\ x < 0 \end{cases}. \tag{3.25}$$

The solvation free energy $\Delta G_{sol,3DRISMKH}$ thus obtained using 3D-RISM-KH is used in equation 3.5 to calculate the binding free energy of the complementary DNA strands.

3.2.4 Recent advancements

Subsequent to the modeling work done above, there were a number of changes and advancements in the field relating to this theoretical modeling approach which were not able to be employed in this work. More optimized MD software and progressively greater computational power now aid researchers to extend conformational sampling times to the microsecond level and beyond. For creating trajectories, instead of performing one long MD simulation, other studies have observed that it is more effective to run many short independent simulations to obtain uncorrelated data [37, 135] .

The force field model is another key component which has been improved in recent years to generate accurate and stable structures of biomolecules [136]. In this thesis, ff99bsc0 is used as force field to create the ds-DNA structures; ff14sb is the improved AMBER force field recommended nowadays.

Recent research introduced a number of corrections for the solvation free energy which improved the accuracy of the prediction of solvation free energy with 3D-RISM theory and is called Universal correction (UC) [137-140]. This technique is also known as the partial molar volume correction technique, and this correction significantly improves the agreement between the calculated and experimental data for solvation free energies. In addition, this correction technique works better with 3D-RISM-KH theory for solvation free energy in a non-polar liquid [137].

For this thesis, MD simulation is performed using AMBER 10 version, but currently there is a much-improved Version 16 with better force fields, continuum solvation models, and 3D-RISM-KH theory integration. Moreover, the 3D-RISM-KH model has been integrated into the AMBER software, which made it easier to

execute sampling and calculations similar to MM/GBSA. Further, this enabled the performance of the MM/3D-RISM-KH calculations in better and faster computer resources like WestGrid.

3.3 Methods

3.3.1 Molecular dynamic simulation of ds-DNA

The aim is to find information that will complement what can be learned through the DNA-assisted self-assembly experiments. Binding energy is one of the important parameter which could provide more insight into the theromodynamic behavior of the ds-DNA strands. There are many ways to perform the MD simulation of the DNA strands and thereby calculate the binding energy using a molecular theory of solvation. To perform molecular mechanics, the generalized Born model, and the solvent accessibility method (MM/GBSA) based calculation, the MD simulation of the complex can be performed and the trajectories of the single strands from the same complex can be derived for post-processing. In this thesis this method is called as single simulation approach “Run 1 MD” since only the MD simulation for the complex is performed. Alternatively, the ds-DNA complex and the two ss-DNA strands could be subjected to an MD simulation separately. However, the alternative approach involves three separate MD simulations, this method is called as separate simulation approach (Run 3 MD).

The post-processing of the ds-DNA was done after stripping the water and the neutralizing ions (Na+) from the ds-DNA complex and from the separate single strands. Additionally, to find the best suitable procedure, the post-processing of

the trajectories by retaining the ions in the system is tested. Procedures that can be used to perform MD simulations and DNA post-processing to calculate the binding energy of ds-DNA using different approaches are summarized in Figure 3-2.

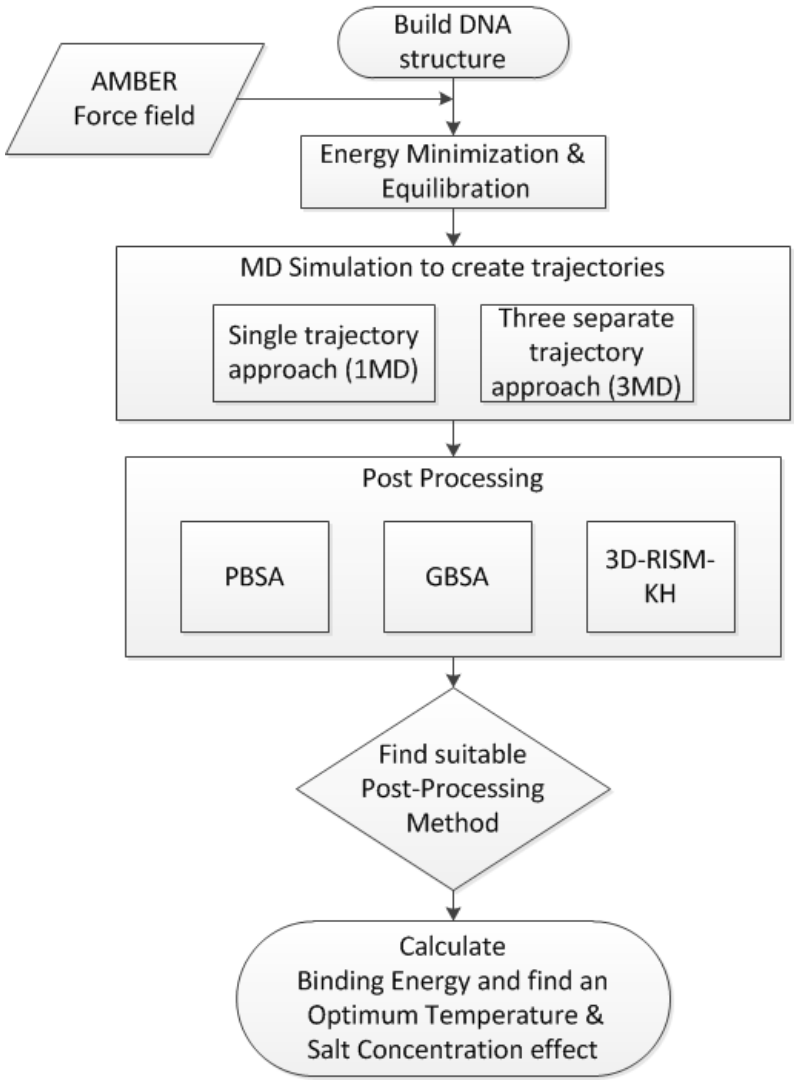

Figure 3-2 Flow chart summarizing the procedures used to perform MD simulations and DNA post-processing to calculate the binding energy of ds-DNA.

To find the best approach to calculate the binding energy of complementary DNA strands, samples of four of DNA sequences (Table 3-1) whose experimental binding energy values are available [141] were chosen. The DNA sequence

represents the primary structure of the molecule by showing the order of nucleotides within the DNA. 5′-end and 3′-end represent the chemical convention of naming the carbon atoms in the nucleotide sugar ring for each strand, designating the start and end of each DNA strand. The third sample is named pal10-mer since the sequence is a palindromic sequence. A DNA strand is said to be palindromic when its complementary strand has the reverse complement sequence. The same procedure was used for all samples; figures and intermediate results are reported only for the 10-mer.

Table 3-1 DNA sequences used for the theoretical study.

Sample	Sequence	Experimental binding energy [141] (kcal/mol)
9-mer	5'-CAAATAAAG-3'.3'-CTTTATTTG-5'	-8.5
10-mer	5'-TTGGTGATCC-3'.3'-GGATCACCAA-5'	-11.9
pal10-mer	5'-GCGAATTCGC-3'.3'-CGCTTAAGCG-5'	-15.5
20-mer	5'-AGATTAGCAGGTTTCCCACC-3'.3'-GGTGGGAAACCTGCTAATCT-5'	-40.0

A detailed list is provided below in Table 3-2 with the details of the simulation software programs used including their source details. Appendix I provides more details on the commands I used in the AMBER MD package including the input files for the MD simulation of the 10-mer ds-DNA.

Table 3-2 Details of the simulation software programs used and its source.

MD simulation package	AMBER 10
Computer resource	HPC of WestGrid

	Website: https://www.westgrid.ca/support/software/amber
Server	*Bugaboo* server System Location: Simon Fraser University Cores: 4584 Login Node: *bugaboo.westgrid.ca*
AMBER modules/program	*NAB* : build DNA structure *xleap* : generates parameter and topology files *sander* : perform energy minimization and molecular dynamics *ptraj* : read trajectories *nmode* : entropy calculations *mmpbsa.pl* : post processing using GBSA and PBSA
3D-RISM-KH calculation	program from theory and modeling group (TMG), NINT Server: TMG server NINT 4 CPU cores of 2.5 GHz Intel Xeon processor

3.3.1.1 Building 3D DNA structure

The most common B-form ds-DNA structure was constructed using Nucleic Acid Builder (NAB) in the AMBER suite. The AMBER force field ff99bsc0 was utilized. Na^+ ions were added as counter ions to neutralize the negatively charged DNA system using xleap in AMBER. Water is an integral part of all biomolecular systems, so the molecular dynamics (MD) simulation was carried out in an explicit solvent using the SANDER module in AMBER 10.

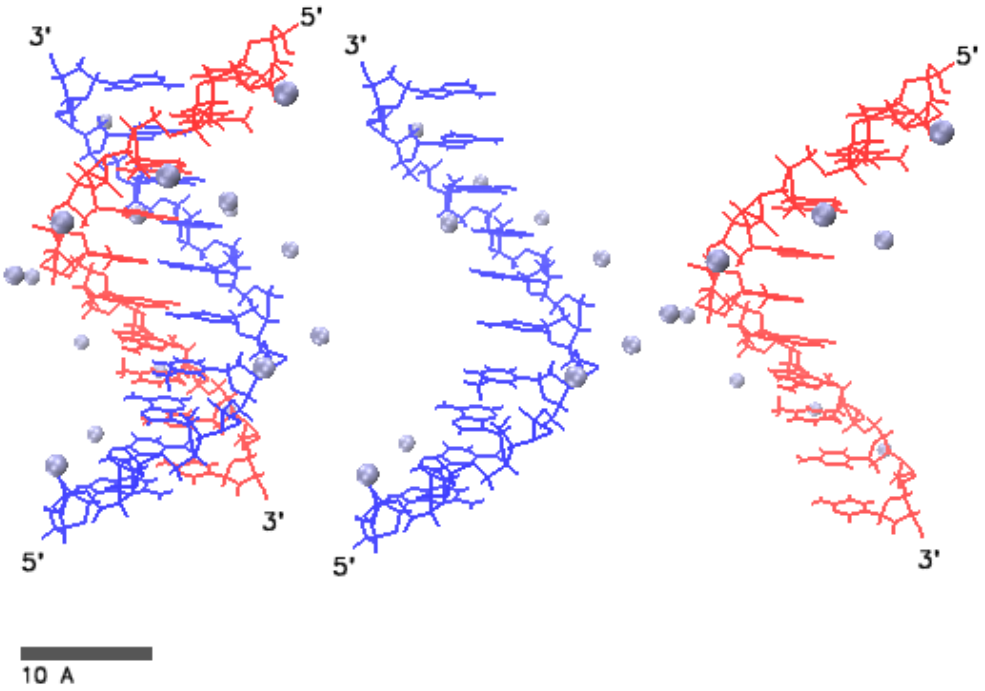

Figure 3-3 10-mer ds-DNA complex with neutralizing Na+ ions (blue spheres) prior to energy minimization. The single strand DNA, ss1 (red) and its complementary strand, ss2 (blue) are shown separately with the counter ions.

An 8 Å buffer of TIP3P water around the DNA in each direction in an octahedral simulation box was used to solvate the DNA. The addition of neutralizing ions and water destabilizes the system so the system energy was minimized to make it more stable before MD simulation was performed (Figure 3-3).

3.3.1.2 Energy minimization

Energy minimization was performed by keeping all atoms except water, counter ions, and hydrogen atoms fixed in position using positional restraints with a force constant of 500 kcal mol^{-1} $Å^{-2}$. The potential energy of the solvated ds-DNA was minimized by 500 steps of steepest descent minimization, followed by 500 steps of conjugate gradient minimization. During energy minimization, favourable

water-water and water-DNA electrostatic interactions were optimized as the water molecules reorient into geometry of lower energy.

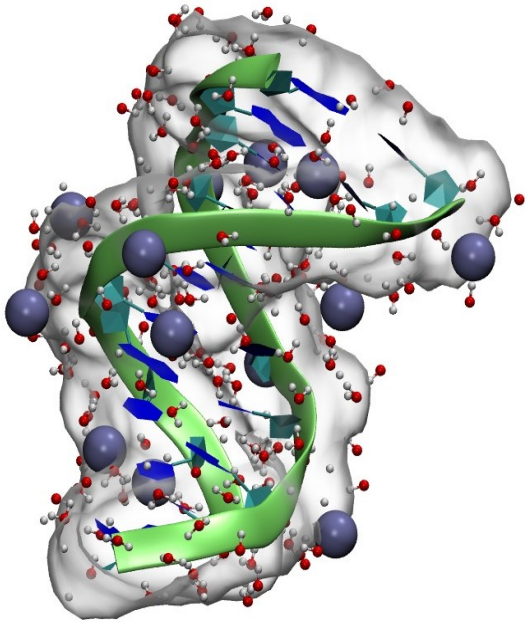

Figure 3-4 Double stranded DNA, 10-mer from an MD simulation snapshot. The DNA backbone is shown in cartoon representation. Water molecules within 3 Å distances from DNA are in the ball and stick representation; sodium ions in proximity of DNA are shown as van der Waals spheres (in blue). Solvent accessible surface of DNA is shown in grey.

After energy minimization of water and ions, the entire system was energy minimized without restraints. The solvated system was further energy minimized using another 2500 steps of minimization (Figure 3-4).

3.3.1.3 Equilibration

The minimized solvated structure was then equilibrated in three steps. The DNA system was allowed to warm from 0 K to 298.15 °K at constant volume during a 20 ps first equilibration step. Restraints were applied to the ds-DNA, except for the hydrogen atoms, with a force constant of 200 kcal mol^{-1} $Å^{-2}$. The temperature was controlled using Langevin dynamics [142] with a collision frequency of 20 ps^{-1}. The particle-mesh Ewald (PME) method [143] was adopted for the numerical

computation of the electrostatic interaction. The nonbonded cutoff was kept at 10 Å. A time step of 2 fs was chosen for the MD simulation. The bond lengths that involved hydrogen atoms were constrained using the SHAKE algorithm [144].

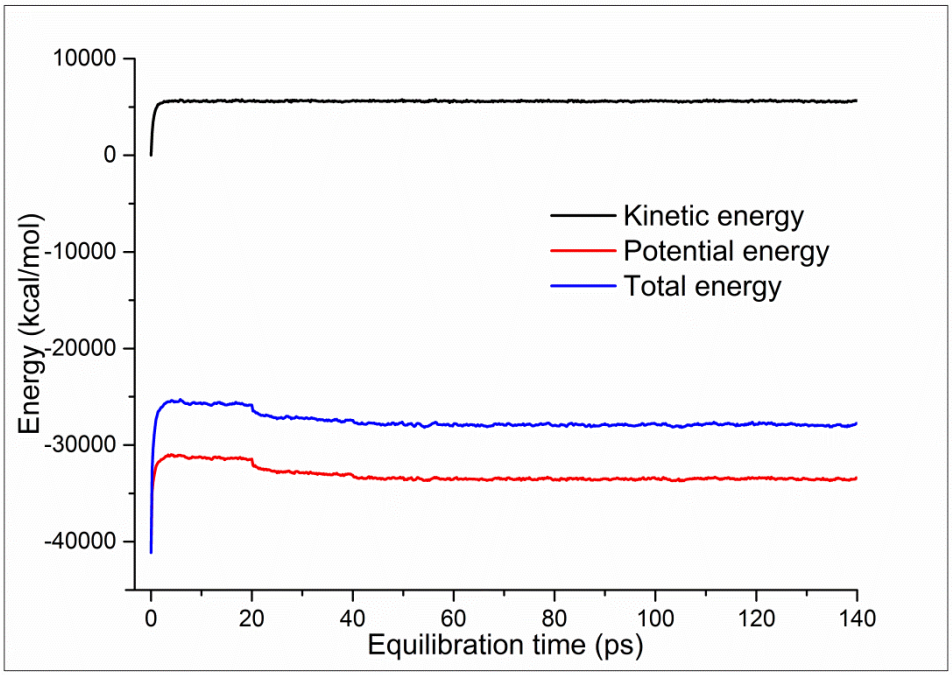

Figure 3-5 Energy of the system including kinetic (black), potential (blue), and total energy (red) during equilibration steps of the MD simulation.

The next equilibration step (20 ps) was performed using an isobaric-isothermal (NPT) ensemble and the pressure was maintained at 1 atm with isotropic position scaling and a pressure relaxation time of 1 ps. The constant temperature constant pressure (NPT) equilibration was carried out with position restraints on the DNA atoms, except hydrogens, with a force constant of 10 kcal mol^{-1} $Å^{-2}$. Later, a 100 ps equilibration was performed using the same NPT ensemble without restraints.

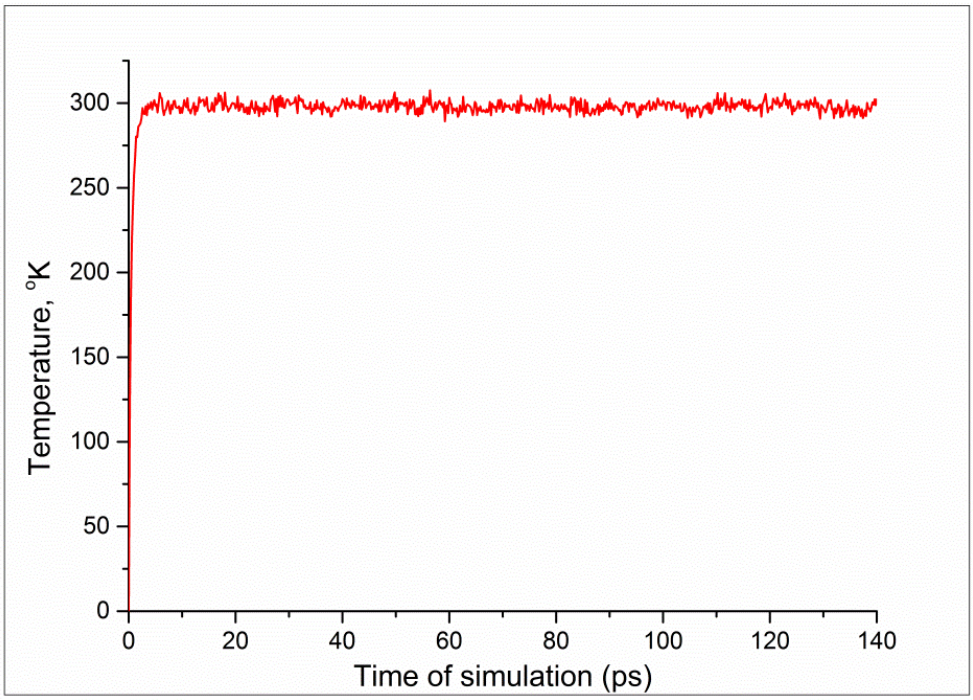

Figure 3-6 Temperature (K) of the system during equilibration step for 10-mer ds-DNA.

Figure 3-5 shows the how the energy of the system behaved during the equilibration MD simulation. The kinetic energy (green line) is positive, the potential energy (blue line) is negative, and the total energy (red line), a sum of potential and kinetic energy in the system during equilibration, is negative. Since I heated the system from 0 K to 300 K during the initial stage, the energies increased for first few picoseconds and the kinetic energy remained constant afterward, indicating that our thermostat was working properly. The potential energy initially increased then plateaued during the constant volume stage (0 to 20 ps) and subsequently decreased as our system relaxed during the constant pressure stage (20 to 40 ps). The potential energy and the total energy of the system remained constant for the remainder of the simulation (40 to 120 ps), indicating that relaxation was complete, and that the system had reached an equilibrium stage.

The system temperature increased from 0 °K and reached 298.15 °K in around 5 ps and remained constant thereafter during equilibration, indicating that the temperature control using Langevin thermostat was working (Figure 3-6).

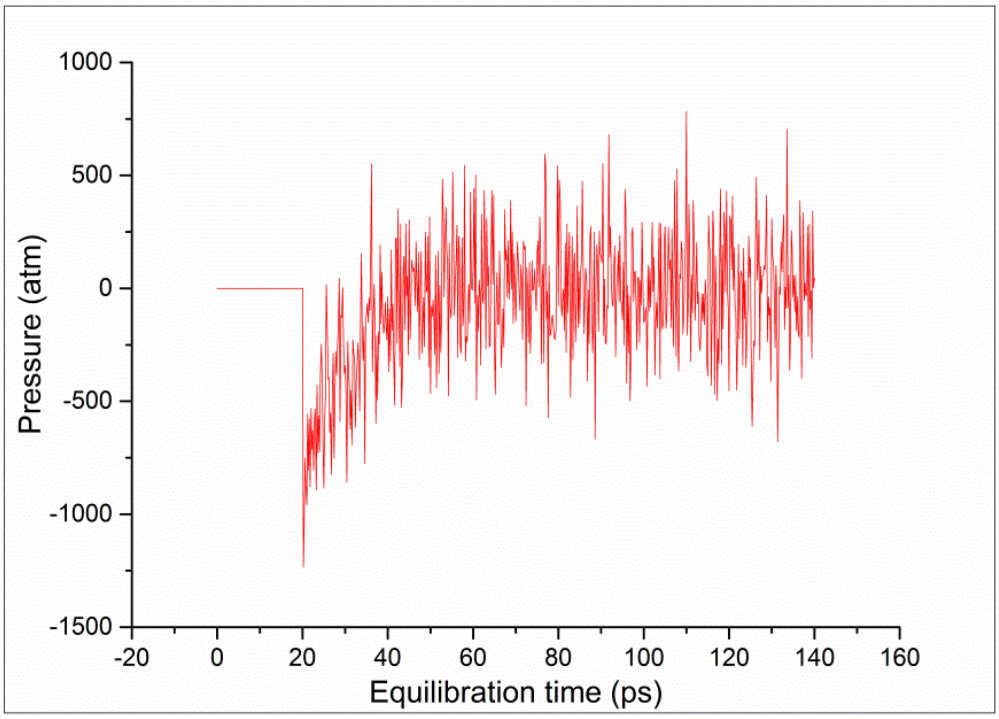

Figure 3-7 System pressure (in atm) during equilibration.

During the first 20 ps of simulation, the pressure of the system was showing zero since the system was running at constant volume during which the pressure was not evaluated (Figure 3-7). Even though there were wild fluctuations (20 ps to 140 ps) during the constant pressure simulation, after 50 ps a mean value of 1 atm was achieved during the equilibration.

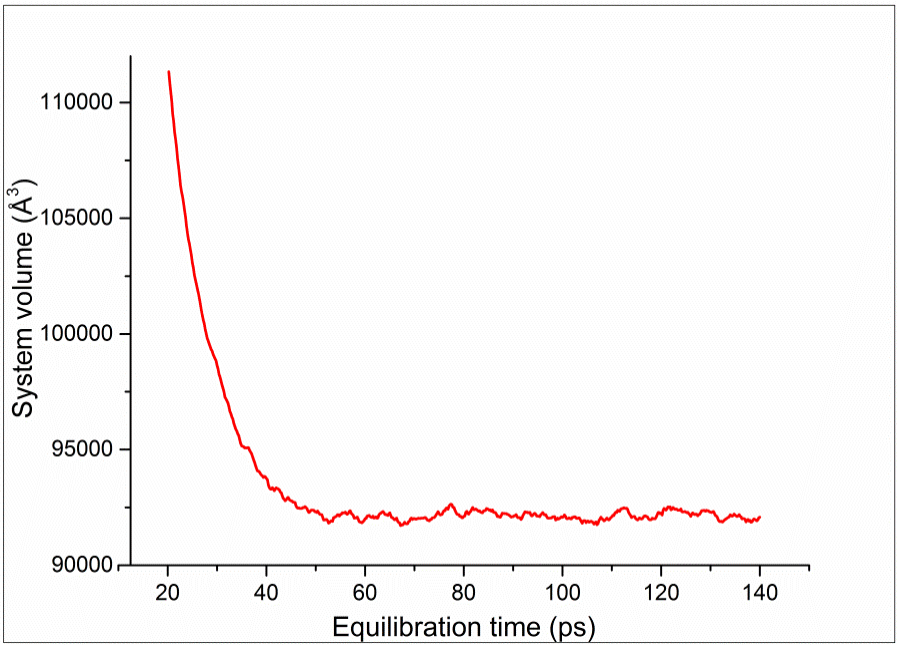

Figure 3-8 Volume of the system during equilibration.

As the octahedral water box relaxed, initially, the volume of the system decreased and thereafter oscillated around a mean value, indicating successful equilibration (Figure 3-8).

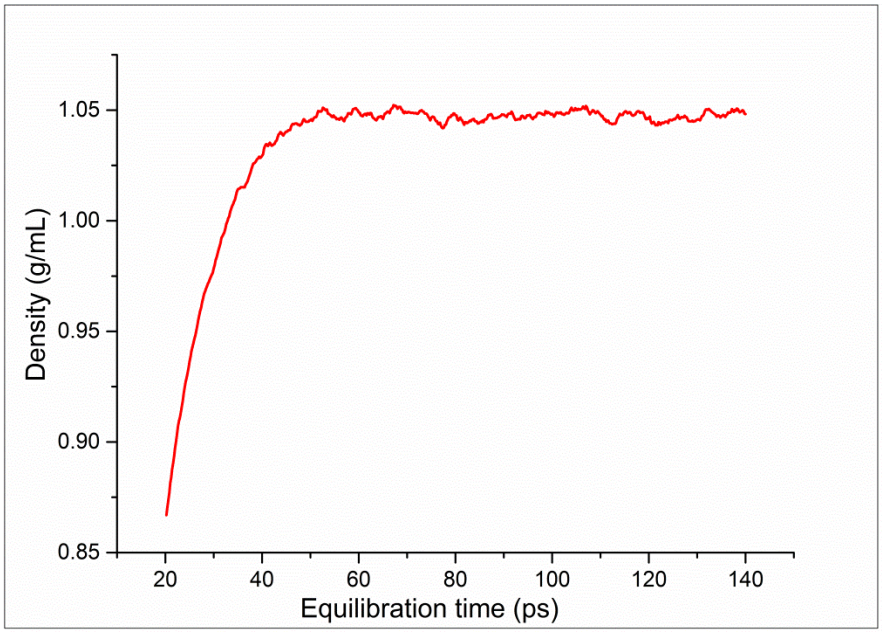

Figure 3-9 Density (in g/mL) of the system during equilibration.

As expected, the system appeared to equilibrate at a density of approximately 1.05 gcm^{-3}, which seemed reasonable since the density of pure liquid water at 298.15 K is approximately 1.00 gcm^{-3} (Figure 3-9). The addition of 10-mer ds-DNA to the water increased the density slightly (~ 5%).

To validate that the DNA structure was stable during the MD simulation, I calculated the root mean square deviation of the backbone atoms (P, O3*, O5* C3*, C4*, and C5*) as the DNA molecule oscillates. The root mean square deviation of the DNA backbone from the starting structure to the relaxation of the DNA structure in explicit solvent appears to be fairly stable with no wild oscillations (Figure 3-10).

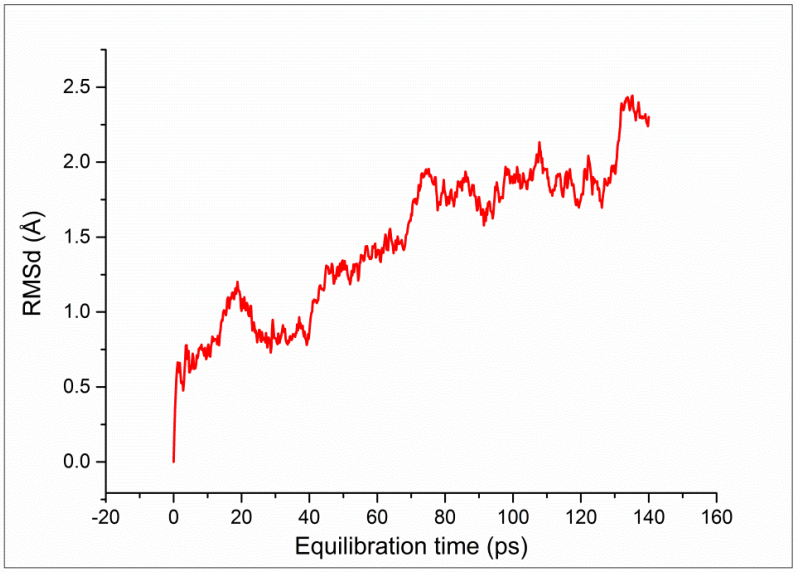

Figure 3-10 Root mean square deviation (RMSD) of the DNA backbone during equilibration of the system.

3.3.1.4 Production simulation run

The initial input structure was created, neutralized and solvated, and then brought to equilibrium to create the final structure and the files needed to perform

an MD simulation of the DNA structure in explicit solvent. After equilibration, a 1 ns production simulation was performed at constant temperature and pressure with a time step of 2 fs which is well accepted in biomolecular simulations. Such a time step was used in the previous MD simulation of DNA [145]. Table 3-3 shows the time taken for each simulation step for the 10-mer oligonucleotide. Figure 3-11 shows the snapshots of the double stranded DNA for various time steps during the MD simulation. The conformational state of the DNA is vital, since proper thermodynamic conditions and the conformational state of the DNA regulate the rate of hybridization. The selectivity and specificity of the hybridization also depends on the conformational state.

Table 3-3 Time taken through various steps of the MD simulation of the complex and single stranded DNA strands of 10-mer

MD simulation step	Simulation time	Actual computational time		
		Complex	SS1	SS2
Energy Minimization	1000 steps	3 min	3 min	3 min
Equilibration Heating	20 ps	26 min	29 min	33 min
Density	20 ps	18 min	20 min	25 min
Equilibration	100 ps	1 hr 34 min	1 hr 38 min	1 hr 58 min
Production	1 ns	15 hr 9 min	16 hr 1 min	15 hr 38 min

In many free energy simulation studies, the equilibration time has been determined by using certain qualitative criteria like monitoring the potential energy and structure of the system [146]. The equilibration time could be determined as the first plateau in the potential energy following the heating of the system to 300 ^{o}K. From Figure 3-12 for 10-mer it is clear that the system reached equilibrium state in approximately 50 ps of the MD simulation. So, 140 ps

simulation time should be more than enough time to conclude that the system reached equilibrium. The trajectories generated from 140 ps to 1140 ps were used for post-processing calculations which seem free of any systematic error since potential energy plateaus at an average value of ~33,800 kcal/mol. The potential energy curves for longer production runs were used to verify there is no systematic error for all 4 ds-DNA samples and are provided in Appendix III.

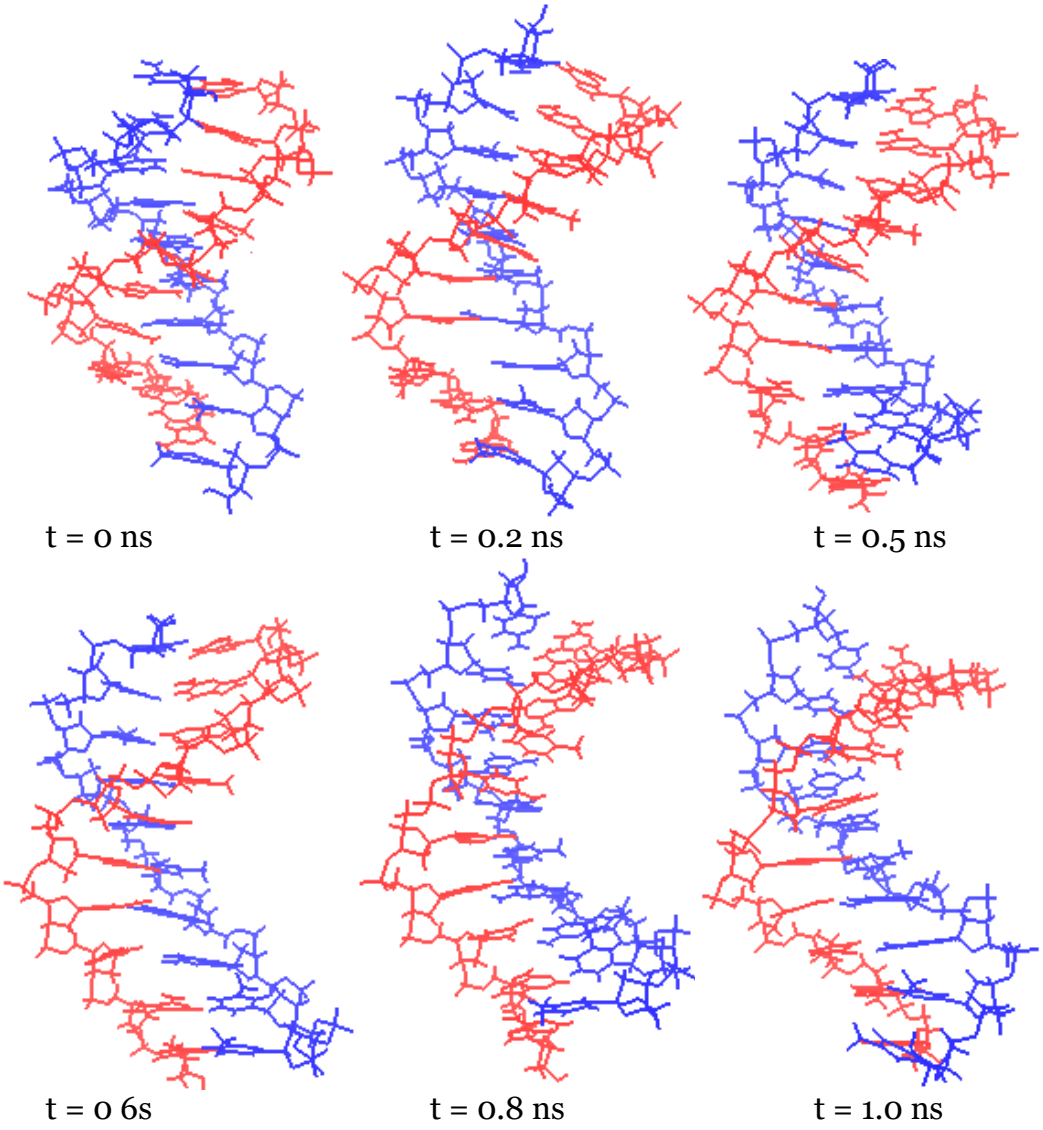

Figure 3-11 MD trajectories at various time (t) intervals during the 1 ns MD simulation of the 10-mer ds-DNA system.

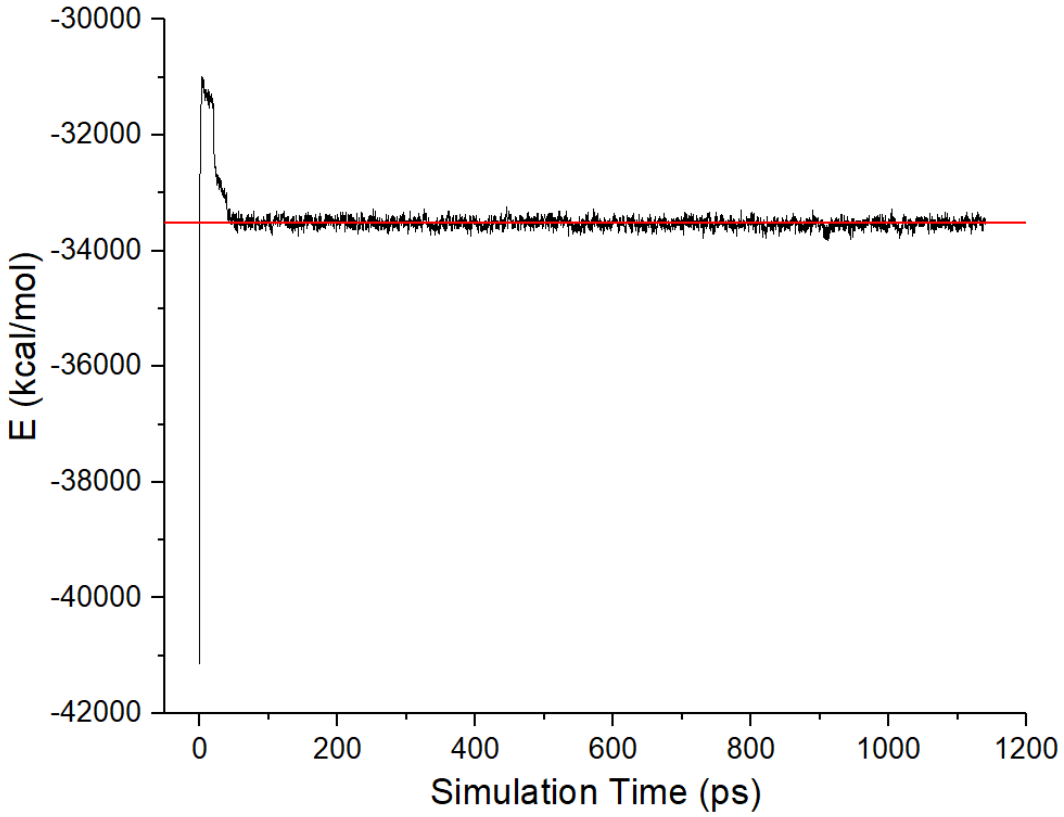

Figure 3-12 Potential energy plots after the MD simulation of 10-mer. The red line indicates the plateau region where 10-mer structure begins to look stable and equilibrated from ~50 ps onwards of simulation time.

The root mean square deviation (RMSDs) relative to an equilibrated structure was used to monitor the conformational changes of the backbone of oligonucleotides during MD simulations (Figure 3-13). The MD simulation of the smaller oligonucleotides of 9-mer, 10-mer and pal10-mer show RMSDs which are fairly stable with no wild oscillations and average RMSDs of 2.9, 2.6 and 3.0 Å, respectively. The larger 20-mer shows greater fluctuations with an average RMSD of ~5.5 Å. The RMSDs are calculated using trajectories obtained at every 200 fs of the production MD run.

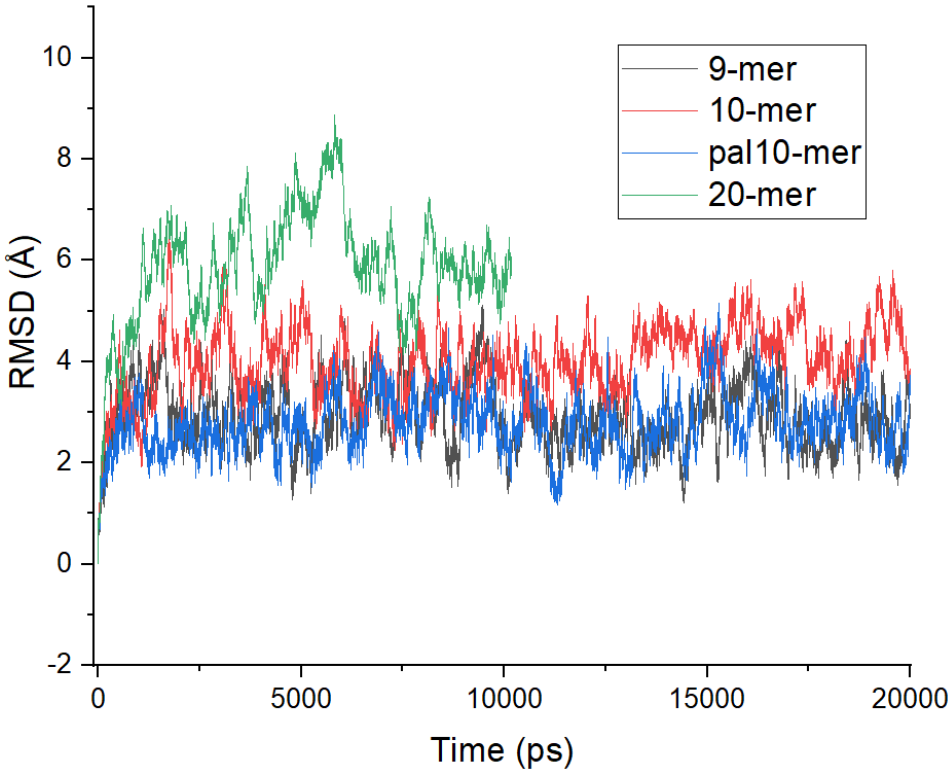

Figure 3-13 Root mean square deviations of the backbone atoms of the oligonucleotides 9-mer, 10-mer, and pal10-mer for 20 ns and 20-mer for 10 ns of MD simulation run from the initial structure including the equilibration and production run.

3.3.2 Error analysis for MD simulation trajectories

An accurate ensemble average of structural trajectories generated using MD simulation is essential for meaningful post-processing for the free energy calculation. The molecular mechanics (MM) approach aims at obtaining statistically converged values for all thermodynamic properties of interest. An efficient sampling procedure is needed to reduce the considerable number of calculations and to obtain proper statistically converged average values. This can be achieved either using statistical correlation or the statistical inefficiency method [135, 147, 148]. Here, statistical correlation method is used by analyzing the correlation of a thermodynamic property between successive configurations of the system generated by MD simulation. To perform the statistical correlation

calculation, potential energy of the system is chosen as the thermodynamic property, f. The computed average of f is obtained by:

$$\langle f \rangle_L = \frac{1}{L}\sum_{i=1}^{L} f_{i,} \tag{3.26}$$

where L is the number of MD trajectories. The statistical error $err(\langle f \rangle_L)$ due to the finite size of the successive values of $\{f_i\}$ generated from MD simulation is obtained as:

$$err(\langle f \rangle_L) = \sqrt{\frac{\langle \delta f^2 \rangle}{L/s}}, \tag{3.27}$$

where s is the interval needed to obtain statistically uncorrelated configurations. The statistical correlation between the configurations can be calculated through correlation coefficient $C(k)$ given by:

$$C(k) \cong \frac{\langle f_i f_{i+k} \rangle_{L-k} - \langle f_i \rangle_{L-k} \langle f_{i+k} \rangle_{L-k}}{\langle f^2 \rangle_L - \langle f \rangle_L^2} \tag{3.28}$$

where k is the interval. The correlation time, τ can be obtained by:

$$\tau = \int_0^\infty C(k) dk. \tag{3.29}$$

Figure 3-14 shows the exponential decay of the correlation coefficient with increased correlation time, τ. Using curve fitting analysis, a value of ~0.75 ps is calculated as the correlation time. In general, to obtain statistically uncorrelated data, the rule of thumb is to use trajectories spaced larger than 2τ units apart in simulation time [147], which will be ~1.5 ps in the case of 10-mer. In addition, we could see a plateau of the correlation curve, from around 2 to 6 ps values of τ close to a correlation coefficient of ~10% or less. Thus, for this DNA system, 250 MD

trajectories sampled with a 4 ps interval from a 1 ns MD simulation should be more than enough to obtain statistically converged average values for our binding free energy calculations in the post-processing step with a standard error of ± 0.2 %. The correlation coefficient distribution with correlation time for all 4 ds-DNA samples are provided in Appendix III.

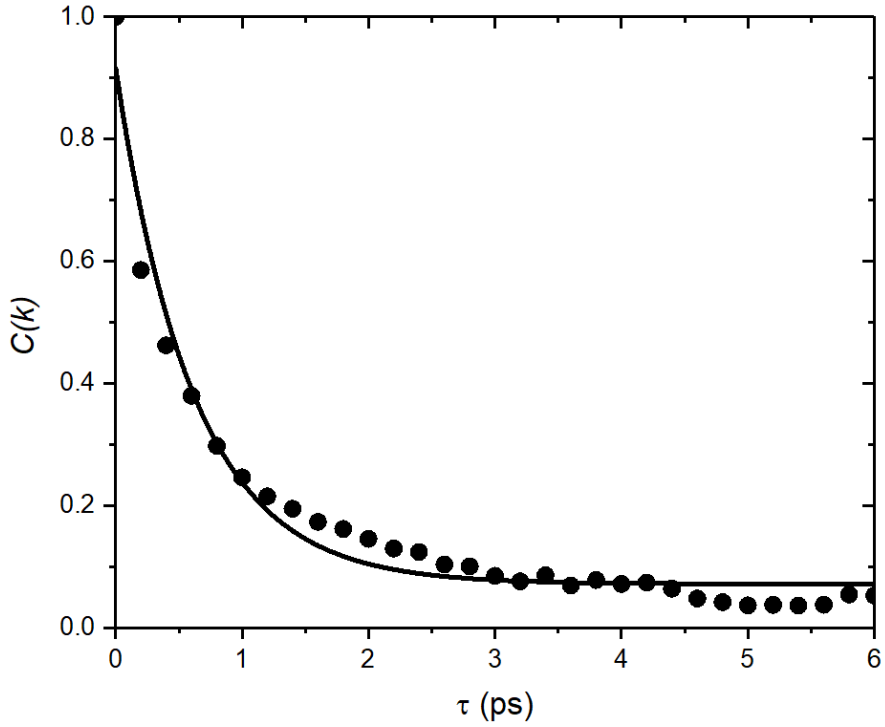

Figure 3-14 Distribution of the correlation coefficient with correlation time intervals chosen to estimate the statistically converge interval for 10mer configurations obtained from MD simulation.

3.3.3 Post-processing MD trajectories

The method and procedure used to calculate the solvation energy of the binding for the created trajectories is depicted in Figure 3-15. The 3D-RISM-KH method was used to calculate the solvation energy and the results were compared with MM/PB(GB)SA results and with the experimental value. In this way, I found the

best procedure for calculating the binding energy of two single stranded DNA to form the ds-DNA complex. The results obtained with these calculations are discussed in detail in section 3.4. Appendix II provides the details of the commands and input files used for the post-processing of the 10-mer oligonucleotide MD trajectories.

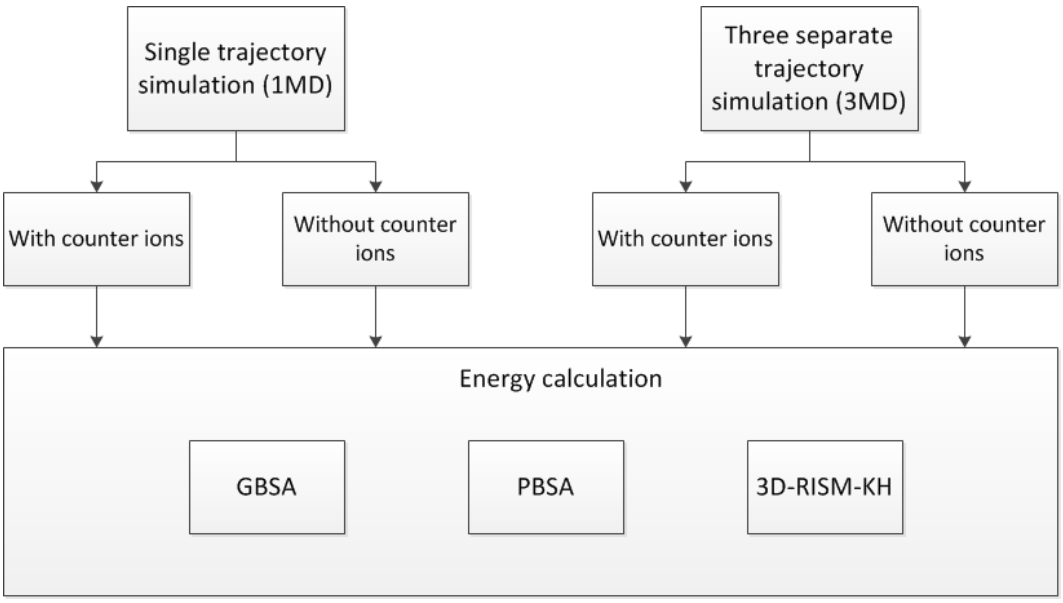

Figure 3-15 Flow chart showing the steps involved in performing the post-processing of the DNA molecule trajectories generated by MD simulation.

3.3.3.1 MM/(PB/GB)SA calculations

The molecular mechanics/Poisson-Boltzmann surface area (MM/PBSA) analysis implemented in the AMBER 11 package [90] computes the binding free energy by using a thermodynamic cycle that combines the molecular mechanical energies with the continuum solvent approaches, that is, the Poisson-Boltzmann/general Born surface area (PB/GBSA) [89, 91] . All water molecules were stripped off during the post processing of the MD trajectories. Energies were calculated with and without counter ions for the MD trajectories. Both PB and GB

methods calculate the polar part of the solvation energy. Generalized Born calculations were performed using the GB^{OBC} model [149] with a second modified Bondi radii set (mbondi2). For the Poisson-Boltzmann method a solvent probe radius of 1.4 Å was used. The solute and solvent dielectric constants were set as 1 and 80, respectively for both PB and GB methods. A linear combination of pairwise overlaps (LCPO) method was used for solvent accessible surface area (SASA) calculations [150] to estimate the nonelectrostatic solvation interactions using equation 3.11 with $\sigma = 0.0072$ kcal mol^{-1} $Å^2$and $\varphi = 0$ kcal/mol. The conformational entropy part ($T\Delta S$) of the oligos was calculated using the NMODE module in the AMBER 10 molecular dynamics package which performs computations based on normal mode analysis. The convergence criterion for the energy gradient was set to a value of 10^{-5} kcal/mol.Å.

3.3.3.2 3D-RISM-KH calculations

To derive the solvation free energy, 3D-RISM-KH equations 3.17 and 3.22 were solved on a uniform 3D grid of 256×256×256 points in a cuboid supercell of size 128x128x128 Å, large enough to accommodate the DNA together with sufficient solvation space around. To solvate the oligonucleotide variable size, the solvation box in the AMBER package was used with the option of maintaining a minimum distance of 14 Å between the solute and the edge of the solvent box. The equations converged to a relative root mean square accuracy of 10^{-4} by using the modified direct inversion in the iterative subspace (MDIIS), an accelerated numerical solver of integral equations of liquid state theory [38]. The solute-solvent interaction potential comprises the Coulomb and Lennard-Jones interactions. The DNA

atoms were described from the OPLS-AA force field [151], and used the TIP3P model [152] of water solvent molecules to describe the thermodynamic and structural properties of bulk water. The bulk water solvent has density of 0.99705 g/cm^3 and a dielectric constant of 78.4 which corresponds to ambient conditions of temperature (298 °K) and pressure (1 atm). Calculations were also performed using solute with no partial charges to find the nonpolar G_{np} and polar G_{pol} energy contribution to the solvation free energy.

3.3.4 Computational requirements

In this thesis study, a total of 33 MD simulations were ran in explicit solvent. For 10-mer DNA alone, 8 MD simulations were conducted to get trajectories to evaluate the "Run 1 MD" and "Run 3 MD" methods. The MD simulations for both methods were performed with and without ions, as well. The *bugaboo* server in the WestGrid facility was utilized to perform this MD simulations using AMBER 10. The server administrator allowed users to submit simulation jobs, using 1 processor for each job and up to 1600 MB of memory. The average time of performing each MD simulation is ~36 hrs including minimization, equilibration and production step involved. The least time required was for 9-mer (~20 hrs) and more time was needed for the bigger system of 20-mer (~90 hrs of calculation). Considering these numbers, around ~1220 hours of calculation time is required to perform all 33 MD simulations without considering the time for development, debugging and testing of the scripts. The availability of AMBER software in WestGrid facilitated running many of the MD simulation job in parallel.

Calculating a 3D-RISM-KH solution for a single solute conformation during post-processing typically required about 100 times more computer time than the same calculation with GB/PBSA. The average computational time for a single snapshot of the DNA duplex in the water solvent was about ~16 min run on 4 CPU cores of the 2.5 GHz Intel Xeon processor with 16 cores. In addition, the file size of the output from 3D-RISM calculations which are useful for visualization and further analysis is in the range of ~275 MB for each solvent per frame, so it can quickly fill disk space.

3.4 Results and discussion

3.4.1 Calculation of the DNA binding free energy with 3D-RISM-KH

The MMPB/GBSA method averages contributions of gas-phase energies, solvation free energies, and solute entropies calculated for snapshots of the DNA complex molecule as well as the unbound components, which are extracted from MD trajectories. The binding free energy is obtained as the difference between the free energy of the complex and the free energy of the individual molecules. Since 3D-RISM-KH calculations are computationally demanding, post-processing of the MD trajectories was performed for an optimum number of snapshots. To obtain the optimum number of snapshots, the negative binding free energy ($-\Delta G_{bind}$) values obtained using the MM/GBSA method is plotted against the number of snapshots processed in Figure 3-16. Around 250 snapshots were sufficient to find the ensemble average for calculating the binding free energy for the 9-mer, 10-mer, pal10-mer and 20-mer oligonucleotides. The standard errors for the mean

binding energy values calculated using the GBSA method are given in Table 3-4. The standard error of the binding energy based on 250 energy calculations is ~0.5 kcal/mol for 10-mer. Post-processing of the energies obtained using the three separate trajectories approach is discussed in section 3.4.2.

Table 3-4 Standard Error of the mean binding energy of all four DNAs for various number of snapshots[a]

Number of snapshots	9-mer	10-mer	pal10-mer	20-mer
5	5.1	5.8	5.5	5.1
10	3.1	3.5	3.3	2.8
20	2.1	2.3	2.3	1.7
25	1.6	1.8	1.8	1.5
50	1.1	1.2	1.2	1.0
70	0.9	1.0	1.0	0.8
90	0.8	0.8	0.8	0.6
100	0.8	0.8	0.8	0.6
120	0.7	0.7	0.7	0.6
150	0.6	0.7	0.7	0.5
200	0.5	0.6	0.6	0.4
250	0.4	0.5	0.5	0.4
500	0.3	0.4	0.4	0.3
1000	0.2	0.3	0.3	0.2
1250	0.2	0.2	0.2	0.2
2500	0.1	0.2	0.2	0.1
5000	0.1	0.1	0.1	0.1

[a] All energies are in kcal/mol

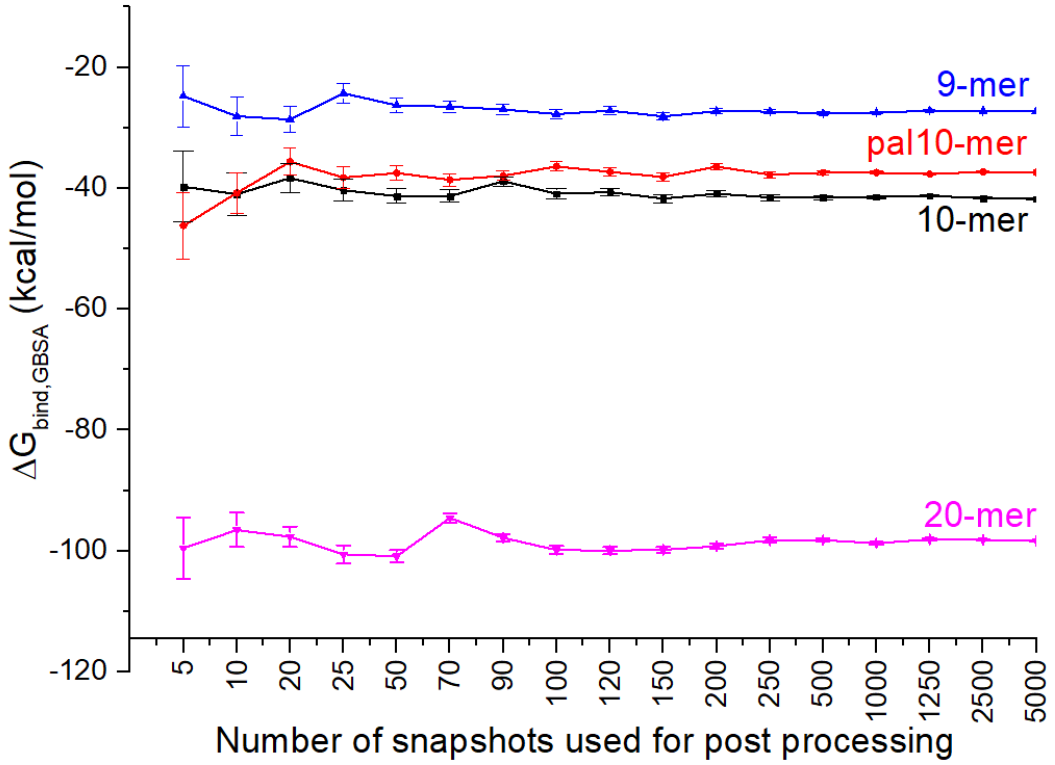

Figure 3-16 Binding free energy values for DNA 10-mer, 20-mer, 9-mer, and pal10-mer strands using the MM/GBSA approach versus the number of snapshots processed. All values were obtained using "Run 1 MD" simulations and fixing Na+ ions during post-processing. The standard errors are given by the vertical bars.

3.4.2 Oligonucleotide binding energies obtained using Run 3 MD

The binding energy values obtained after post-processing of all four oligonucleotide samples in the three-trajectory approach (Run 3 MD) with and without stripping Na+ ions are summarized in Tables 3.4 and 3.5, respectively. The energetic and entropic contributions to the binding free energy of the ds-DNA sample were obtained from 250 snapshots extracted from 1 nanosecond of MD simulation (Run 1 MD).

Table 3-5 Oligonucleotide binding energies (kcal/mol) obtained in three molecular dynamics (Run 3 MD) approaches to obtain solvation trajectories in which counter ions were stripped off for post-processing. The values are averaged from 250 snapshots.

Energy (kcal/mol)	Samples			
	9-mer	10-mer	pal10-mer	20-mer
E_{ele}	1062.5	1326.8	1319.4	4851.4
E_{vdW}	-29.6	-33.0	-36.8	-88.0
E_{int}	7.5	10.4	9.2	-1.8
$\langle \Delta \mathbf{E_{MM}} \rangle$	1040.3	1304.2	1291.8	4761.6
$\langle \mathbf{T\Delta S_{MM}} \rangle$	-24.0	-24.8	-24.9	-25.9
GBSA				
$\langle \Delta G_{sol,GBSA} \rangle$	-1072.2	-1342.2	-1339.1	-4852.7
$G_{pol,GBSA}$	-1066.7	-1335.8	-1332.6	-4839.3
$G_{np,SASA}$	-5.4	-6.4	-6.5	-13.4
$\langle \Delta H_{GBSA} \rangle$	-31.8	-38.0	-47.3	-91.1
$\Delta \mathbf{G_{bind,GBSA}}$	-7.7	-13.2	-22.4	-65.1
PBSA				
$\langle \Delta G_{sol,PBSA} \rangle$	-1085.2	-347.6	-1350.8	-4876.6
$G_{pol,PBSA}$	-1079.7	-1341.2	-1344.2	-4863.2
$G_{np,SASA}$	-5.4	-6.4	-6.5	-13.4
ΔH_{PBSA}	-44.8	-43.4	-58.9	-115.0
$\Delta \mathbf{G_{bind,PBSA}}$	-20.8	-18.6	-34.0	-89.0
3D-RISM-KH				
$\langle \Delta G_{sol,3DRISMKH} \rangle$	-1068.6	-1339.5	-1340.7	-4842.
$G_{pol,3DRISMKH}$	-1076.2	-1348.8	-1344.6	-4859.88
$G_{np,3DRISMKH}$	7.5	9.2	3.8	17.4
$\langle \Delta H_{3DRISMKH} \rangle$	-28.2	-35.3	-48.9	-80.7
$\Delta \mathbf{G_{bind,3DRISMKH}}$	-4.1	-10.5	-24.0	-54.7

The average internal energy term $\langle \Delta E_{MM} \rangle$, obtained using molecular mechanics and the average entropic contribution term $\langle T\Delta S_{MM} \rangle$ calculated by normal mode analysis was common for all the three methods. The gas phase energies include the Coulomb (E_{ele}), van der Waals (E_{vdW}), and internal (E_{int}) energies. The Columbic interaction and internal energy values disfavour the binding of the DNA strands. A positive internal energy indicates that conformational changes upon binding of the DNA strands led to internal strain which was true for all oligonucleotides

except the 20-mer (-1.80 kcal/mol). The van der Waals interactions, which contribute to the gas phase energy, were found to favour hybridization of the DNA strands, including the 10-mer which had a negative energy value of about -33 kcal/mol.

Electrostatic forces are much larger than van der Waals forces and entropic forces and thus make significant contributions to the binding energy of particles in the gas phase. The entropic term is a sum of translational, rotational, and vibrational components determined by normal mode analysis. Normal mode analysis approximates the potential energy surface of a molecular system by a harmonic function at some point on the surface. Changes in the degrees of freedom $\langle T\Delta S_{MM}\rangle$, as determined by normal mode analysis, amounted to -24.3 kcal/mol.

To a great extent the electrostatic component of the solvation energy is canceled by the polar component. The solvation free energy $\langle \Delta G_{sol}\rangle$ was obtained as a sum of the solvent accessible surface dependent nonpolar contribution (G_{np}) and a polar contribution (G_{pol}) using GBSA, PBSA, and 3D-RISM-KH methods. In this case, polar contributions to the solvation energy strongly favored complex formation in all three methods, with values of about -1335, -1341, and -1349 kcal/mol for GBSA, PBSA, and 3D-RISM-KH, respectively. On the other hand, there was a significant difference between results obtained with the SASA method and results obtained with the 3D-RISM-KH method. The SASA method predicted complex formation with a negative value whereas 3D-RISM-KH always predicted solvation with a positive value almost two times larger for each of the four oligonucleotides. The difference between SASA and 3D-RISM-KH results might be

due to the failure of SASA to predict the nonpolar contribution to the binding energy correctly [91, 109, 153, 154].

All three methods favoured the binding of the DNA strands, and for the 10-mer and the 20-mer the 3D-RISM-KH values were closest to the experimental value. The calculation of the nonpolar component of the solvation energy seems to be the factor that affects GBSA and PBSA binding energy calculations. For example, the pal10-mer and the 20-mer had GBSA binding energies of -22.43 and -65.15 kcal/mol, respectively. If the nonpolar part of the solvation energy calculated using SASA ($G_{np,SASA}$) is replaced with that of the 3D-RISM-KH ($G_{np,3DRISMKH}$), the binding energy values obtained are in good agreement with the experimental values as shown below.

Using $\langle \Delta G_{pol,GBSA} \rangle$ and $\langle \Delta G_{np,SASA} \rangle$ in equation 3.10 for calculation of the binding energy for pal10-mer, a value of -22.42 kcal/mol is obtained. Replacing $\langle \Delta G_{np,SASA} \rangle$ with $\langle \Delta G_{np,3DRISMKH} \rangle$ in equation 3.10 yields binding energy $\Delta G_{bind,pal10-mer}$ of -12.00 kcal/mol which is in better agreement with an experimental value of -15.5 kcal/mol [141]. Similarly, by replacing $\langle \Delta G_{np,SASA} \rangle$ with $\langle \Delta G_{np,3DRISMKH} \rangle$ in equation 3.10 for 20-mer yields binding energy $\Delta G_{bind,20mer}$ of -34.23 kcal/mol instead of -65.15 kcal/mol, again showing better agreement with experimental value of -40.0 kcal/mol [141].

These results show that the 3D-RISM-KH method predicts the nonpolar part of the solvation free energy more accurately than the SASA method when the neutralizing ions (Na+) are stripped from the three separate MD trajectories. The

results obtained from post-processing calculations with retained neutralizing ions are presented in Table 3-6.

Table 3-6 Oligonucleotide binding energies (kcal/mol) obtained in three molecular dynamics (Run 3 MD) approaches to obtain solvation trajectories in which counter ions were not stripped off for post-processing. The values are averaged from 250 snapshots.

Energy (kcal/mol)	Samples			
	9-mer	10-mer	pal10-mer	20-mer
E_{ele}	-161.0	-274.6	-388.8	-571.7
E_{vdW}	-29.5	-52.2	-32.1	-85.2
E_{int}	7.5	8.8	9.2	-1.8
$\langle \Delta \mathbf{E_{MM}} \rangle$	-183.0	-317.9	-411.7	-658.8
$\langle \mathbf{T}\Delta \mathbf{S_{MM}} \rangle$	-27.7	-25.1	-33.2	-42.2
GBSA				
$\langle \Delta G_{sol,GBSA} \rangle$	143.1	239.2	360.8	532.7
$G_{pol,GBSA}$	149.2	247.9	368.9	548.6
$G_{np,SASA}$	-6.0	-8.7	-8.1	-15.9
$\langle \Delta H_{GBSA} \rangle$	-39.9	-26.7	-50.8	-126.0
$\Delta \mathbf{G_{bind,GBSA}}$	-12.1	-53.5	-17.6	-83.8
PBSA				
$\langle \Delta G_{sol,PBSA} \rangle$	131.5	255.2	356.9	516.1
$G_{pol,PBSA}$	137.6	263.9	365.1	532.0
$G_{np,SASA}$	-6.0	-8.7	-8.1	-15.9
ΔH_{PBSA}	-51.4	-10.7	-54.7	-142.6
$\Delta \mathbf{G_{bind,PBSA}}$	-23.7	-37.5	-21.5	-100.4
3D-RISM-KH				
$\langle \Delta G_{sol,3DRISMKH} \rangle$	157.8	240.4	378.3	533.5
$G_{pol,3DRISMKH}$	148.6	228.8	375.6	506.1
$G_{np,3DRISMKH}$	9.2	11.7	2.7	27.3
$\langle \Delta H_{3DRISMKH} \rangle$	-25.1	-45.8	-33.3	-125.2
$\Delta \mathbf{G_{bind,3DRISMKH}}$	2.3	-52.4	-0.1	-83.0

When neutralizing Na+ ions were retained during post-processing, the negative Coulombic interactions favoured the binding of the DNA strands except for the 10-mer, which showed positive Coulombic interactions which disfavoured binding and negative polar solvation energy which favoured binding. The positive values of the internal energy of most of the systems disfavoured the association of the

DNA strands. For 9-mer and pal10-mer GBSA, binding energy values of -12.16 and -17.66 kcal/mol were closer to experimental values of -8.5 and -15.5 kcal/mol, respectively. The 3D-RISM-KH method calculated a nonfavourable binding energy value for the 9-mer and weaker binding for the pal10-mer. On the other hand, it showed strong association energy for the 10-mer and a value closer to the experimental value than the GBSA and PBSA methods. The presence of the neutralizing ions made the binding energy stronger in most cases.

3.4.3 Oligonucleotide binding energies obtained using Run 1 MD

The single molecular dynamics (Run 1 MD) approach is less costly than a triple molecular dynamics (Run 3 MD) approach. The energy values obtained after post-processing of all four oligonucleotide samples in a single trajectory approach (Run 1 MD) with and without stripping of Na^+ ions are summarized in Tables 3.7 and 3.9 respectively. Similar to the "Run 3 MD" approach, the energetic and entropic contributions to the binding free energy of the ds-DNA were obtained from 250 snapshots extracted from 1 nanosecond of a single MD simulation (Run 1 MD). The internal energy (E_{int}) of the system is zero because all of the intermolecular energies cancel which differ from the Run 3 MD approach. In the "Run 1 MD" approach, none of the post-processing methods provided a result close to the experimental value, but all the results favoured the binding of the DNA strands. Interestingly, as with the "Run 3 MD" simulation, substitution of 3D-RISM-KH values obtained for the nonpolar part of the solvation energy for values calculated

in the GBSA analysis, yielded binding energy values closer to the experimental results.

Table 3-7 Oligonucleotide binding energies (kcal/mol) obtained in a single molecular dynamics (Run 1 MD) approach to obtain solvation trajectories using GBSA, PBSA, and 3D-RISM-KH post-processing. Counter ions were stripped off for post-processing.

Energy (kcal/mol)	Samples			
	9-mer	10-mer	pal10-mer	20-mer
E_{ele}	1078.7	1402.9	1406.1	4995.9
E_{vdW}	-44.4	-49.4	-49.8	-102.0
E_{int}	0.0	0.0	0.0	0.0
$\langle \Delta \mathbf{E_{MM}} \rangle$	1034.2	1353.5	1356.2	4893.9
$\langle \mathbf{T\Delta S_{MM}} \rangle$	-23.0	-23.9	-23.7	-25.3
GBSA				
$\langle \Delta G_{sol,GBSA} \rangle$	-1081.3	-1411.2	-1421.2	-4993.6
$G_{pol,GBSA}$	-1074.9	-1404.1	-1414.0	-4979.6
$G_{np,SASA}$	-6.4	-7.1	-7.2	-14.0
$\langle \Delta H_{GBSA} \rangle$	-47.0	-57.7	-64.9	-99.7
$\Delta \mathbf{G_{bind,GBSA}}$	-24.0	-33.8	-41.2	-74.4
PBSA				
$\langle \Delta G_{sol,PBSA} \rangle$	-1098.2	-1419.9	-1438.4	-5026.5
$G_{pol,PBSA}$	-1091.7	-1412.8	-1431.1	-5012.5
$G_{np,SASA}$	-6.4	-7.1	-7.2	-14.0
ΔH_{PBSA}	-63.9	-66.4	-82.1	-132.6
$\Delta \mathbf{G_{bind,PBSA}}$	-40.9	-42.5	-58.3	-107.3
3D-RISM-KH				
$\langle \Delta G_{sol,3DRISMKH} \rangle$	-1078.6	-1403.7	-1416.0	-4978.3
$G_{pol,3DRISMKH}$	-1090.9	-1419.5	-1428.4	-5007.2
$G_{np,3DRISMKH}$	12.3	15.8	12.3	28.9
$\langle \Delta H_{3DRISMKH} \rangle$	-44.3	-50.2	-59.8	-84.4
$\Delta \mathbf{G_{bind,3DRISMKH}}$	-21.3	-26.3	-36.0	-59.1

Using $\langle \Delta G_{pol,GBSA} \rangle$ and $\langle \Delta G_{np,SASA} \rangle$ in equation 3.10 for calculation of the binding energy for 10-mer, a value of -33.82 kcal/mol is obtained. Replacing $\langle \Delta G_{np,SASA} \rangle$ with $\langle \Delta G_{np,3DRISMKH} \rangle$ in equation 3.10 yields a binding energy $\Delta G_{bind,pal10-mer}$ of -10.86 kcal/mol which is in better agreement with experimental value of -11.96 kcal/mol. A similar approach yielded binding energy ΔG_{bind} values of -5.29, -21.89,

and -31.46 kcal/mol instead of -24.06, -41.21, and -74.42 kcal/mol, showing better correlation with experimental binding energy values of -8.5, -15.5, and -40.0 kcal/mol for 9-mer, pal10-mer and 20-mer, respectively.

The substitution of nonpolar $\Delta G_{np,3DRISMKH}$ post-processing values for $\Delta G_{np,SASA}$ values indicates that 3D-RISM-KH is superior to SASA for estimating the nonpolar solvation energy of the oligonucleotides tested, and the values obtained are summarized in Table 3-8.

Table 3-8 Oligonucleotide binding energy obtained for the GBSA post-processing method by replacing the nonpolar energy part with 3D-RISM-KH values in the "Run 1 MD" approach. Neutralizing ions were stripped for post-processing.

Sample	$\Delta \mathbf{G_{bind}}_{,GBSA}$ (kcal/mol) using nonpolar solvation energy from SASA	$\Delta \mathbf{G_{bind}}$, using nonpolar solvation energy from 3D-RISM-KH	$\Delta \mathbf{G}_{Expt}$
9-mer	-24.0	-5.2	-8.5
10-mer	-33.8	-10.8	-11.9
pal10-mer	-41.2	-21.8	-15.5
20-mer	-74.4	-31.4	-40.0

Results obtained for "Run 1 MD" simulations without stripping neutralizing ions are shown in Table 3-8. Similar to the "Run 3 MD" approach, both Coulombic and van der Waals interactions favour hybridization of the DNA strands, including the 10-mer strand which shows negative energy values of about -173 and -46 kcal/mol, respectively. As expected, the internal energy (E_{int}) of the system is zero since all of the intermolecular energies cancel out when calculating the association energy. The electrostatic part of the binding energy is much larger than the van der Waals and entropic terms which contribute to the gas phase energy. The entropic term $\langle T\Delta S_{MM} \rangle$, i.e., changes in the degrees of freedom, as determined by normal mode analysis, is equal to -28.4 kcal/mol.

The polar part of the solvation energy disfavours complex formation for all three methods, with values of about 156, 138, and 118 kcal/mol for GBSA, PBSA, and 3D-RISM-KH, respectively. As expected, the SASA method predicted favorable conditions with negative values whereas 3D-RISM-KH predicted unfavorable conditions with positive values about three times larger than those calculated by SASA for all four oligonucleotides.

Table 3-9 Oligonucleotide binding energies (kcal/mol) obtained in a single molecular dynamics (Run 1 MD) approach to obtain solvation trajectories using GBSA, PBSA, and 3D-RISM-KH post-processing. Counter ions were not stripped for post-processing.

Energy (kcal/mol)	Samples			
	9-mer	10-mer	pal10-mer	20-mer
E_{ele}	-73.0	-172.8	-225.4	-523.2
E_{vdW}	-44.2	-45.8	-47.3	-98.1
E_{int}	0.0	0.0	0.0	0.0
$\langle \Delta \mathbf{E_{MM}} \rangle$	-117.2	-218.7	-272.7	-621.3
$\langle \mathbf{T}\Delta \mathbf{S_{MM}} \rangle$	-28.4	-28.2	-35.4	-39.9
GBSA				
$\langle \Delta G_{sol,GBSA} \rangle$	61.5	148.9	199.5	483.1
$G_{pol,GBSA}$	68.3	156.5	207.5	499.3
$G_{np,SASA}$	-6.7	-7.5	-8.0	-16.2
$\langle \Delta H_{GBSA} \rangle$	-55.7	-69.7	-73.1	-138.1
$\Delta \mathbf{G_{bind,GBSA}}$	-27.2	-41.5	-37.7	-98.2
PBSA				
$\langle \Delta G_{sol,PBSA} \rangle$	44.2	131.0	184.9	455.9
$G_{pol,PBSA}$	51.0	138.5	192.9	472.1
$G_{np,SASA}$	-6.7	-7.5	-8.0	-16.2
ΔH_{PBSA}	-72.7	-87.7	-87.7	-165.3
$\Delta \mathbf{G_{bind,PBSA}}$	-44.1	-59.4	-52.3	-125.4
3D-RISM-KH				
$\langle \Delta G_{sol,3DRISMKH} \rangle$	57.4	133.6	197.0	469.4
$G_{pol,3DRISMKH}$	43.7	118.1	183.7	433.3
$G_{np,3DRISMKH}$	13.7	15.5	13.2	36.0
$\langle \Delta H_{3DRISMKH} \rangle$	-59.7	133.6	-75.7	-151.8
$\Delta \mathbf{G_{bind,3DRISMKH}}$	-31.3	-56.8	-40.4	-111.9

For all four oligonucleotides, the "Run 1 MD" simulated binding energies were not convincingly close to experimental ($\Delta G_{bind,Expt}$) values. The GBSA method predicted values closer to experimental values than PBSA and 3D-RISM-KH methods. GBSA analysis of the 10-mer predicted a binding energy of -41.51 kcal/mol, which is four times higher than the experimental value of -11.96 kcal/mol. The positive factor is that the theoretical calculations estimated favorable energies for binding of the DNA strands. Again, if the nonpolar solvation energy obtained with the GBSA method is replaced with that obtained with the 3D-RISM-KH method, the resulting theoretical binding energy values agree well with experimental values (Table 3-10).

Table 3-10 Oligonucleotide binding energy obtained for the GBSA post-processing method by replacing the nonpolar energy part with 3D-RISM-KH values in the "Run 1 MD" approach. Neutralizing ions were retained for post-processing.

Sample	**$\Delta G_{bind,GBSA}$ (kcal/mol) using nonpolar solvation energy from SASA**	**ΔG_{bind} (kcal/mol) calculated using nonpolar solvation energy from 3D-RISM-KH**	**ΔG_{Expt}**
9-mer	-27.2	-6.7	-8.5
10-mer	-41.5	-18.4	-11.9
pal10-mer	-37.7	-16.4	-15.5
20-mer	-98.2	-45.9	-40.0

3.4.4 Validation of various approaches to find binding energy

Among these DNAs, the binding energy ($\Delta G_{bind,Expt}$) of 20-mer > pal10-mer > 10-mer > 9-mer (Table 3-10) and it agrees with the results obtained after post processing without counter ions for both "Run 1 MD" and "Run 3 MD" approach. In contrast, while keeping the counter ions for post processing we can observe binding energy of 20-mer> 10-mer > pal10-mer > 9-mer, which disagrees with the

experimental value. This suggests stripping the counter ions is necessary for the energy calculations of the trajectories from molecular mechanics.

In order to evaluate the approach suitable to calculate the binding energy of the DNA strands, a graphical comparison to the experimental was utilized for each method. The calculated binding energies values with and without neutralizing ions for the "Run 1 MD" and "Run 3 MD" approach using GBSA (Figure 3-17), PBSA (Figure 3-18) and 3D-RISM-KH (Figure 3-19) respectively are shown. From the graphical comparison, we can see that all methods show a fair correlation to the experimental data even though they show a constant offset from the experimental value. From the results obtained for "Run 1 MD", none of the methods provided a result closer to the experimental value, but all the results favored the binding of the DNA strands. For the calculated binding energy, the post processing of the trajectories obtained from Run 3 MD approach after stripping counter ions yielded results more close to the experimental values ($\Delta G_{bind,\,Expt}$) using GBSA, PBSA and 3D-RISM-KH method for calculating the solvation energy contribution for all DNAs used for the study. The results indicate that the following steps provide the best procedure to calculate the binding energy of the DNA strands:

1. Perform the MD simulation separately for the complex and the single strands in explicit solvent,

2. Strip off the neutralizing ions along with the water, and

3. Perform the solvation energy calculation using the 3D-RISM-KH method.

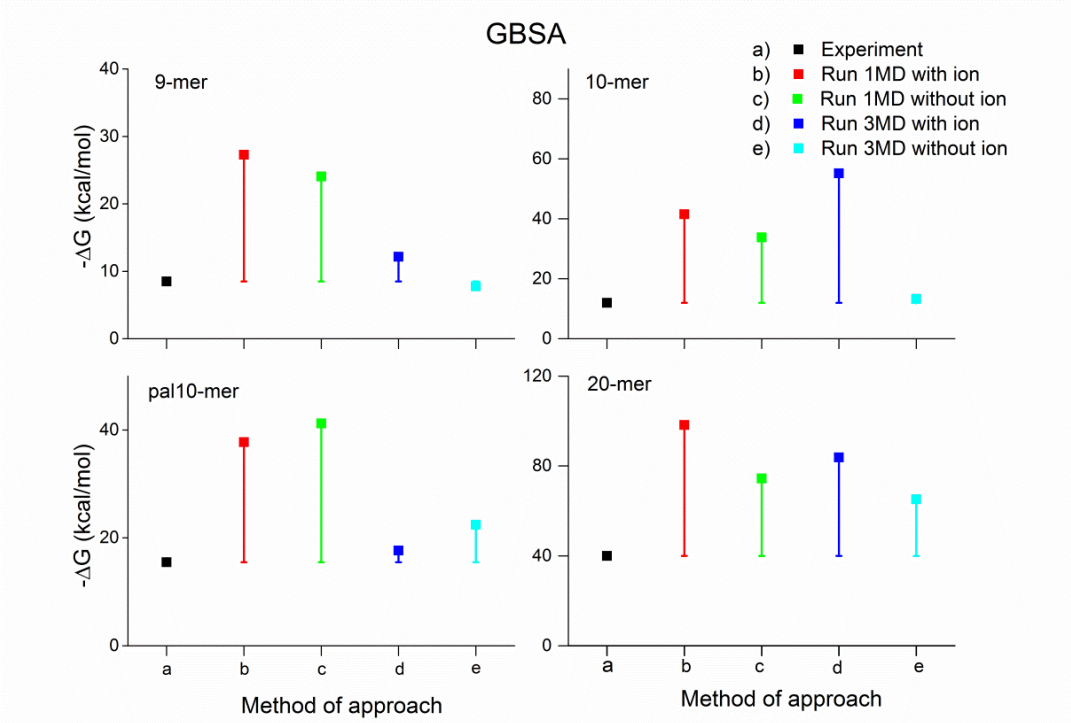

Figure 3-17 Oligonucleotide binding energies calculated using the GBSA method with "Run 1 MD" and "Run 3 MD" approaches with and without neutralizing ions, compared against experimental binding energies using minus error bars.

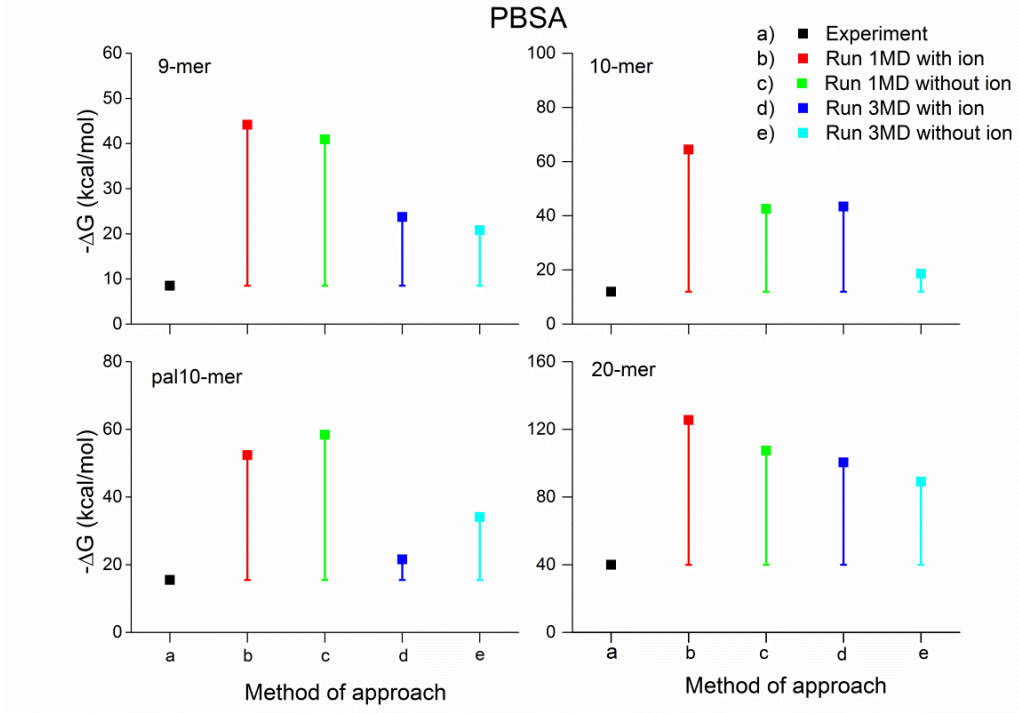

Figure 3-18 Oligonucleotide binding energies calculated using the PBSA method with "Run 1 MD" and "Run 3 MD" approaches with and without neutralizing ions, compared against experimental binding energies using minus error bars.

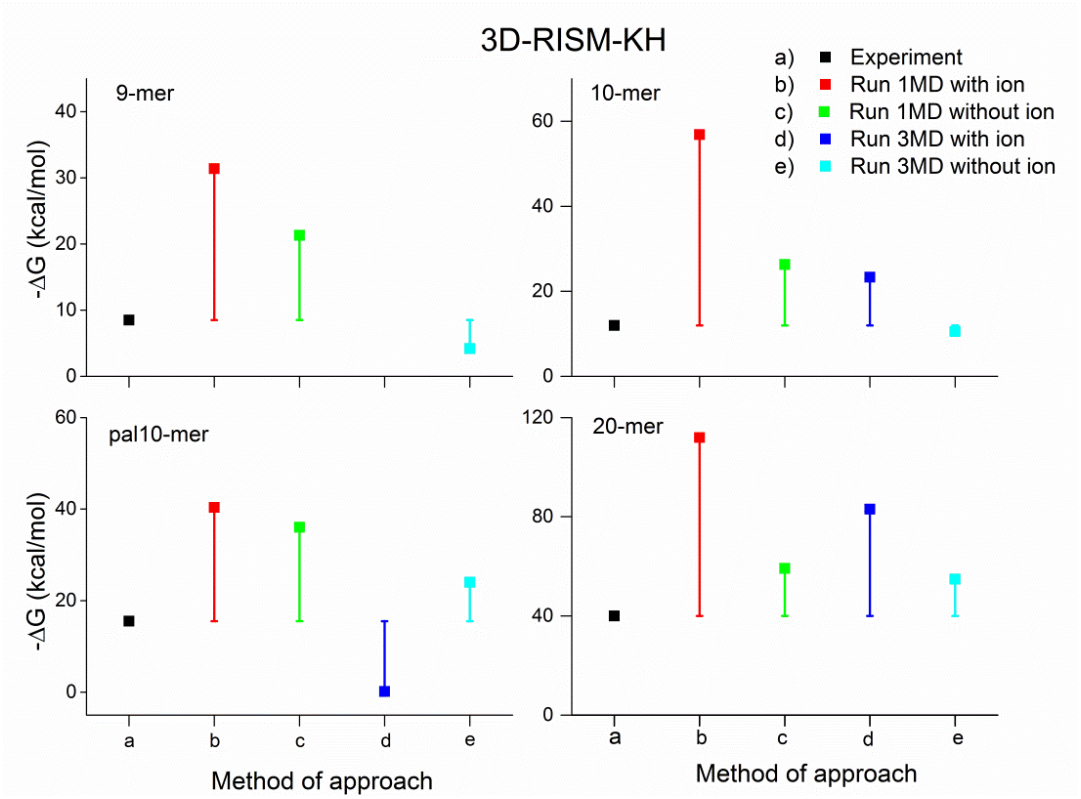

Figure 3-19 Oligonucleotide binding energies calculated using the 3D-RISM-KH method with "Run 1 MD" and "Run 3 MD" approaches with and without neutralizing ions, compared against experimental binding energies using minus error bars.

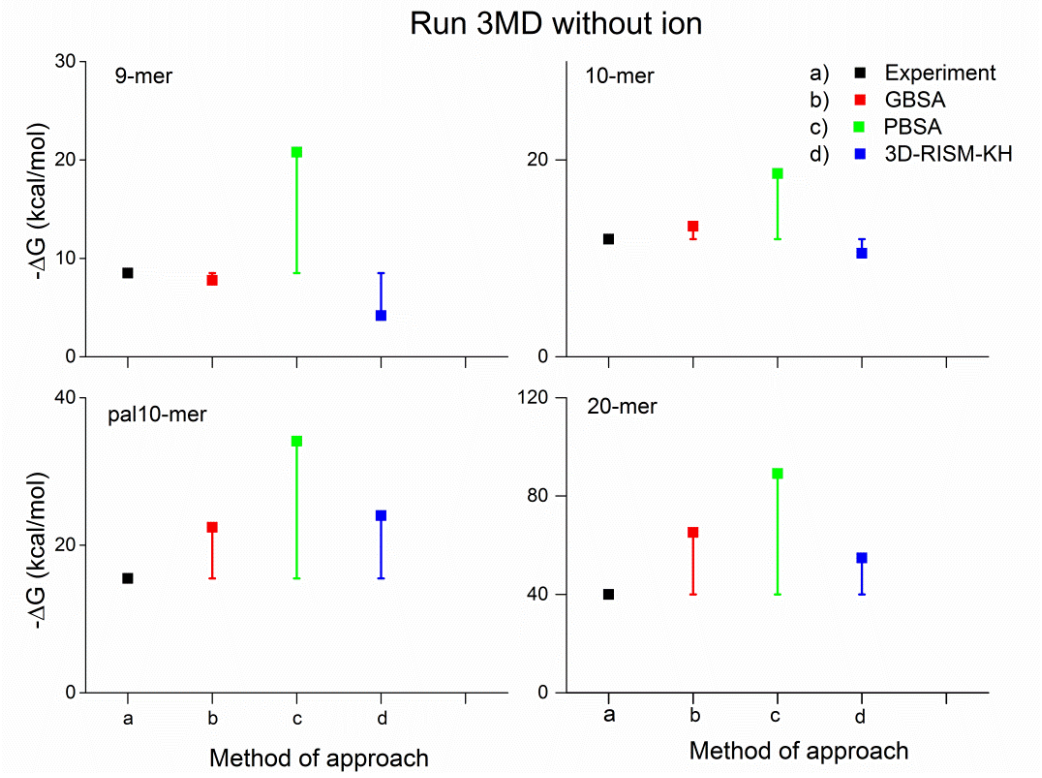

Figure 3-20 Binding energies calculated using GBSA, PBSA, and 3D-RISM-KH methods, without counter ions compared against experimental binding energies using minus error bars.

Table 3-11 Oligonucleotide binding energy obtained from Run 3 MD approach without counter ions[a]

	9-mer	10-mer	pal10-mer	20-mer	Correlation Coefficient (r^2)
$\Delta G_{bind,GBSA}$	-7.8	-13.2	-22.4	-65.1	0.99
$\Delta G_{bind,PBSA}$	-20.8	-18.6	-34.0	-89.0	0.99
$\Delta G_{bind,3DRISMKH}$	-4.1	-10.5	-24.0	-54.7	0.98
$\Delta G_{bind,Expt}$	-8.5	-11.9	-15.5	-40.0	1.00

[a]All energy values are in kcal/mol.

The binding energies obtained for "Run 3 MD" approach without counter ions by using GBSA, PBSA and 3D-RISM-KH for solvation free energy calculation are shown in Table 3-11. Another graphical comparison the three methods after stripping neutralizing ions for post processing is depicted in Figure 3-20. Among the three methods, binding energies calculated using 3D-RISM-KH is closer to the experimental binding energies. The implicit solvation model which is phenomenological does not take account of hydrogen bonding and hydrophobic interactions, especially for complex systems. It is the nonpolar solvation energy part that gives an advantage to the 3D-RISM-KH compared to the SASA. Previous studies confirmed the failure of SASA to predict the non-polar contribution correctly [91, 109, 153, 154] . SASA is not well defined, and the entropic term is absent in continuum solvent. 3D-RISM-KH more accurately accounts for chemical functionalities of both biomolecules and solvent species by representing both electrostatic and non-polar features of the solvation structure such as hydrogen bonding, hydrophobicity, salt bridges and structural solvent.

3.4.5 Neutralizing ions for post-processing

The conditions of retained and stripped neutralizing ions during the GBSA post-processing step with experimental results for the oligonucleotide binding energy were compared. The results depicted in Tables 3-7 and 3-9, and in Figure 3-21, show that there was not much difference between results obtained with and without neutralizing ions. Results obtained in the presence of neutralizing ions show a better correlation coefficient ($r^2 = 0.98$) with experimental binding energy values than results obtained in the absence of neutralizing ions ($r^2 = 0.90$). Thus it can be concluded that sufficient and optimal conditions for calculating oligonucleotide binding energy include (i) a "Run 1 MD" simulation with GBSA post-processing, (ii) retention of neutralizing ions **(**based on correlation values with and without ions)**,** and (iii) use of the 3D-RISM-KH method rather than the SASA method to calculate the nonpolar solvation energy.

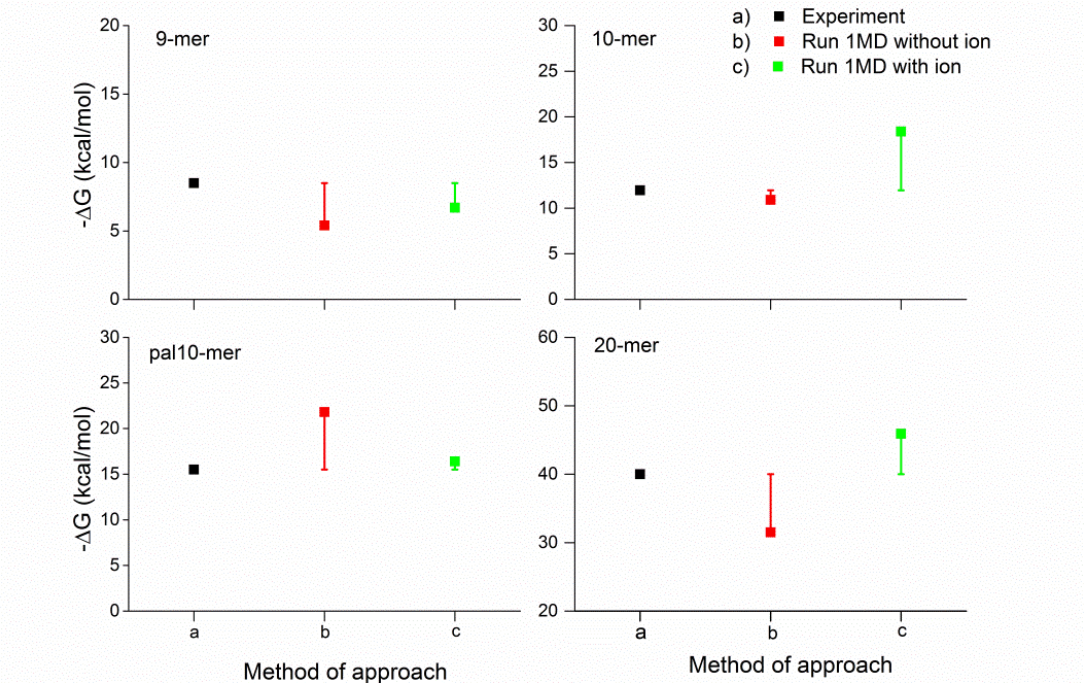

Figure 3-21 Calculated oligonucleotide binding energy compared with experimental binding energy using minus error bar. For the solvation energy, the polar part is from GBSA method and the nonpolar part is from 3D-RISM-KH.

3.4.6 DNA used for experimental work

Having established optimal conditions to measure the binding energy of double stranded DNA, I was prepared to model the DNA-assisted self-assembly of micro/nano chips. For this purpose I used a 16 base pair oligonucleotide with the sequence 5'-TTC AGC AAA TTT GGA G-3' (Figure 3-22) as was used in the experiment. Since the binding energy of this ds-DNA is not known, an MD simulation is performed and post-processed the nucleotide trajectories using the 3D-RISM-KH method. To avoid repetition, the complete procedure is not explained and many of the intermediate results are not presented; the final results are shown in Table 3-12.

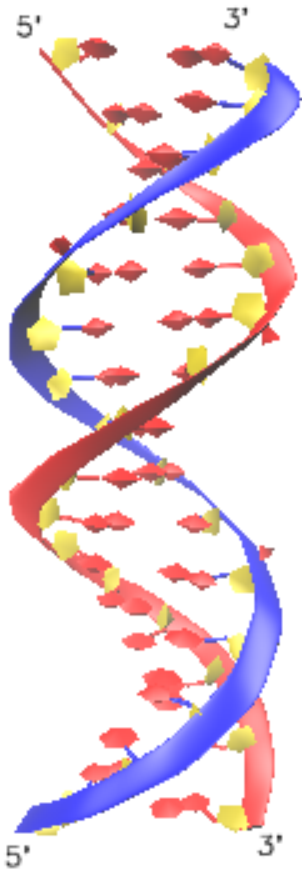

Figure 3-22 Structure of the 16 base paired ds-DNA (5'-TTCAGCAAATTTGGAG-3') used for the experimental work.

Table 3-12 Energies[a] obtained during the post-processing of the experimental ds-DNA.

Energies	Complex (ds-DNA)	Receptor (sstrand1)	Ligand (sstrand2)	Δ[b]
E_{ele}	2866	-325	-215	3408
E_{vdW}	-285	-97	-106	-8
E_{int}	1501	748	752	0
$\langle \mathbf{E_{MM}} \rangle$	4082	325	430	3326
$\langle \mathbf{TS_{MM}} \rangle$	667	343	348	-24
$\langle G_{sol,GBSA} \rangle$	-9692	-3124	-3161	-3405
$G_{pol,GBSA}$	-9738	-3153	-3190	-3394
$G_{np,SASA}$	46	28	28	-11
$\langle H_{GBSA} \rangle$	-5610	-2799	-2731	-79
$\mathbf{G_{GBSA}}$	-6277	-3142	-3079	-55
$\langle G_{sol,PBSA} \rangle$	-9876	-3203	-3240	-3432
$G_{pol,PBSA}$	-9922	-3231	-3268	-3421
$G_{np,SASA}$	46	28	28	-11
H_{PBSA}	-5794	-2878	-2810	-106
$\mathbf{G_{PBSA}}$	-6461	-3221	-3158	-82

[a]All energies are in kcal/mol.
[b]Contribution(ds-DNA) – contribution(sstrand1) – contribution(sstrand 2).

The ds-DNA structure was created using NAB, and a minimization procedure was performed followed by equilibrations steps for the explicit solvent model using the AMBER suite. The MD simulation was performed for 1 ns with a time step of 2 fs, and the ds-DNA was subjected to post-processing by extracting the trajectories of the single complementary strands from the complex using a "Run 1 MD" approach.

Using the 3D-RISM-KH method, the solvation energy part of the binding energy was obtained. Replacing the SASA $\langle \Delta G_{np,SASA} \rangle$ calculated nonpolar part with 3D-RISM-KH $\langle \Delta G_{np,3DRISMKH} \rangle$ using equation 3.10, a binding energy of -26.74 kcal/mol was calculated for the 16-base pair oligonucleotide at 298.15 ^{o}K and at 0

M salt concentration. The energies obtained from theoretical calculations for the 16-mer (5'-TTCAGCAAATTTGGAG-3') is summarized in Table 3-13 below.

Further we can observe that the energetic part of the binding energy $\langle \Delta E_{MM} \rangle + \langle \Delta G_{sol} \rangle$ is negative and supports the binding of the DNA strands whereas the entropy part $-\langle T\Delta S_{MM} \rangle$ is disfavoring the binding with a positive value. The entropy term for 9mer<10mer<16mer<20mer, from which we could infer that, as the length of the oligo sequence increases, the entropy of the system increases. This could be contributing to steric hindrance for DNA binding.

Table 3-13: Energies and the experimental condition terms for the DNA used for experiment.

Energies and the experimental condition terms	
Binding free energy, ΔG	-26.74 kcal/mol
Enthalpy, ΔH	-50.85 kcal/mol
Entropy, ΔS	-0.081 kcal/mol
Temperature, T	298.15 ^{o}K
Pressure, P	1 atm
Oligonucleotide concentration, C_o	1E-15 M

The ds-DNA fraction f helps us to determine what fraction of the ds-DNA is unwound at different temperatures. The DNA melting curve (Figure 3-23) is obtained using the following equations [39] 3.26 and 3.27 by calculating the equilibrium constant, K_{eq} using:

$$K_{eq} = e^{[\frac{\Delta S}{R} - \frac{\Delta H}{RT}]}, \tag{3.30}$$

where R is universal gas constant and ds-DNA fraction f given by:

$$f = \frac{1 + C_o K_{eq} - \sqrt{1 + 2C_o K_{eq}}}{C_o K_{eq}}, \tag{3.31}$$

where C_o is the oligonucleotide concentration.

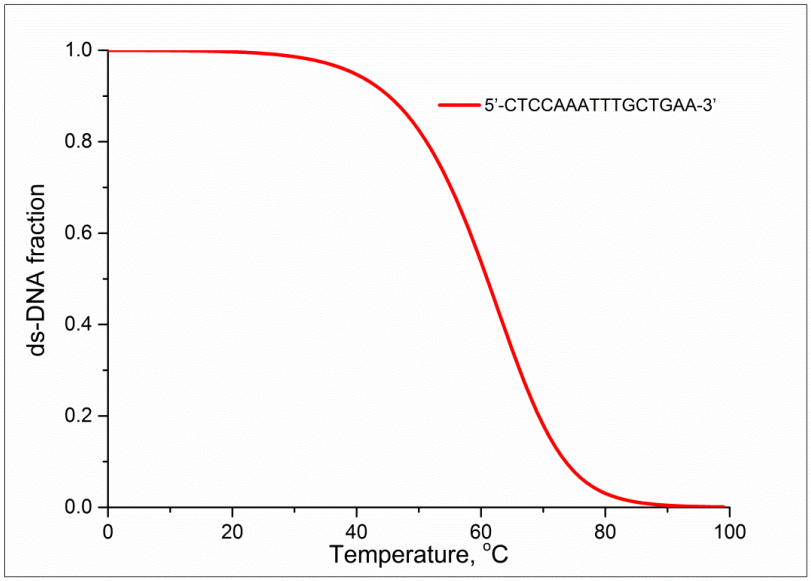

Figure 3-23 Temperature dependence of the 5'-CTCCAAATTTGCTGAA-3 ds-DNA unwinding.

The calculations were performed using MATLAB scripts (Appendix IV) and is based on obtained enthalpy, ΔH and entropy, ΔS values of 5'-CTCCAAATTTGCTGAA-3 ds-DNA at an expected oligonucleotide concentration of 1 fM and using the universal gas constant R (1.987 10^{-3} kcal/mol-K). The melting or the unwinding of the ds-DNA occurs gradually as the temperature of the system increases from 40 °C to 80 °C. So to perform the simulated hybridization with heating and cooling cycles, a temperature between 50 °C to 60 °C seems optimum.

3.4.7 The effect of salt concentration on the ds-DNA

The MMGB/PBSA was utilized to detect changes in the DNA binding energy in the presence of different salt concentrations. The results are presented in Table 3-14.

Table 3-14 MM/GBSA calculations of 16-mer ds-DNA binding energy values obtained at different salt concentrations.

Salt (Na^+) Concentration (M)	$\Delta G_{bind,GBSA}$ (kcal/mol)
0.0	-55.43
0.1	-90.09
0.15	-92.90
0.2	-94.66
0.3	-96.77
0.4	-97.98
0.5	-98.74
0.6	-99.25
0.8	-100.07
1.0	-100.24
1.1	-100.36
1.2	-100.45
1.5	-100.62

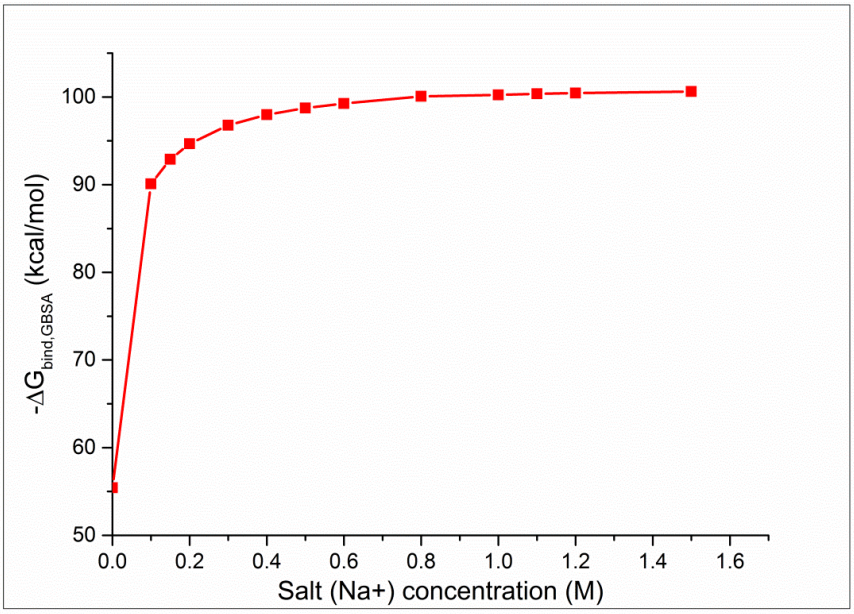

Figure 3-24 Effect of salt (Na+) concentration on binding energy found using GBSA of 16-mer ds-DNA (5'-CTCCAAATTTGCTGAA-3').

Figure 3-24 shows that the 16-mer ds-DNA binding energy increases with salt concentration. A large increase in binding energy was observed when the salt concentration was increased from 0 to 0.3 M. Further increases in salt concentration from 0.4 M up to 1.5 M produced only slight increases in DNA

binding energy. So a 0.3 M salt concentration is chosen as optimum salt concentration for the experiment.

MELTING software based on a semi-empirical algorithm [40] was used to study the effect of salt concentration on the melting temperature of the 16-mer ds-DNA. To explain the effect of G-C content on melting, our experimental 16-mer ds-DNA is compared with another 16 G-C and 16 A-T base pairs. For the three oligonucleotide sequences shown in Table 3-15, as the salt concentration increased, the melting temperature of the DNA sequence needed for the unwinding of the ds-DNA also increased. The effect of salt concentration was constant from 0.5 M to 1.5 M for all three DNA sequences.

Figure 3-25 shows the effect of salt concentration on the melting temperatures of ds-DNA: 16 base pairs (5'-CTCCAAATTTGCTGAA-3'), 16 GC base pairs (5'-GGGGGGGGGGGGGGGG-3'), and 16 AT base pairs (5'-AAAAAAAAAAAAAAAA-3'). Binding of the 16 GC base pairs was stronger than binding of 16 AT base pairs, thus a higher temperature was required for the unwinding of the 16 GC base pairs. GC content in the DNA sequence increases the temperature needed for melting the ds-DNA. This is expected since the GC base pair forms three hydrogen bonds as opposed to the two hydrogen bonds formed by an AT base pair.

Table 3-15 Melting temperature of 3 ds-DNAs: 16-mer, 16 GCs, and 16 ATs obtained at different salt concentrations.

Salt (Na+) concentration (M)	Temperature (^{o}C)		
	5'-CTCCAAATT-TGCTGAA-3	5'-GGGGGGGGG-GGGGGGG-3'	5'-AAAAAAAAA AAAAAAA-3'
0.01	60	94	45
0.1	65	97	50
0.2	68	99	53
0.3	69	99	55

0.4	70	100	56
0.5	71	100	57
0.6	71	100	58
0.8	72	100	58
1.0	72	100	59
1.2	72	100	60
1.5	73	100	60

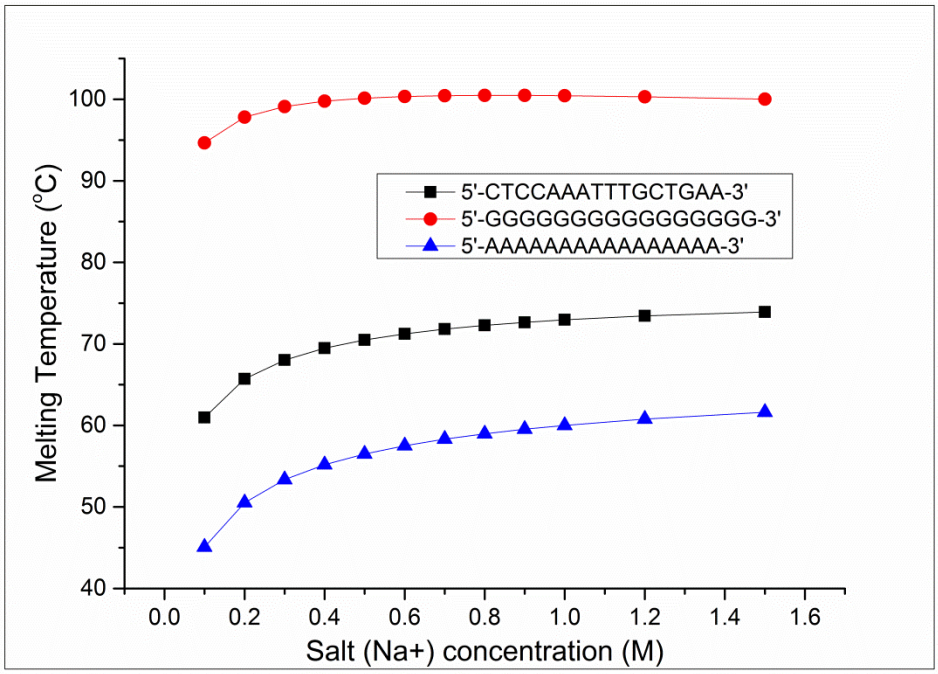

Figure 3-25: Melting temperature of ds-DNA samples and effect of salt concentration on ds-DNA melting temperatures.

After GBSA post-processing, binding energies of -48.82 kcal/mol for oligonucleotide binding in the presence of K^+ ions (Table 3-16) and -55.43 kcal/mol for oligonucleotide binding in the presence of Na^+ ions were determined. Thus, neutralization with K+ or Na^+ ions favours the binding of the DNA strands.

Table 3-16 Energies obtained for ds-DNA with K+ ions.

Energies	Complex (ds-DNA)	Receptor (sstrand1)	Ligand (sstrand2)	Δ
E_{ele}	2829	-338	-232	3400
E_{vdW}	-288	-97	-07	-83

E_{int}	502	749	752	0
$\langle \mathbf{E_{MM}} \rangle$	4043	313	412	3317
$\langle \mathbf{TS_{MM}} \rangle$	667	343	348	-24
$\langle G_{sol,GBSA} \rangle$	-8762	-2639	-2731	-3390
$G_{pol,GBSA}$	-8808	-2667	-2760	-3379
$G_{np,SASA}$	45	28	28	-11
$\langle H_{GBSA} \rangle$	-4719	-2326	-2319	-73
$\mathbf{G_{GBSA}}$	-5386	-2669	-2667	-49
$\langle G_{sol,PBSA} \rangle$	-9822	-3182	-3223	-3417
$G_{pol,PBSA}$	-9868	-3210	-3251	-3405
$G_{np,SASA}$	45	28	28	-11
H_{PBSA}	-5779	-2869	-2811	-100
$\mathbf{G_{PBSA}}$	-6446	-3212	-3159	-76

[a]All energies are in kcal/mol.
[b]Contribution(ds-DNA) – contribution(sstrand1) – contribution(sstrand 2).

3.5 Conclusions

We calculated the binding energy of the DNA strands using 3D-RISM-KH and compared with the continuum solvation models to validate the approach. The 3D-RISM-KH molecular theory of solvation rendered a value for the binding energy of DNA strands in solution that was closer to the experimental value than the values obtained with GBSA and PBSA continuum solvation models. This was due to a better first principle description of nonpolar terms for the solvation free energy in the statistical-mechanical 3D-RISM-KH method. The 3D-RISM-KH method represents the hydration of the solute molecule more accurately as compared to the continuum solvation model, which contributes to the exactness of the solvation energy calculation.

In addition, I investigated “Run 1 MD” and “Run 3 MD” approaches to find the binding free energy for double stranded oligonucleotides. In the “Run 1 MD” approach, the complex formation of two single DNA strands was simulated and

post-processed the solvation free energy of the double stranded DNA complex. To obtain the solvation free energies of unbound DNA strands, the structure of the DNA double stranded complex was split up and post-processed the two single DNA strands, a widely accepted practice in the bio-molecular modeling field. In the "Run 3 MD" approach, I obtained the DNA binding energy more accurately by separately simulating and post-processing the two single DNA strands and the bound DNA complex. Compared to the "Run 1 MD" approach, the "Run 3 MD" approach yielded a DNA binding energy in considerably better agreement with experimental values. The binding energy calculation was performed with and without counter ions. The energy values obtained without counter ions taken into account implicitly in the solvation model were in better agreement with experimental values than results obtained with counter ions removed.

Unlike phenomenological modeling tools, this MM/3D-RISM-KH approach helps us to understand the mechanism. In addition, other approach like MD simulation requires long simulation run to get the distribution of the ions unlike 3D-RISM-KH theory. The decomposed energy terms helps us to infer the various contributing factors favoring and against the DNA strands binding. The binding energy (ΔG = -26.74 kcal/mol) of the ds-DNA used for our experiment is calculated using 3D-RISM-KH approach and the DNA melting curves were plotted to understand the role of temperature to perform simulated hybridization. The entropy of the system was showing increase with the length of the oligo sequence. This could be used as a measure to the steric hindrance effect. The ds-DNA starts unwinding at a system temperature of around 40 ^{o}C and completely separates the bands above 80 ^{o}C. A temperature between 50 ^{o}C and 60 ^{o}C was chosen for

simulated hybridization. The effect of the various salts at different concentration is also investigated to aid the experiment. Salts help to stabilize the DNA structure at the solid surface thereby improving the efficiency of the DNA binding. As the salt concentration increases, the binding energy of the ds-DNA also increases and then ineffective when the salt concentration is more than 0.3 M. From this, we could infer that the salt ions have a good role to play with the conformation of the DNA strands to promote the self-assembly by lowering the role of steric hindrance by maintaining a stabilized DNA structure.

4 Experimental Work

4.1 Introduction

Our experiments with DNA-assisted self-assembly of electronic devices were performed to determine contributing factors that would help in the commercialization of this technology. The experimental procedure comprised (1) host substrate preparation, (2) preparation of the model micro/nano silicon chips/devices for assembly on the substrate, (3) functionalization of the host substrate and devices with DNA strands, and (4) DNA-assisted self-assembly of the micro/nano silicon chips/devices on the host substrate (Figure 4-1).

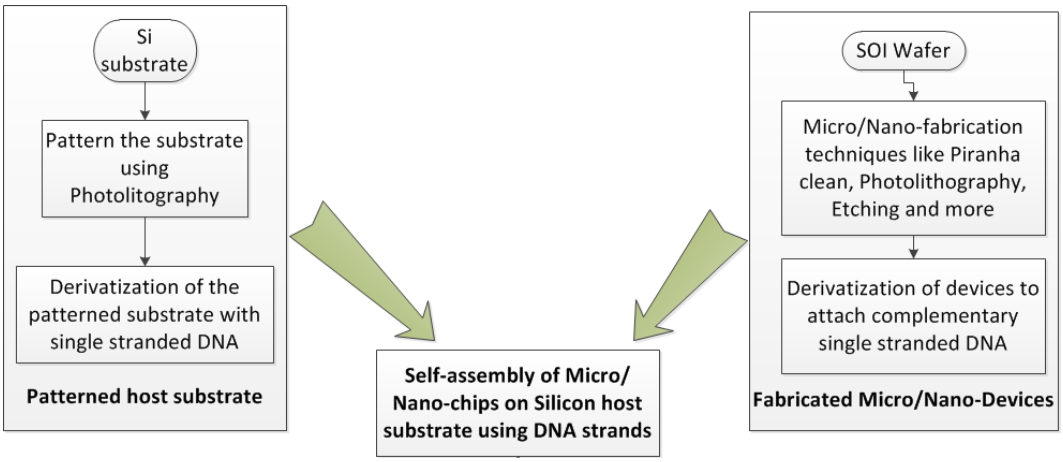

Figure 4-1 Experimental steps for DNA-assisted self-assembly of Si nanochips on a host substrate.

The covalent and selective attachment of DNA to a Si substrate for the alignment of electronic devices can be accomplished in several ways [62, 63, 155]. The attached DNA must be patterned appropriately to better align the nanochips to the substrate. Nanochips can be functionalized by covalent attachment to DNA strands that are complementary to the DNA strands on the Si substrate. The parameters for the attachment of nanochips to the substrate were evaluated and

the behavior of the process was monitored under various conditions. Characterization techniques were utilized to validate the success of each experimental step. Section 4.2 provides an introduction to the microfabrication and experimental characterization techniques used in the thesis. The work described in this chapter has been published in Journal of Nanotechnology and Nanoscience [71].

4.2 Equipment and Processes

4.2.1 Micro/nanofabrication techniques

Micro/nanosystems—small, integrated systems that perform electrical, optical, magnetic, mechanical, chemical and biological functions—can be fabricated to impose a reproducible structure on a surface through a series of deposition, etching, and patterning steps. The various micro/nanofabrication techniques used to fabricate the silicon microtiles as model device and to prepare the host substrate for self-assembly experiments are briefly discussed below.

4.2.1.1 Piranha cleaning

Piranha solution — a 3:1 ratio of sulfuric acid (H_2SO_4) and hydrogen peroxide (H_2O_2) — a highly corrosive and a powerful oxidizer is used to clean and remove organic and metallic contaminants on silicon wafers. The preparation of a piranha bath involves exothermic reactions that exceed 100 °C; it was performed on a specific wet deck at the nanoFAB facility at the University of Alberta (Figure 4-2).

Figure 4-2 Wet deck at the University of Alberta, used for piranha preparation [156].

4.2.1.2 Photolithography

Lithography is used for transferring a square grid pattern to a layer of photoresist which is then used as a mask for a subsequent lift-off or etch step. HPR-504 from FujiFilm [157], a common positive photoresist (Figure 4-3), is used in all experiments.

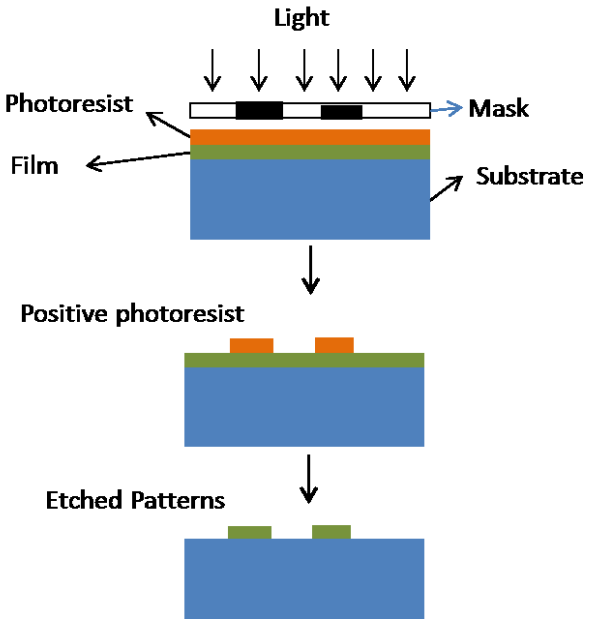

Figure 4-3: Flow diagram of a photolithography process. Based on [158].

The photoresist was applied onto the Si wafer by spin-on application followed by a soft bake at < 100 °C on a hot plate (Figure 4-4).

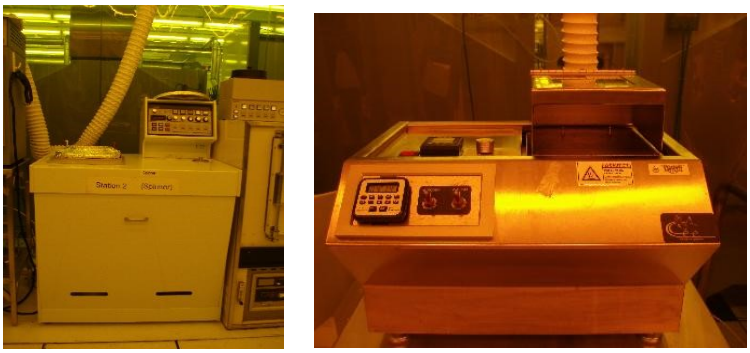

Figure 4-4 Solitec spinner [159] (left) and CEE hot plate [160] (right) in nanoFAB, University of Alberta [156].

Hexamethyl-disilazane (HMDS), an adhesion promoter was previously applied to the substrate using a vapor source to improve the adhesion of the photoresist to the Si surface (Figure 4-5, left).

Figure 4-5 YES HDMS oven (left) and ABM mask aligner (right) at nanoFAB, University of Alberta [156].

After mild heating to drive off solvents, the substrate is exposed to a pattern of intense UV light (365 nm) for 1.9 s using a mask aligner (Figure 4-5, right). After exposure to UV light, the photoresist is developed in a bath using Shipley 354

Developer. The photoresist can be stripped off using acid or organic solvent after the following etch steps.

4.2.1.3 Etching

After the creation of the pattern using the photoresist, the pattern was transferred to the underlying thin films including a sacrificial SiO_2 layer with a standard etch process like buffered oxide etching (BOE). In this experiment, a Silicon-on-Insulator (SOI) wafer with a buried sacrificial layer of SiO_2 is used, which is later etched for the release of the Si devices from its top (device) layer.

BOE is performed using a 10:1 mixture of 40% NH_4F and 49% HF. Reactive ion etching (RIE), which uses chemically reactive plasma to remove material deposited on the Si wafer (Figure 4-6), is used to remove contaminants from the substrate after photolithography.

Inductively coupled plasma reactive ion etching (ICPRIE), another type of RIE system, was used to perform the Bosch process. The Bosch process involves two steps (1) coating the entire surface with polymer using a teflon-like substance formed in the plasma from C_4F_8 gas and (2) SF_6 plasma etching of the polymer in the bottom of the trench, followed by the layer below the polymer.

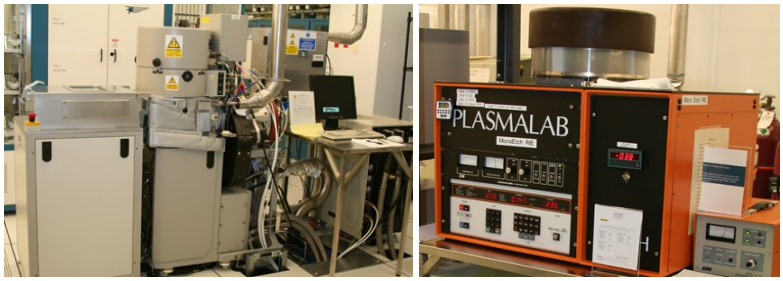

Figure 4-6 Surface Technology Systems ICPRIE (left) and microetch RIE (right) at nanoFAB, University of Alberta [156].

Bosch etching was used for deep etches such as removing the handle wafer from the back of our SOI substrate with good selectivity and also suitable for backside silicon etching.

In order to remove the bulk silicon on the backside of the SOI substrate XeF_2 etching was used for dry isotropic Si etching [161] (Figure 4-7). A member of the fluorine based silicon etchants, the system uses XeF_2 gas obtained from rock salt-sized XeF_2 crystals. The Si/XeF_2 reaction is:

$$2\,XeF_2 + Si \rightarrow 2\,Xe + SiF_4. \qquad \text{Equation 4-1}$$

The reaction is exothermic and the substrate temperature increases to hundreds of degrees. XeF_2 gas forms hydrogen fluoride (HF), a safety hazard, in the presence of water vapor. The 500 μm of bulk silicon was etched with 300 etch cycles by setting a base pressure of 150 mTorr and using a pulse time of 60 s for expansion and etching.

Figure 4-7 XeF_2 etching system at nanoFAB, University of Alberta [156].

4.2.1.4 Evaporation

For preparing the gold patterned host substrate, thin films of chromium and then gold were deposited onto the silicon substrate using evaporation, a physical vapor deposition technique (Figure 4-8). The E-beam evaporation available at the

nanoFAB facility, University of Alberta, was used deposit a 10 nm chromium layer followed by a 50 nm layer of gold. The thicknesses of the thin films were monitored using quartz crystal sensor. The chromium layer was deposited first to assist in the adhesion of the gold layer.

Figure 4-8 Electron beam evaporation system at nanoFAB, University of Alberta [156].

4.2.2 Self-assembled monolayer

Self-assembled monolayers (SAMs) are highly ordered two-dimensional structures that form spontaneously on a variety of surfaces by adsorption of organic molecules [162]. They result in dense reproducible surface coatings with predictable chemical functionality. The most commonly used SAMs are alkyl silanes (on oxide surfaces) and sulfur-terminated alkanes (on gold surfaces) as depicted in Figure 4-9. In 1983, Allara and Nuzzo at Bell Laboratories produced the first gold thiolate [163].

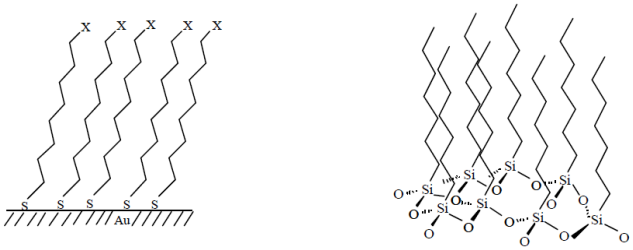

Figure 4-9 Gold thiolate monolayer (left) and alkyl silane (right) monolayer.

The Si wafer surface was activated prior to the self-assembly to clean the surface and maximize the number of silanol groups at the surface. This can be achieved using strong acids or by exposure to an oxygen plasma which renders the surface hydrophilic and prone to the formation of a thin water layer. Traces of water have been found to be essential for the formation of well packed monolayers [162, 164]. SAMs can also be produced through physical vapor deposition or by dipping the surface activated substrate in solution. Aggregates form much faster in an aqueous solution but do not form a smooth monolayer.

SAMs are compatible with silicon technology and permit the use of various characterization techniques such as fluorescence spectroscopy. Contact angle goniometry is a characterization technique that provides information on the polarity, roughness, and order of a SAM. The SAM thickness can be determined using ellipsometry. Elemental composition can be gathered using x-ray photo spectroscopy (XPS) and secondary ion mass spectroscopy (SIMS). Atomic force microscopy (AFM) helps to measure the surface topology of the monolayer.

4.2.3 Characterization techniques

The characterization techniques I used to verify each experimental step for the attachment of the DNA strands onto the substrate are described in sections 4.2.3.1–4.2.3.5.

4.2.3.1 Contact angle measurement

The contact angle method [165] was used to characterize the formation of the SAM on the Si substrate surface.

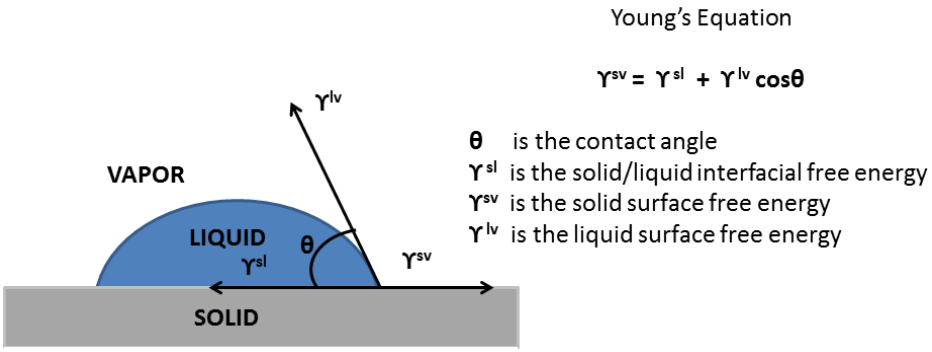

Figure 4-10 The surface energy of a drop of liquid on a solid surface can be estimated using Young's equation [166].

A drop of liquid on a solid surface is surrounded by a vapor. If these three phases can be considered to be in thermodynamic equilibrium, the surface energy of a liquid can be calculated using Young's equation (Figure 4-10) which describes the interactions between the forces of cohesion and adhesion.

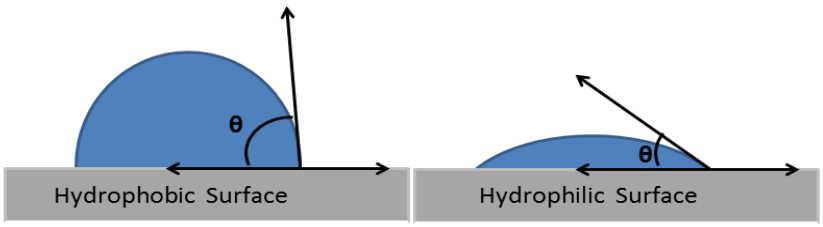

Figure 4-11 Contact angles on hydrophobic and hydrophilic surfaces [166] .

Surface defects, dislocations, and impurities can often influence the size of the contact angle, so we can use it to validate the quality of the surface and the SAM. The presence of organic contaminants lower the wetting and show higher contact angles on an originally hydrophilic surface, so the surface needed to be cleaned to remove these organic contaminants (Figure 4-11). To accomplish this, I performed a piranha cleaning on the control Si substrate samples. The contact angle measurement system (First 10 Å) in the nanoFAB facility at the University of Alberta, shown in Figure 4-12 was used.

Figure 4-12 First 10 Å contact angle measurement system at nanoFAB, University of Alberta [156].

4.2.3.2 X-ray photoelectron spectroscopy

X-ray photoelectron spectroscopy (XPS) [167, 168], which detects the chemical composition on the surface of a material by bombarding it with X-rays (typically Al Kα at 1487 eV) and measuring the kinetic energy and number of photoelectrons ejected from the top ~30 Å of the sample is used to characterize the formation of the self-assembled monolayer and attachment of the bifunctional cross linker, SSMCC. To confirm the formation of the SAM on the Si substrate, a sample without any pattern was prepared and another piranha cleaned Si substrate was used as a control. If XPS detects the presence of the nitrogen atom in the amine group of the SAM, this could confirm its presence. In addition, to characterize the SSMCC attachment, I used XPS to find the presence of C=O bond in the linker molecule. The samples were analyzed with XPS at Alberta Centre for Surface Engineering and Science (ACSES), University of Alberta, using the AXIS ULTRA (Figure 4-13).

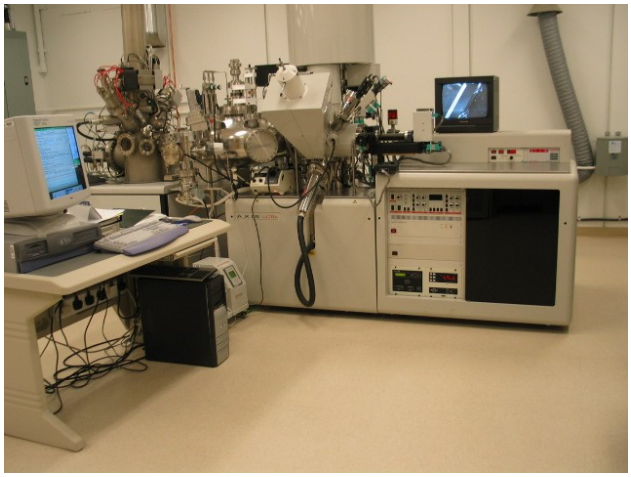

Figure 4-13 AXIS ULTRA XPS system at ACSES, University of Alberta [156].

4.2.3.3 Time of flight-secondary ion mass spectroscopy

ToF-SIMS [169, 170] which uses a pulsed ion beam to sputter molecules for surface analysis is used to characterize the attachment of the DNA strands onto the Si and gold patterned substrate. The mass spectrum of emitted fragments helps to confirm the surface composition.

The high mass range capability of ToF-SIMS enables us to perform an elemental composition analysis that can determine the presence of Si, Au, and various atom groups in oligomers. DNA strands were attached to Si and Au patterned substrate samples. I looked for the presence of Si, Au, CNO, PO_2, and PO_3 to validate the DNA attachment process. For a patterned Si substrate, Si should be the predominant signal in regions where no DNA is present whereas CNO, PO_2 and PO_3 groups are expected for regions rich with DNA. The ION-TOF IV instrument

at ACSES, University of Alberta (Figure 4-14) was used to characterize our samples using ToF-SIMS technique.

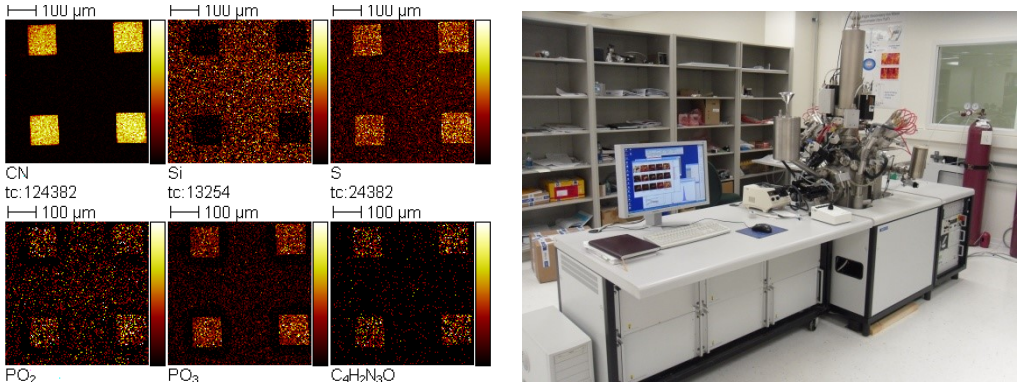

Figure 4-14 Lateral distribution of DNA fragments over a patterned Si substrate (left). Each image maps our sample at an energy characteristic of a different chemical bond. ION-TOF IV instrument at ACSES, University of Alberta (right) [156].

4.2.3.4 Fluorescence microscopy

"Fluorescent chromophores" which absorb light at specific wavelength(s) and produce lower energy photon-excited electrons, have become an indispensable tool [171] for the imaging of biological samples, and were employed to characterize the attachment of DNA onto the host substrate and to confirm DNA hybridization with an Olympus IX81 fluorescence microscope (Figure 4-15) in the National Institute for Nanotechnology (NINT).

Figure 4-15 Olympus IX81 fluorescence microscope at NINT.

The AlexaFluor 546 fluorophore attached to the 5’ end of one of the DNA strands [5' (Alexa546) (C6-NH) TTC AGC AAA TTT GGA G (Spacer9) u (C3-SH) 3'] were used to characterize the attachment of the oligonucleotides (“oligos”) onto the substrate as well their hybridization with the complementary DNA strand functionalized to the substrate surface. A 1 μmole of the single stranded DNA labeled with Alexa Fluor 546 (Figure 4-16) fluorophore (peak emission at 573 nm wavelength, peak absorption at 556 nm) was obtained from Trilink Biotechnologies Inc, as desalted. Desalting removes the small-molecule impurities created as byproduct during the oligo synthesis. The AlexaFluor 546 attached oligos were aliquoted using 1 mL of triethanolamine (TEA) buffer to get 1000 μM oligo concentration and stored in dark centrifuge tube covered with aluminum foil before use to avoid photobleaching.

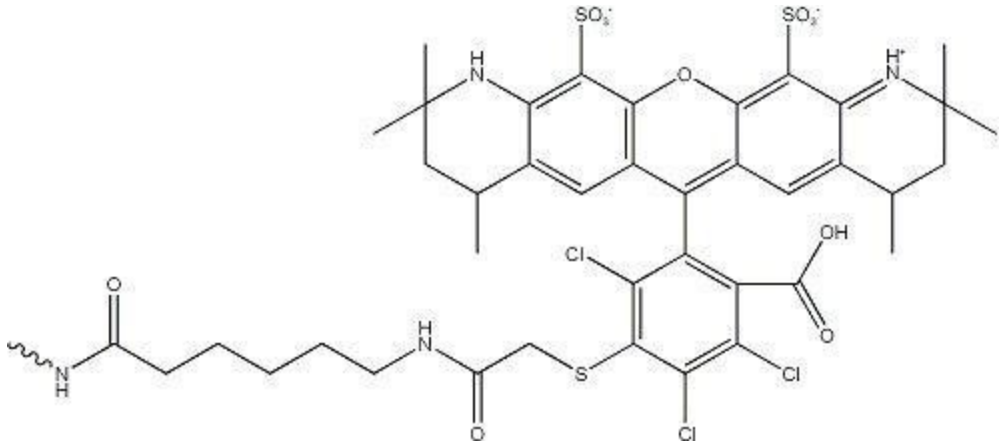

Figure 4-16 Structure of the Alexa Fluor 546 fluorophore [172].

4.2.3.5 Scanning electron microscopy

Scanning electron microscopy (SEM), [173] which employs electrons instead of light for illumination, is used to obtain high resolution images of the substrate after self-assembly. A field emission (cold cathode) scanning electron microscope (JAMP-9500F, Figure 4-17) at ACSES, University of Alberta, is used to analyze the self-assembled gold nanoparticles on the patterned host substrate.

Figure 4-17 JAMP-9500F scanning electron microscope at ACSES, University of Alberta [156].

4.3 Experimental Procedure

4.3.1 Fabrication of model silicon nanochips

The micro/nanosilicon devices/chips for conducting the experiments were fabricated using a process developed by Ng and Dew [92] starting from a 100 mm (100)-oriented silicon-on-insulator (SOI) wafer and proceeding through the steps as explained below and shown in Figure 4-18 .

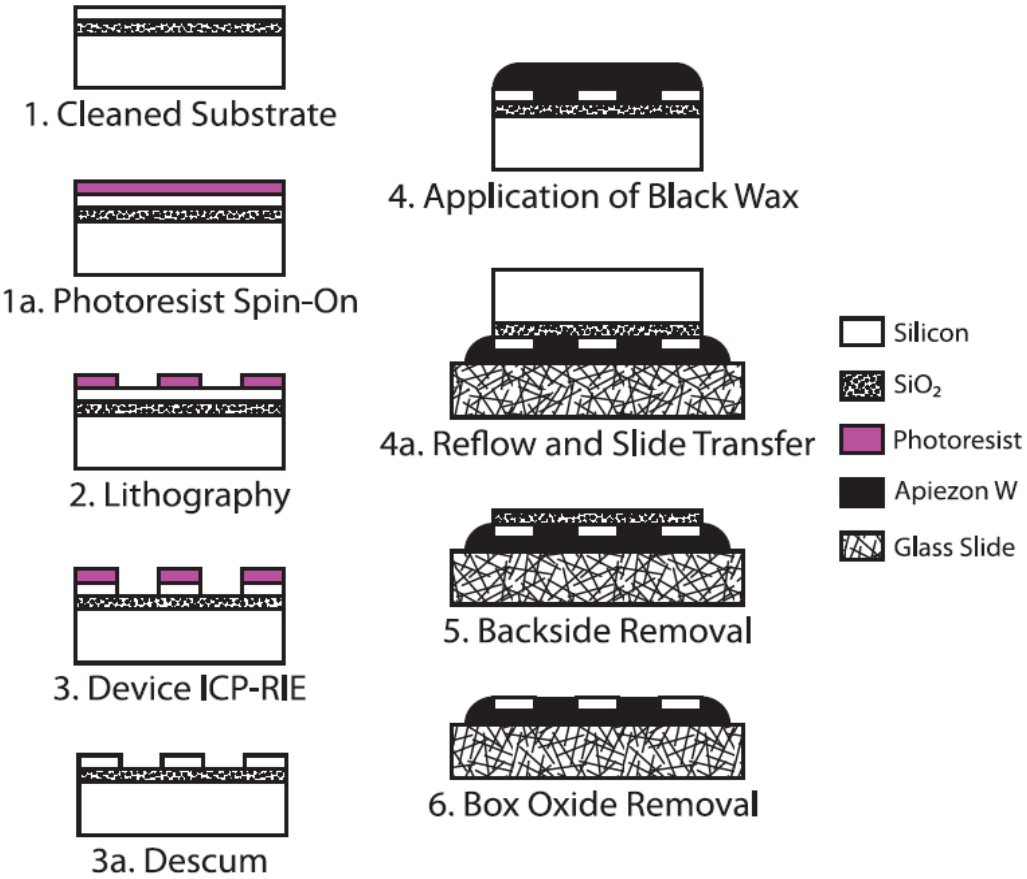

Figure 4-18 Process flow of device production.

(1) SOI substrates were diced 1 x 1.5 cm and cleaned using piranha solution. (1a) HPR-504 photoresist was applied using spin-on. (2) The photoresist was patterned using photolithography. (3) The Si device layer was etched using ICP-

RIE. (3a) The photoresist was stripped by sonication in an acetone bath for 10 mins. (4) Molten wax at 120°C was spread on the entire top surface of substrate. (4a) the substrates were placed wax-down on top of glass slides at room temperature. (5) The backside bulk silicon was removed using XeF_2 dry etching. (6) The box oxide was removing using buffered oxide etch (BOE) to release the Si devices. Before device release, the probe DNA strands need to be covalently attached to the Si device surface. After the removal of the backside bulk Si and the box oxide, the Si devices are embedded in black wax which acts as a carrier for the devices with the Si surface exposed to perform further steps including the formation of the SAM and the attachment of the DNA strands, themselves. Once the Si device surface with the DNA strands is characterized, the devices can be released using TCE solvent. In this way, steps involving the exposure of the attached DNA strands to etch solvents are avoided.

The following steps were performed to covalently attach DNA to the Si device chips.

The steps involved in fabricating the Si device chips are shown in Figure 4-19. The Si nanochips were functionalized by covalent attachment to the DNA strands having a complementary sequence to the DNA on the host substrate.

(1) A 100 mm silicon-on-insulator (SOI) wafer with (100) orientation and 2 μm Si device layer, 0.5 μm box oxide, and 500 μm backside silicon, was diced to substrate/tiles of 1 × 1.5 cm in size using the Disco diamond saw in the nanoFAB facility at the University of Alberta along the (100) crystal planes. These substrates were piranha cleaned (3:1 mixture of 96% H_2SO_4 and 30% H_2O_2) to remove

organic contaminants on the surface. Native oxide removal was performed with a buffered oxide etch using a 10:1 mixture of 40% NH_4F and 49% HF for 90 s followed by a dump-rinse and N_2 drying. The substrate was further dehydrated and primed with HMDS.

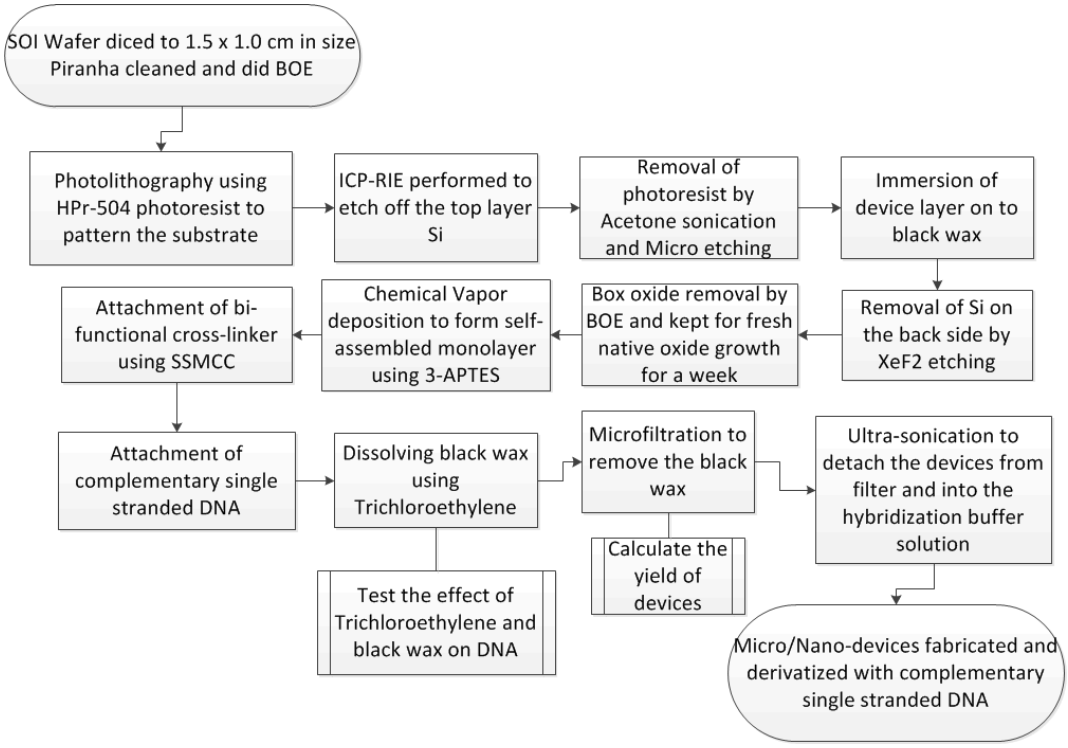

Figure 4-19 Flowchart explaining the steps involved in the fabrication of Si device chips.

(1a) HPR-504 positive photoresist was applied to the substrate using a Solitec spinner to achieve a ~1.5 μm thick layer and the coated substrate was soft-baked in a vacuum hot plate for 90 s at 110 °C.

(2) The photoresist was patterned by performing photolithography using a 1.9 s exposure of UV (365 nm) light followed by a 20 s developing step using a Shipley 354 developer. The chrome mask was patterned after the various patterns of

devices, including different sized squares. I used mainly 25 μm and 100 μm squares for the experiments.

(3) Etching was performed using an ICPRIE system to pattern the 2 μm Si device layer using the Bosch recipe.

(3a) The photoresist was removed after the ICPRIE etching was performed using acetone sonication for 10 min at 50 °C followed by a drying step using N_2. To ensure the removal of residues from the Bosch polymer, an etching step using oxygen plasma was performed with a PlasmaLab's RIE machine for 20 min.

(4) Molten black wax (Apiezon W) (~ 20 gm) was spread at 120 °C over the entire top surface of the substrate.

(4a) Substrates were placed wax-down on top of a glass slide at room temperature followed by heating (~ 120 °C) to reflow the wax and settle the substrate onto the glass slide.

(5) A XeF_2 dry etch was performed to remove the backside bulk 500 μm thick silicon. To avoid the presence of native oxide and moisture content, a quick BOE step followed by a quick 90 s vacuum bake was performed before the XeF_2 etch. Around 350 XeF_2 etch cycles and ~ 25 hours were needed to completely remove the 500 μm thick bulk Si.

(6) A 20 minute buffered oxide etch was performed to remove the 0.5 μm thick box oxide layer, followed by a dump-rinse and drying under a stream of N_2. To avoid etching the glass slide itself, blue tape was used to cover the glass portion.

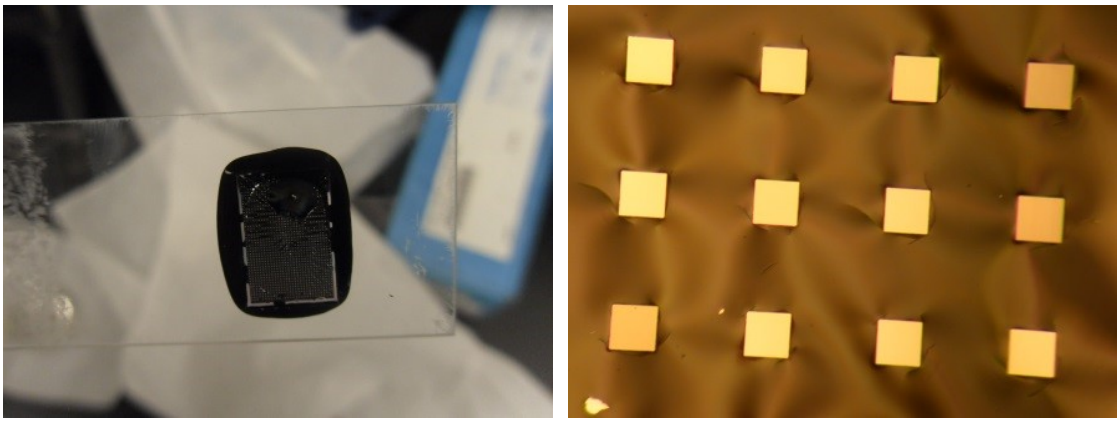

Figure 4-20 Sample after XeF_2 etching, showing the black wax (left) and 100 μm devices (right).

After obtaining the Si devices immersed in black wax (Figure 4-20), the tiles were freed by dissolving the black wax using trichloroethylene. Before freeing the devices from the tiles, the attachment of the SAM was performed followed by the covalent attachment of DNA, which is described in more detail in section 4.3.3.

The list below describes the procedure I used to free the Si tiles from the black wax.

1. The glass slides with devices were dipped in a 30 mL beaker containing trichloroethylene (TCE) for 5 min. TCE dissolved the black wax and the devices moved into the TCE (Figure 4-21).

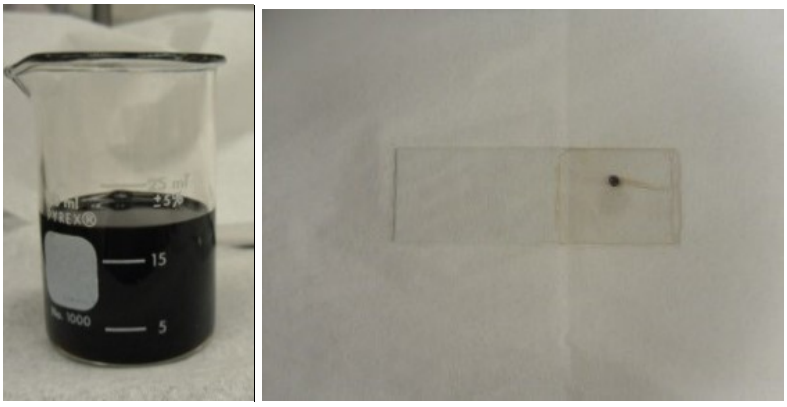

Figure 4-21 Black wax on glass slides with devices was dissolved with trichloroethylene (left). Glass slide after black wax was removed (right).

2. The devices in the TCE were prefiltered through a stainless steel mesh (metal grid) apparatus (Figure 4-22) followed by microfiltration using vacuum finally through a membrane filter (Figure 4-23).

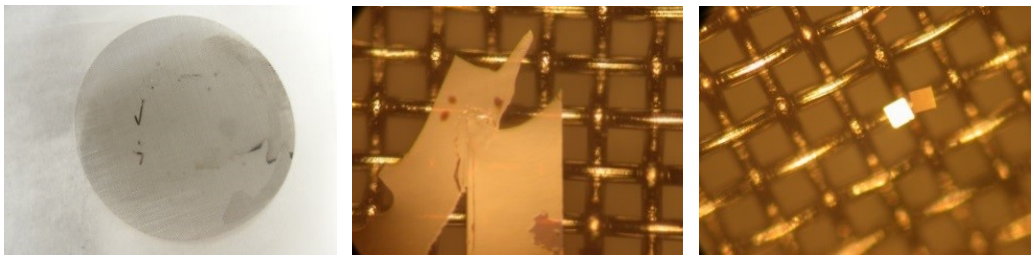

Figure 4-22 Wire mesh used for prefiltering devices in TCE (left). Debris collected on the wire mesh during filtration (middle). Devices stuck on the mesh filter (right).

3. Using tweezers, the membrane containing the devices was turned upside down to the hybridization buffer, 2X saline sodium phosphate EDTA (Ethylenediaminetetraacetic acid) from Fisher Scientific, without any air contact between the buffer and membrane filter in a large centrifuge tube (Figure 4-23 right).

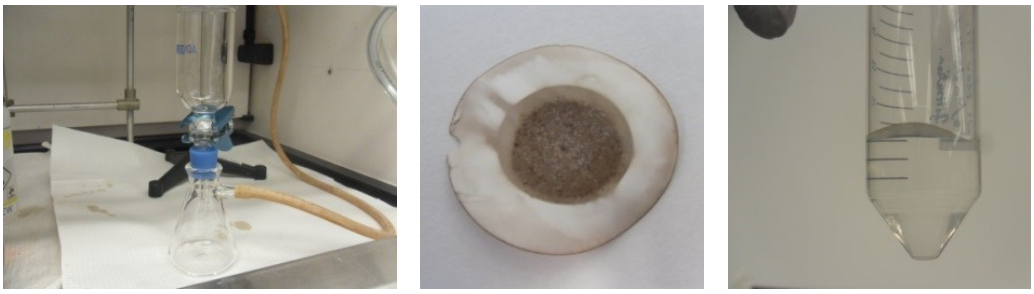

Figure 4-23 Microfiltration apparatus used to filter devices (left), membrane filter with devices after filtration (middle), and membrane filter upside down on hybridization buffer to detach devices in a centrifuge tube (right).

4. The centrifuge tube was sonicated to transfer the devices from the membrane filter into the hybridization buffer solution in the centrifuge tube (Figure 4-24).

Figure 4-24 Sonication to detach devices from membrane filter into the hybridization buffer (left). Optical microscopic view of membrane filter containing 25 μm devices (right).

4.3.2 Preparation of host substrate

We used bare Si substrate as well as gold coated and patterned substrates in our experiments.

4.3.2.1 Si based host substrate preparation

Steps involved in the preparation of Si based host substrate are described below.

1. To prepare the host substrate a regular (100) orientation Si wafer was diced to substrate/tiles of 1 × 1.5 cm along the (100) crystal planes using a Disco diamond saw in the nanoFAB facility at the University of Alberta. These substrates were piranha cleaned (3:1 mixture of 96% H_2SO_4 and 30% H_2O_2), to remove organic contaminants on the surface. Native oxide removal was performed by buffered oxide etching using a 10:1 mixture of 40% NH_4F and 49% HF for 90 s followed by a dump-rinse and drying under a stream of N_2. The substrate was further dehydrated and primed with HMDS.

2. An HPR-504 positive photoresist was applied with a Solitec spinner device to achieve a layer ~ 1.5 μm thick and the layered substrate was soft-baked in a vacuum hot plate for 90 s at 110 °C.

3. The photoresist was patterned by photolithography using a 1.9 s exposure of UV (365 nm) light followed by a 20 s developing step using a Shipley 354 developer (Figure 4-25). The chrome mask used for this was a negative mask, unlike the mask used for preparing the devices.

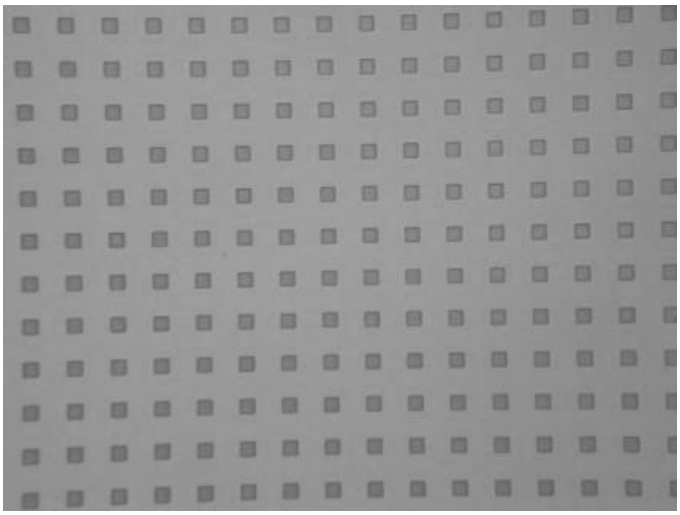

Figure 4-25 Host substrate patterned using HPR-504 positive photoresist with 100 μm squares.

4. A chemical vapor deposition of the SAM on the host substrate was performed. A more detailed explanation for this step is provided in section 4.3.3.

5. The photoresist was removed with a 10 minute sonication of the substrate in acetone.

4.3.2.2 Gold coated host substrate preparation

The diced 1 × 1.5 cm Si wafers were used to prepare the gold coated host substrate as described below.

1. Steps 1–3 of the Si based host substrate preparation (section 4.3.2.1) were performed.

2. Chromium metal was evaporated with an electron beam to achieve a ~ 7 nm thick layer on the host substrate.

3. Gold metal was evaporated with an electron beam to achieve ~ 50 nm thick gold layer on the host substrate (Figure 4-26).

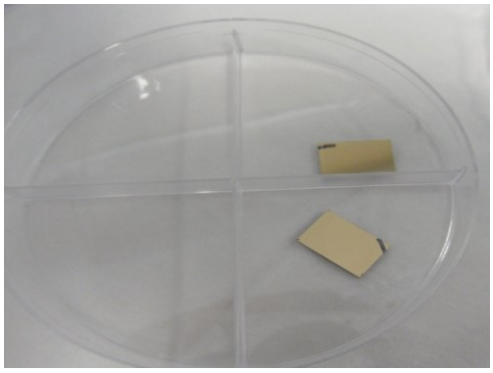

Figure 4-26 Gold coated Si substrate prepared by electron beam evaporation of the gold.

4. Liftoff process: the photoresist was dissolved by sonication in acetone, thereby making gold patterns on the Si substrate. For preliminary experiments, some of the substrates were made without using the photoresist patterns. Half-patterned substrates were also created.

5. A cold piranha solution cleaning was performed to remove organic contaminants.

The gold coated Si substrates prepared for our experiments are shown in Figure 4-27.

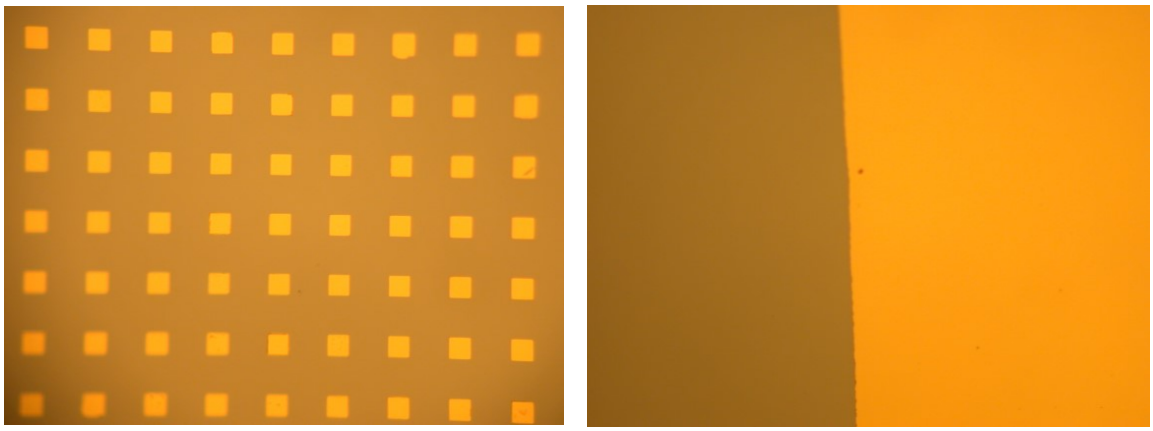

Figure 4-27 Gold coated Si substrates: Half patterned substrate (right) and 100 μm square patterned substrate (left).

We tried to deposit a gold coating on the devices immersed in the black wax, but the temperature conditions inside the evaporator caused the black wax to melt (Figure 4-28).

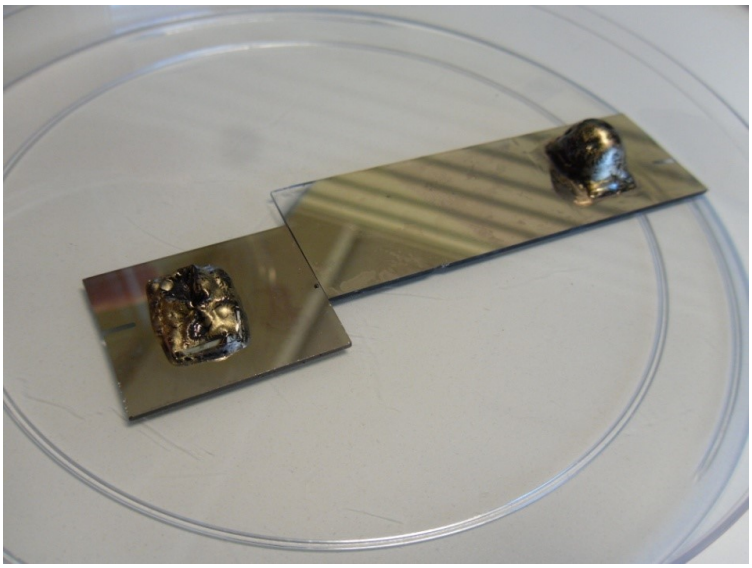

Figure 4-28 When gold was coated by evaporation onto the devices immersed in black wax, the black wax melted as shown.

4.3.3 Attachment of the DNA strands

DNA was attached to devices and to a host substrate with either a Si or a gold surface. Complementary oligonucleotides were obtained from Trilink Biotechnologies, San Diego. A fluorophore, AlexaFluor 546 (Em_{max} = 573 nm, Abs_{max} = 556 nm), was attached to the 5' end of one of the DNA strands to confirm successful hybridization. The oligonucleotide sequences are shown in Table 4-1 and Figure 3-22 shows the representation. The method used for attaching these DNA strands onto Si and Au surfaces is explained in section 4.3.3.1.

The efficiency of hybridization at the substrate surface can be enhanced by having spacer chains at the terminus of the DNA strand at the substrate attachment site. The spacer chain provides additional length to the DNA strands to remain as free chains to enhance hybridization conditions. I used spacer chain named Spacer9 which is a triethylene glycol chain 9 atoms long (6 carbon + 3 oxygen) and is incorporated into the oligonucleotides with a RNA Uracil (u) nucleotide at the 3' end of DNA supplied by Trilink Biotechnologies.

Table 4-1 Oligonucleotides used to assist the selective attachment of devices to a host substrate.

*Target DNA (**Type 1**)*: 5' CTC CAA ATT TGC TGA A (Spacer9) u (C3-SH) 3'
*Complementary DNA or probe DNA (**Type 2**)*: 5' TTC AGC AAA TTT GGA G (Spacer9) u (C3-SH) 3'
*Complementary DNA with Fluorophore (**Type 3**)*: 5' (Alexa546) (C6-NH) TTC AGC AAA TTT GGA G (Spacer9) u (C3-SH) 3'

4.3.3.1 Covalent attachment of DNA onto Si based host substrate and devices

DNA can be covalently attached to the Si substrate selectively [20-24], [50-53]. The method to attach DNA covalently to the host Si substrate was adopted from the work of Hamers and coworkers [79] (Figure 4-29). Silicon surfaces modified by this method are more selective and stable compared to Si surfaces modified by other methods. The steps are described in sections 4.3.3.1.1–4.3.3.1.3.

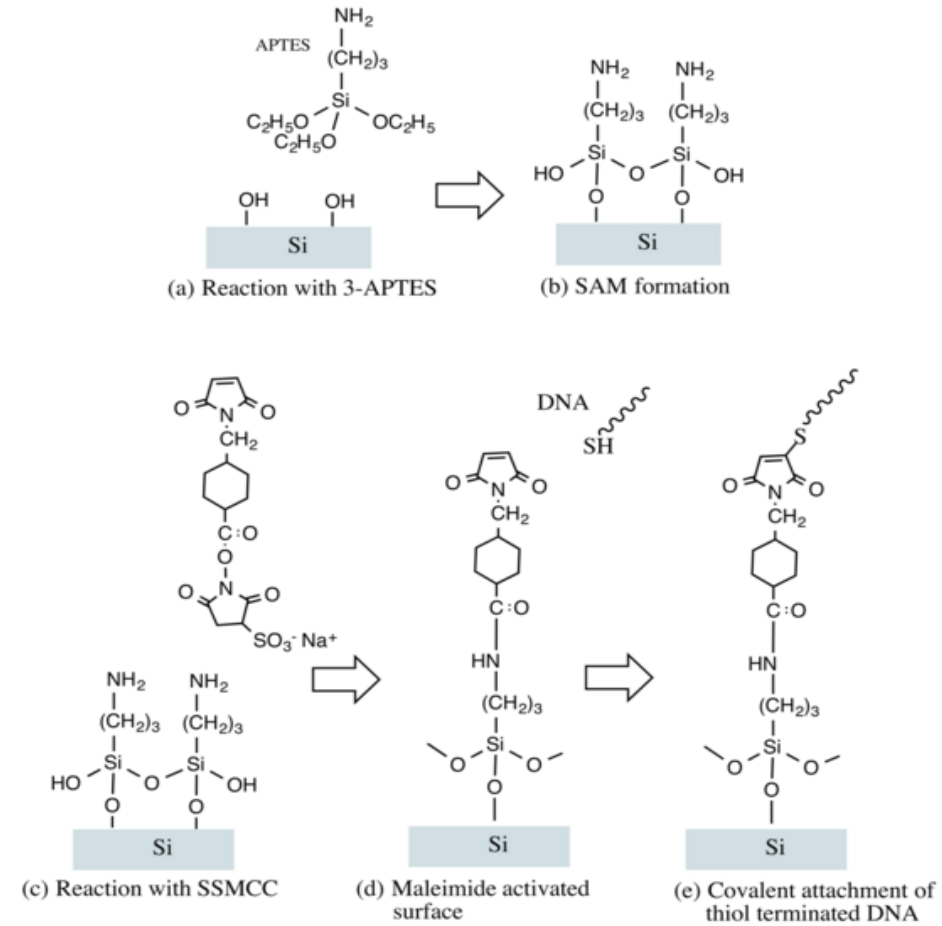

Figure 4-29 Schematic representations: (a) The covalent attachment of DNA onto the Si substrate. The Si surface is reacted with 3-APTES. (b) Formation of a self-assembled monolayer of 3-APTES on the Si surface. (c) The APTES-modified surface is then reacted with the bifunctional crosslinker sulfosuccinimidyl 4-[N-maleimidomethyl]cyclohexane-1-carboxylate (SSMCC). (d) The maleimide-activated surface is subsequently coupled with thiol-linked DNA. (e) Formation of DNA-attached Si substrate. Based on [63].

4.3.3.1.1 SAM formation

SAM formation was achieved by the reaction of the Si substrate having native oxide with 3-aminopropyl tri-ethoxy-silane (3-APTES) [162, 164] . This reaction can be performed in three ways (1) micro contact printing, (2) chemical vapor deposition, or (3) immersion of the substrate in 3-APTES. The chemical vapor deposition (CVD) method was chosen because it is known to form a smooth uniform monolayer on the Si substrate; the following six steps describe the procedure.

1. The Si substrate patterned with photoresist and the Si devices immersed in black wax were allowed to grow native oxide for 48 hours.

2. The CVD reaction was performed in a vacuum desiccator. Substrates were loaded into the desiccator (Figure 4-30) after cracking the vacuum.

Figure 4-30 Small vacuum desiccator used to perform CVD for SAM formation on the Si substrate.

3. A vial was flame-dried to avoid moisture, filled with 3-APTES solution, and stored in the desiccator.

4. The desiccator was purged (N_2) and pumped (vacuum) three times to create a clean and moisture free environment. Pressure (with 10–15 s intervals) was applied to the top of the desiccator to maintain the seal.

5. After ~ 24 hours, the desiccator was opened and the samples were taken out and sonicated in acetone for 10 min to remove the photoresist and the unbound APTES molecules.

6. The substrate was rinsed with HPLC-grade water.

4.3.3.1.2 Bifunctional crosslinker attachment to the substrate

The bi-functional cross linker molecule sulfosuccinimidyl 4-[N-maleimidomethyl]cyclohexane-1-carboxylate (SSMCC) (Fischer Scientific) was received in powder form and stored in a freezer. The procedure used to attach the SSMCC to the SAM coated substrate is described below:

1. Triethanolamine (TEA) buffer (in liquid form) and SSMCC (powder form) were brought to room temperature.

2. 2.6 mg of SSMCC in 1.2 mL of TEA buffer (pH 7.0) were placed in a centrifuge tube to obtain a 6 mM SSMCC solution.

3. 300 μL of the 6 mM SSMCC solution was placed in a new centrifuge tube and made up to 1 mL with TEA buffer to obtain 1 mL of 1.5 mM SSMCC in 150 mM TEA buffer at pH = 7.0.

4. 300 μL of the 1.5 mM SSMCC solution was pipetted on top of the Si substrate under ambient conditions and the reaction was allowed to continue for 15 min to make sure it was complete.

5. The substrate was washed with HPLC-grade water followed by drying under a stream of N_2 gas.

4.3.3.1.3 DNA hybridization tests

Lyophilized oligonucleotides (Trilink Biotechnologies Inc.) were attached to the SSMCC-linked substrate in the following steps.

1. The three oligonucleotides (Table 4.1) were aliquoted in TEA buffer at room temperature to create 1 μM oligonucleotide solutions.

2. Thiol modified oligos can oxidize to form oligo dimers by forming a disulfide linkage. Since we needed oligos with free –SH ends, the disulfide linkage was reduced using 60 mM (tris(2-carboxyethyl)phosphine) (TCEP) (18 mg TCEP in 1 mL H_2O). TCEP prevented disulfide linkage and was inert to further processing steps.

3. To test the successful attachment of the oligonucleotide onto the Si substrate I performed an experiment using the type 3 oligo with the AlexaFluor 546. 20 μL of the type 3 oligo solution and 5 μL of TCEP solution were pipetted onto the substrate after attaching the SSMCC (Figure 4-31).

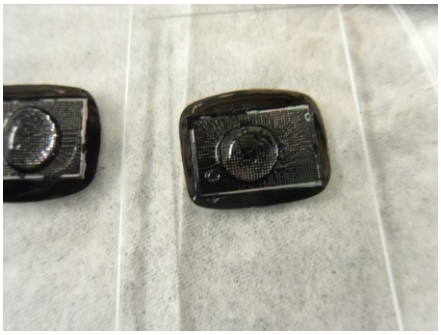

Figure 4-31 A drop of oligo solution to attach complementary DNA to the devices.

4. The substrate was covered with a cover slip which spread the 25 μL solution throughout the substrate (Figure 4-32). To avoid photo bleaching of the fluorophore; this part of the experiment was performed in a dark environment. The substrate was mounted on an SEM stub and stored in a box overnight.

Figure 4-32 A cover slip was used to spread the oligo solution over the substrate.

5. Some water was kept in the box to maintain humid conditions. If the solution dries out, the cover slip can become attached to the substrate. The box was covered with aluminum foil to maintain the dark condition and room temperature.

6. After sitting overnight, the cover slip was removed, washed with HPLC-grade water, and subjected to fluorescence microscopy.

To confirm the DNA attachment, I used the type 3 oligo with the Alexa Fluor 546. To test the hybridization of the two DNA strands, I attached the type 1 oligo to the host substrate and hybridized it with the fluorophore-attached type 3 oligo. Hybridization was performed in humid, dark conditions at room temperature overnight. The next day, the substrate was washed with hybridization buffer and dried with a stream of N_2.

For the self-assembly experiment, the same experimental steps were performed with the type 1 oligo attached to the host substrate and the complementary type 2 oligo attached to the devices.

4.3.3.2 DNA attachment to the gold coated host substrate

The visibility of the gold pattern compared to the bare silicon made it easier to test the steps involved in DNA attachment to the gold patterned substrate and to perform the later self-assembly experiments. To attach DNA to the gold substrate, the following steps were performed.

1. The Si substrate coated with gold was cleaned using a cold piranha solution to remove organic contaminants. It was found that hot piranha would peel the gold layer off the Si.
2. The gold-thiol reaction was performed by mixing 20 μL of the oligo solution with 5 μL of TCEP solution (to avoid oligo dimerization) and storing the mixture overnight at room temperature. The type 3 oligos with the Alexafluor 546 fluorophore were used to test the DNA attachment using Fluorescence microscopy and type 1 DNA was used for the hybridization test.
3. Cover slips were used to cover the substrate and spread the solution, and the sample was kept in a water filled petri dish to maintain the humidity. Steps 2 and 3 were performed in darkness with minimal light to avoid photo bleaching of the fluorophore. Darkness was further maintained for experiments with the fluorophore by covering the sample in the petri dish with an aluminum foil.
4. After keeping overnight, the substrate was cleaned with HPLC-grade water and subjected to characterization tests.

4.3.4 Self-assembly experiment

Si model device microtiles of 25 μm in size covalently attached with type 2 DNA strands freed from the black wax by membrane filtration were added to approximately 7.5 mL of hybridization buffer solution (2X saline sodium phosphate EDTA) in a centrifuge tube. The DNA hybridization buffer controls the stringency, facilitates spreading of the probe DNA strands and reduces the drying of the DNA strands during the hybridization reaction. A magnetic stir bar motion was used to circulate the devices so they will be suspended in solution and available for hybridization. The stirring was performed intermittently every 60 s using a timer, allowing enough time for settling of the devices between stir intervals. The patterned Si host substrate attached with complementary type 1 DNA strands was mounted on an SEM stub and kept in the centrifuge tube with the hybridization buffer with the Si model devices (Figure 4-33).

Figure 4-33: Centrifuge tube on a magnetic stirrer for the self-assembly experiment (left). The host substrate mounted on a SEM stub (right).

The centrifuge tube containing the hybridization reaction mixture was placed in a water bath to control the required hybridization temperature (Figure 4-34). When the Si model devices with type 2 DNA encounter the complementary type 1

DNA on host substrate, they hybridize and stick at that location. The self-assembly procedure was performed for 24 hours. Afterwards, the substrate was gently tilted to remove excess solution and air dried. Pictures of the host substrates were taken using optical microscopy and SEM imaging at nanoFAB, University of Alberta.

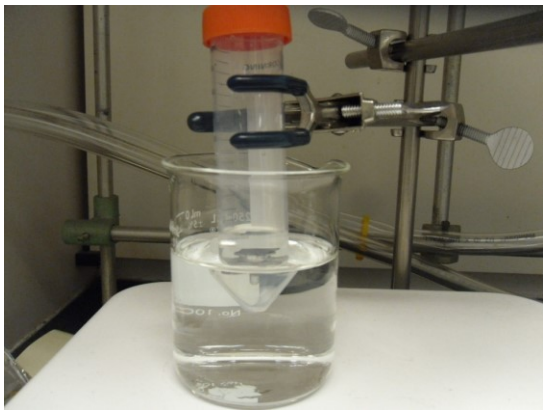

Figure 4-34: Self-assembly reaction in a water bath to maintain the hybridization temperature.

In another approach, the self-assembly experiment was performed by depositing the devices from the membrane filter directly on top of the host substrate in approximately 300 µL of hybridization buffer instead of transferring to centrifuge tube. This method was more effective in getting the Si model devices to encounter the patterned host substrate for self-assembly with no settling issues but misses the opportunity to circulate and keep the devices suspended. Again 24 hours were allowed for hybridization to occur. More details are given in section 4.4.

4.4 Results and Discussion

4.4.1 Si device fabrication and yield

Microtiles of 100 μm and 25 μm were fabricated from the SOI wafer. An optical microscopic image of the 25 μm devices embedded in black wax is shown in Figure 4-35.

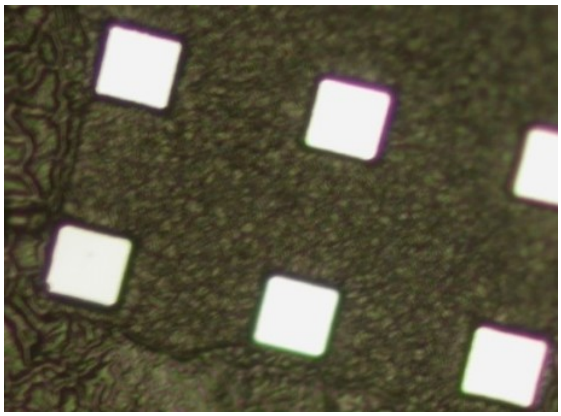

Figure 4-35 25 μm devices embedded in black wax spread over a glass slide.

After dissolving the black wax with trichloroethylene and during microfiltration many of the embedded devices were lost. In addition, some devices did not detach from the membrane filter due to the sticky black wax. Dissolving the black wax in a beaker and pipetting it out onto the microfiltration apparatus was found to be inefficient since many devices stuck to the beaker as well as to the pipette tip (Figure 4-36). Some devices were found attached to the microfiltration reservoir as well. A rough calculation estimated that only 37% of the devices were available on the membrane filter, ~ 8% stuck to the beaker, and rest were lost in the pipette tip, filtration reservoir, and the mesh of the prefilter.

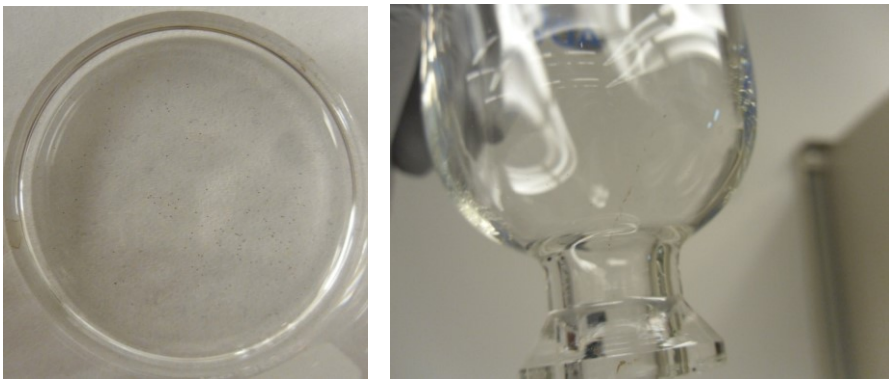

Figure 4-36 100 μm devices found stuck to the beaker (left) and the microfiltration reservoir (right).

To avoid this inefficiency, I decided to dissolve the black wax using TCE directly on top of the microfiltration apparatus so that no extra beaker was involved. Still, many devices adhered to the membrane filter after sonication due to the black wax. This was estimated by combining optical microscope pictures of the membrane filter using Autostitch software (Figure 4-37).

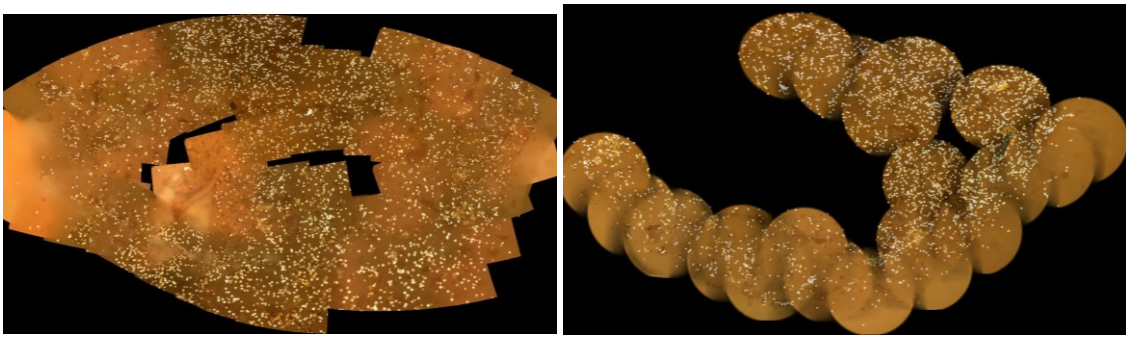

Figure 4-37 25 μm devices found on the membrane filter before sonication (left) and after sonication (right) to remove the devices.

4.4.2 Characterization results to confirm DNA attachment

4.4.2.1 SAM formation

To confirm the self-assembled monolayer formation on the Si substrate, I made use of contact angle goniometry, XPS, and ellipsometry. As a control sample, a Si substrate was cleaned using piranha solution to remove any organic contaminants.

On the control Si substrate sample, the contact angle between substrate and droplet was 15.4°, showing hydrophilic nature since the piranha solution mixture is a strong oxidizing agent which hydroxylates the Si surface by adding OH groups that attract water. The Si substrate surface after coating with the SAM had a contact angle of 60.4° (Figure 4-38) suggesting a dense, well-formed SAM. The more hydrophobic nature of the surface was due to the presence of an amine group which repels water.

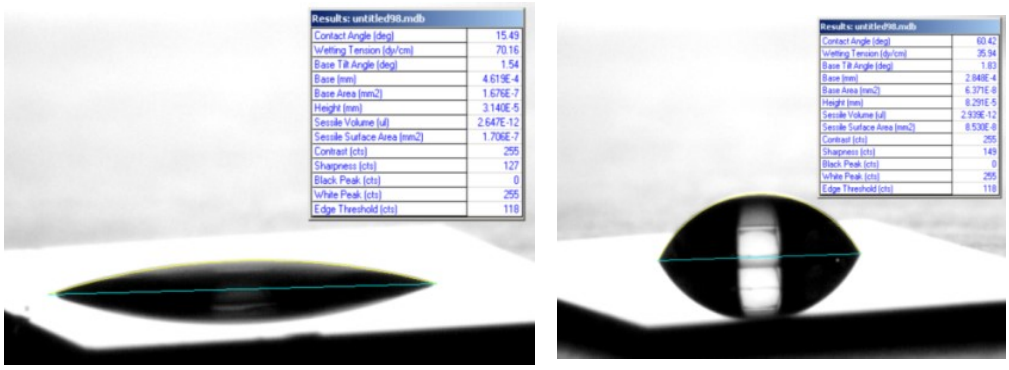

Figure 4-38 A bare Si substrate with native oxide (left) had a contact angle of 15.49°. The 3-APTES coated substrate had a contact angle of 60.42° (right).

Figure 4-39 shows the contact angles on a substrate half patterned with SAM, and we can clearly see the hydrophobic and hydrophilic regions of the same substrate.

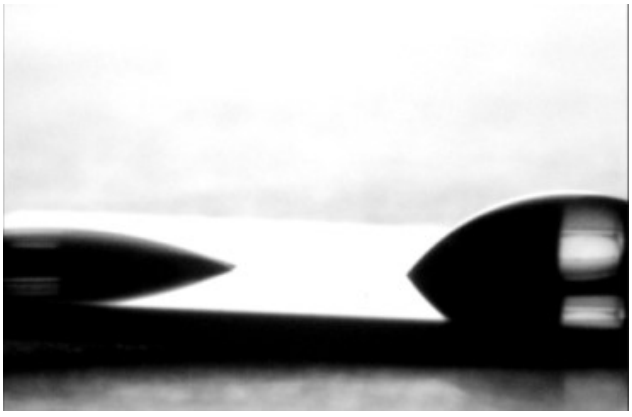

Figure 4-39 This Si substrate is half patterned with a self-assembled monolayer. The left half without SAM has a lower contact angle than the right half with the SAM.

XPS results also suggested the presence of a self-assembled monolayer on the Si substrate (Figure 4-40).

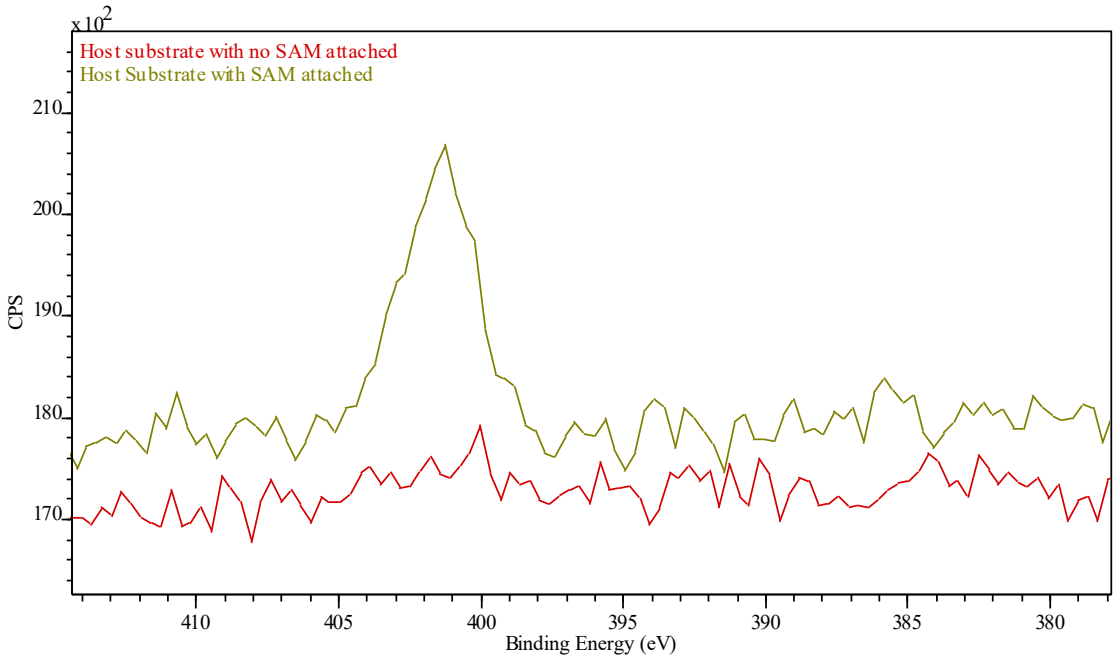

Figure 4-40 An XPS peak at ~ 400 eV indicates the presence of nitrogen, which confirms the presence of an amine group on the substrate surface (green). There is no N_2 peak in the control sample (red).

The nitrogen peak at ~ 400 eV confirmed the presence of the amine group of the SAM. The SAM coated substrate was found to have a 1.76% atomic concentration of nitrogen as opposed to 0.01% for the bare Si substrate. As expected, samples for which the SAM was formed using the immersion method had a higher atomic concentration of 2.02% compared to samples treated with the CVD method which had an atomic concentration of 1.76%.

An ellipsometry test using the VASE ellipsometer at the nanoFAB facility at the University of Alberta found a 2.9 nm thick layer on top of the Si substrate which strengthens our belief in the formation of a SAM on the substrate.

Figure 4-41 shows the ToF-SIMS result obtained for a control sample that was patterned with 25 μm squares using a photoresist. We can see the presence of silicon in the square region only because the rest of the area is covered with photoresist. Carbon, nitrogen, and oxygen atoms are not observed in the square region.

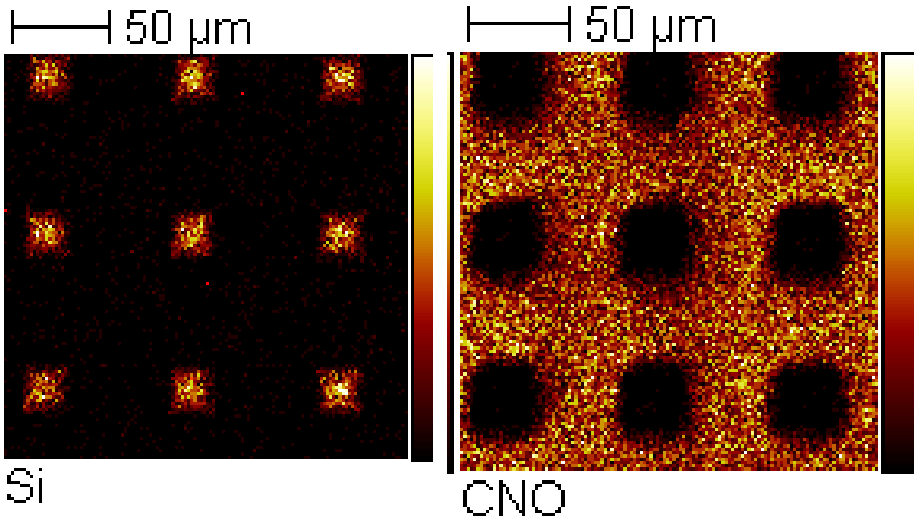

Figure 4-41 ToF-SIMS of a control sample patterned with 25 μm squares with photoresist and no SAM attachment (left). Si rich region (right) with C, N, and O.

Figure 4-42 shows the result obtained for the sample in which SAM was attached to the patterned region. The presence of C, N, and O are more clearly seen in the square region, confirming the presence of SAM.

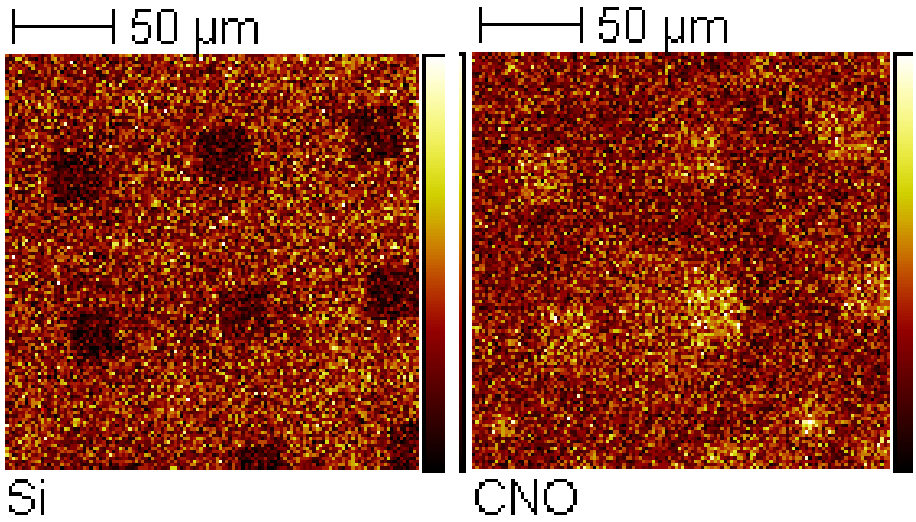

Figure 4-42 ToF-SIMS of a sample patterned with 25 µm squares and SAM attached (left). Si rich region (right) with C, N, and O.

4.4.2.2 SSMCC Attachment

Similar to the attachment of the SAM, I verified SSMCC attachment to the amine terminated SAM using contact angle measurements, XPS, and ellipsometry. With SSMCC attachment, the surface of the Si substrate became more hydrophobic and presented a contact angle of 72° (Figure 4-43).

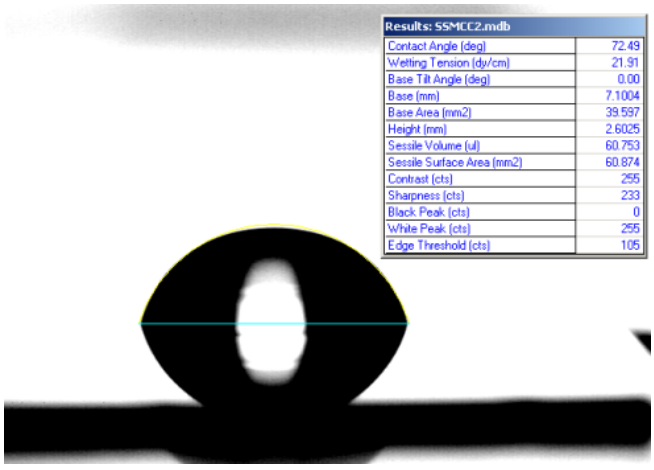

Figure 4-43 Contact angle of 72° for SSMCC-attached Si substrate.

In the XPS spectra, the presence of C=O can be confirmed by looking for a peak at ~ 290 eV. Figure 4-44 shows the XPS results obtained for substrate with and without SSMCC attached.

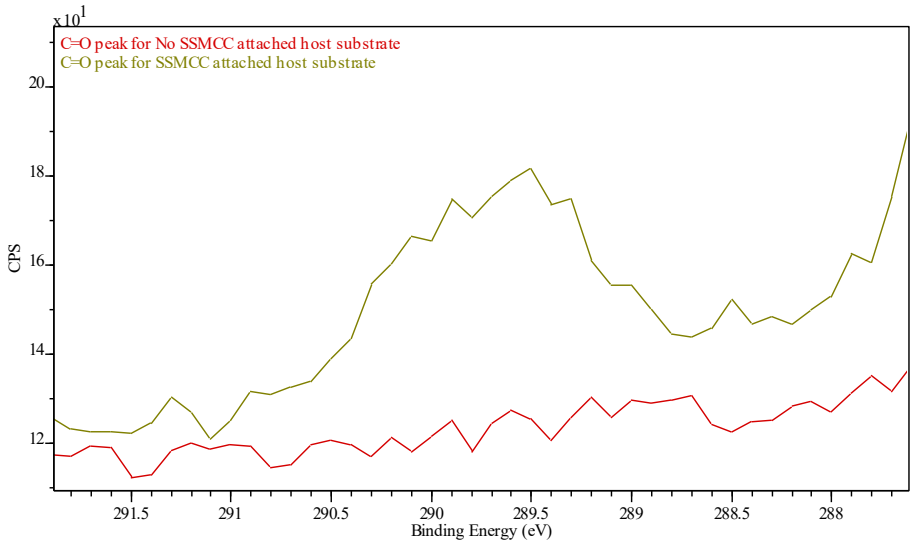

Figure 4-44 XPS spectra of Si substrate after SSMCC attachment (green) and the control sample without SSMCC attachment (red).

Ellipsometry indicated a layer thickness of 2.9 nm before and 4.1 nm after SAM formation. The increase in thickness indicates a successful attachment of the SSMCC bifunctional cross linker.

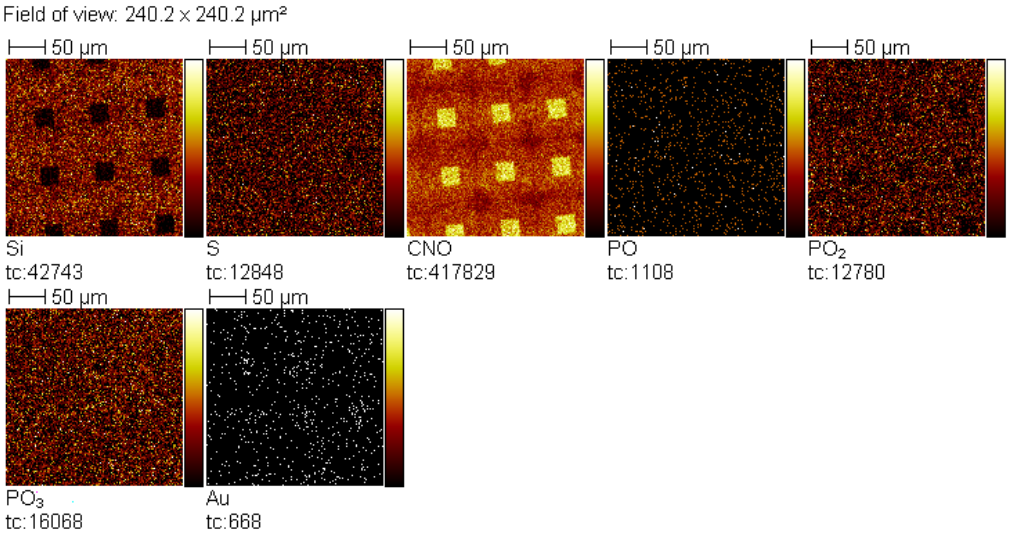

Figure 4-45 ToF-SIMS results obtained for a substrate after SSMCC attachment.

The ToF-SIMS results obtained for the substrate after SSMCC attachment are shown in Figure 4-45. There is no Si in the 25 μm patterned square region. The more intense signals in the square region for C, N, and O atoms indicate the presence of the C=O rich SSMCC. The absence of PO, PO_2, PO_3, and Au indicate the absence of oligonucleotide and gold coating in this sample.

4.4.2.3 DNA attachment

To confirm attachment of the DNA to the Si substrate through the bifunctional cross linker, fluorescence microscopy and ToF-SIMS were applied. To perform this test the host substrate was patterned with 100 μM squares to enable SAM formation and to encourage DNA attachments in these regions. The attachment of the type 3 oligonucleotide with the AlexaFluor 546 fluorophore is shown in Figure 4-46. The fluorescence microscopy image (Figure 4-46, right) obtained for the Si substrate patterned with type 3 DNA confirms the successful selective covalent attachment of the DNA to the patterned Si substrate. The Olympus IX81 inverted fluorescence microscope at NINT was used to observe the samples.

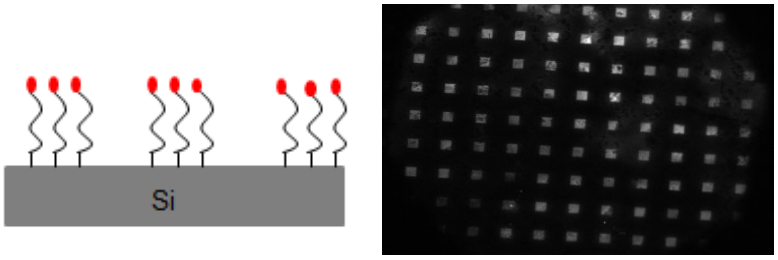

Figure 4-46 (Left) Schematic representation of the Si substrate patterned with SAM and type 3 DNA attached with fluorophore. (Right) fluorescence microscopy image of the Si substrate with the type 3 oligonucleotide attached.

ToF-SIMS confirmed the selective attachment of the DNA strands to the Si substrate (Figure 4-47). PO_2, and PO_3 groups indicate the presence of

oligonucleotides. For a 25 µm patterned Si substrate we can see, no Si surface square regions and the obvious presence of C, N, and O indicates the presence of SAM, SSMCC, and DNA.

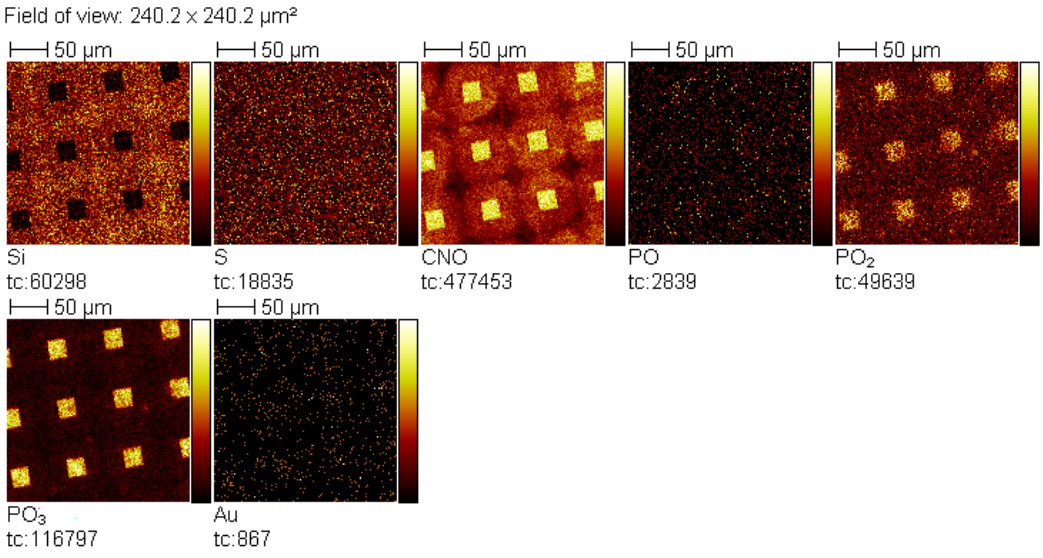

Figure 4-47: ToF-SIMS spectra of a square patterned region of Si substrate after DNA attachment. The presence of PO_2 and PO_3 groups present in the oligonucleotides indicates the successful attachment of DNA to the substrate.

The successful attachment of the thiol terminated type 3 DNA to the gold patterned as 100 µm squares on the Si host substrate is suggested by the fluorescence intensity in Figure 4-48.

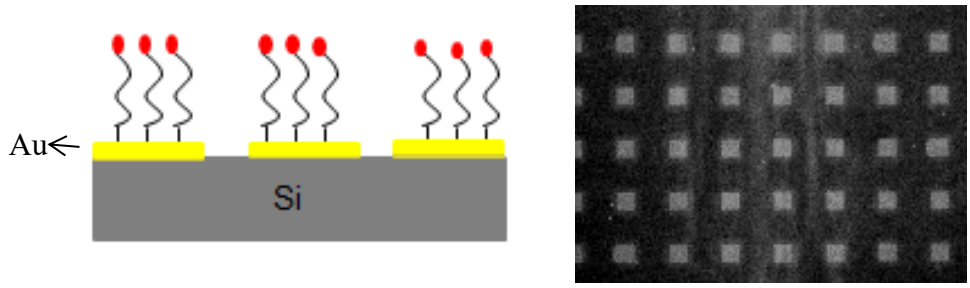

Figure 4-48: Schematic representation of the gold patterned substrate with type 3 DNA attached with fluorophore (left). Fluorescence microscopy image of the gold patterned substrate with thiol terminated type 3 oligonucleotide attachment (right).

TOF-SIMS spectra also confirmed the selective attachment of DNA to the gold rich square region of the substrate (Figure 4-49).

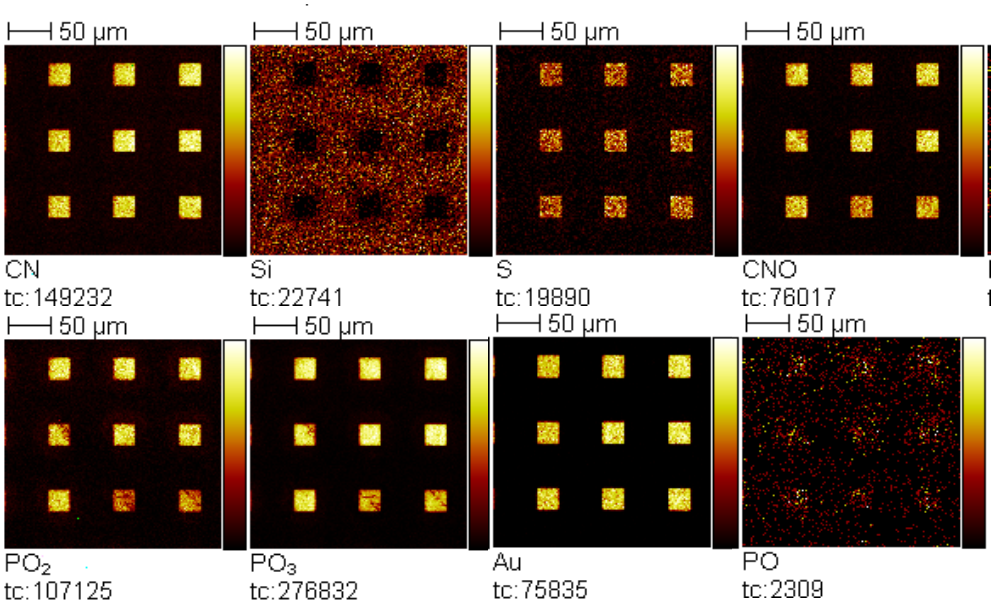

Figure 4-49: ToF-SIMS spectra of DNA attached to the square gold patterned region of a Si substrate. The presence of PO_2 and PO_3 groups present in oligonucleotides indicates the presence of DNA in the square regions.

4.4.3 DNA hybridization verification

Hybridization of the DNA strands (type 1) on the host substrate to the complementary DNA (type 2) was verified using fluorescence microscopy. Type 1 target DNA was attached to the host substrate and hybridization with complementary type 3 DNA with the fluorophore was performed for 24 hours in dark, humid conditions. This experiment was performed with the Si based host substrate (Figure 4-50) and also with the gold patterned substrate (Figure 4-51) and positive results were obtained in both cases.

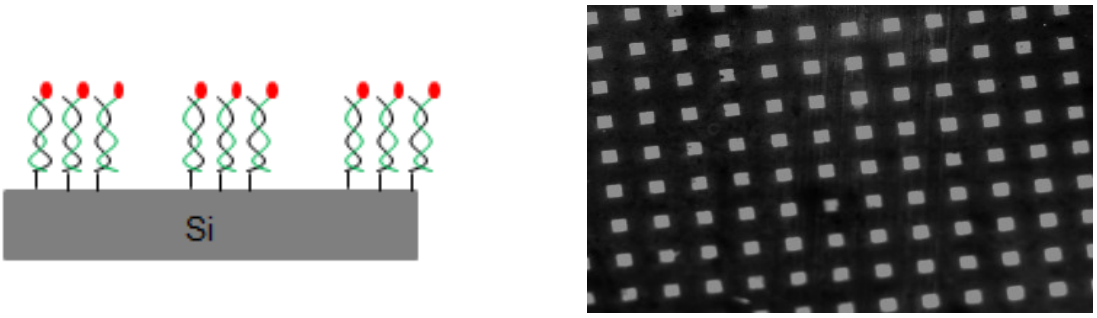

Figure 4-50: Schematic representation (left) and fluorescence microscopy image (right) of the Si substrate patterned with type 1 target DNA and hybridized with complementary type 3 DNA with the fluorophore.

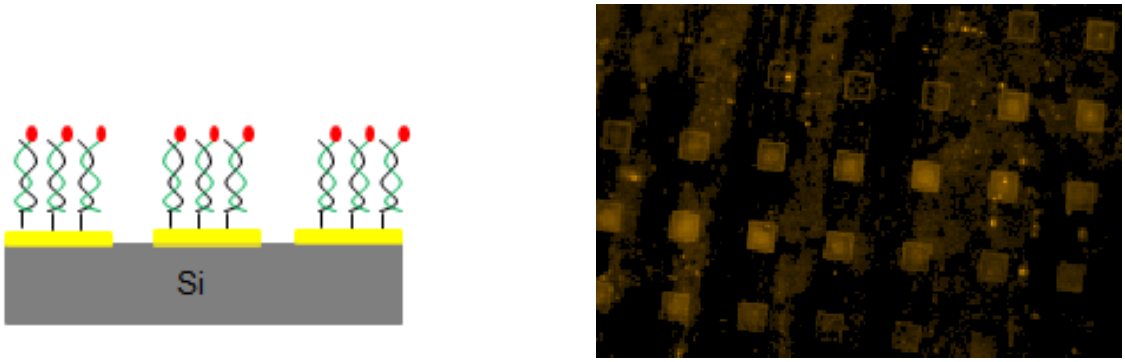

Figure 4-51: Schematic representation (left) and fluorescence microscopy image (right) of the gold patterned substrate with type 3 DNA with the fluorophore attached.

4.4.4 Effect of trichloroethylene (TCE) on DNA attachment

Trichloroethylene was used to dissolve the black wax and free the devices for self-assembly; therefore, it was necessary to test the effect of trichloroethylene and black wax on the DNA attachment to the Si surface and to the hybridization experiment. A sample with DNA (type 1) attached to a patterned Si substrate was dipped it in a mixture of black wax and trichloroethylene. After that the sample was dipped in trichloroethylene alone and hybridization was performed using the complementary type 3 DNA with the fluorophore. The product of the reaction was subjected to fluorescence microscopy (Figure 4-52).

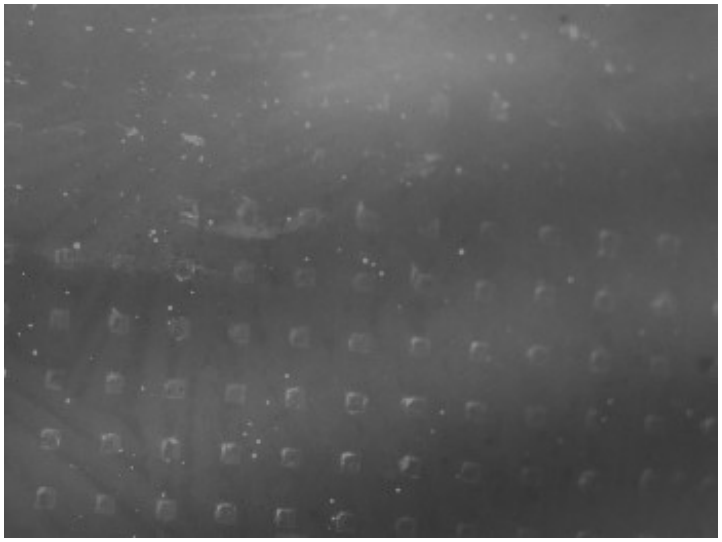

Figure 4-52: Fluorescence microscopy image of type-1 DNA patterned on the Si substrate after treatment with black wax and trichloroethylene and hybridization with complementary type-3 DNA with the fluorophore.

The experiment above was also performed with Au-coated substrate and the result is shown in Figure 4-53. Fluorescence microscopy results indicated that the DNA attachment survived the treatment with trichloroethylene.

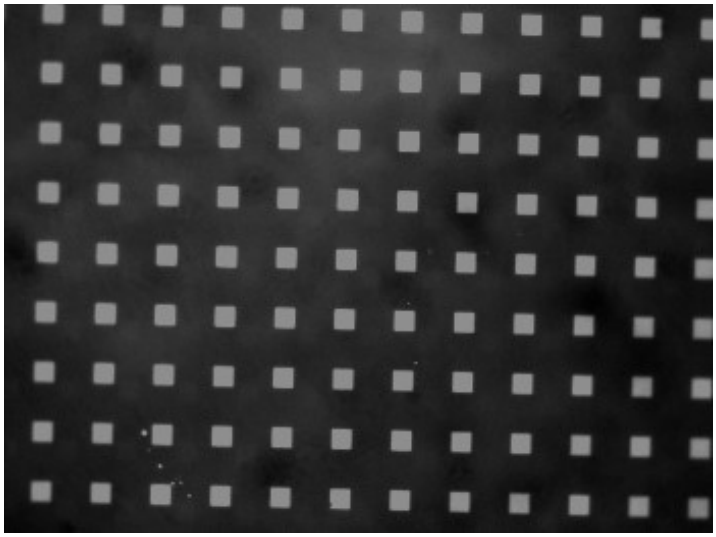

Figure 4-53: Fluorescence microscopy image of DNA patterned on a gold patterned host substrate after treatment with black wax and trichloroethylene and hybridization with complementary type-3 DNA with the fluorophore.

4.4.5 Self-assembly results

4.4.5.1 Self-assembly of Si model devices

Using the method described in section 4.3.4 DNA-assisted self-assembly experiment was performed at room temperature using Si substrates patterned with type 1 target DNA and 25 μm devices with type 2 complementary DNA by allowing 24 hours for hybridization to occur. The sample was gently air dried and analyzed under the optical microscope. The first thing noticed was the presence of salt from the hybridization buffer (Figure 4-54, left) which made it hard to visualize the model devices. Hence, an additional step was added to gently wash the sample with HPLC-grade water to dissolve the salt (Figure 4-54, right), but then we could hardly find any model devices attached to the substrate. This might be from the washing or due to insufficient contact between the substrate and the devices.

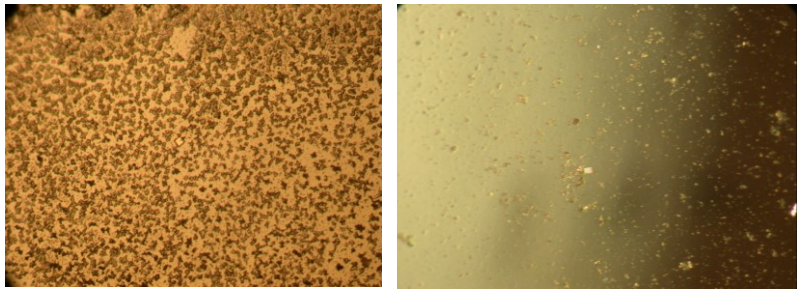

Figure 4-54: Host substrate with salt from the hybridization reaction after performing the self-assembly experiment (left). Host substrate after salt was dissolved with HPLC-grade water (right).

Next, I tried a second approach of delivering devices directly on top of the substrate from the membrane filter (Figure 4-55). This time the presence of some black wax (Figure 4-55, left) was noticed on the host substrate that might had been incompletely removed from the devices in TCE washing and filtration steps. To clear this black wax, another gentle wash was performed with TCE solution, which

further cleared the substrate (Figure 4-55, middle). This time I was able to find more devices holding onto the substrate but no pattern was found as expected. One thing noticed before and after gentle TCE wash was the devices present on the substrate were unmoved from their original locations. We cannot confirm that these devices are holding due to the DNA hybridization, it might be due to the sticky black wax still remaining.

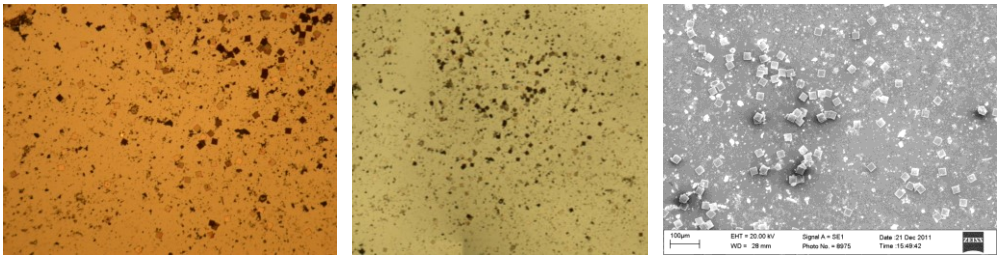

Figure 4-55: The host substrate after the self-assembly experiment showing the presence of black wax (left) and after 1 hour of dip wash in TCE solution (middle). An SEM image of the host substrate assembled with 25 μm devices (right).

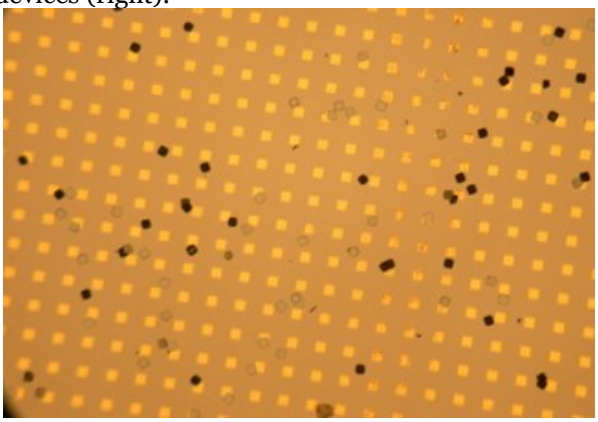

Figure 4-56: 25 μm devices self-assembled on an Au patterned host substrate.

Figure 4-56 shows the result of a device–substrate attachment experiment, conducted with 25 μm Si nanochips on a gold patterned host substrate. The Au areas in the patterned substrate contain the complementary type 1 DNA strands. The gold on the substrate allows us to better visualize the target DNA rich region as compared to the previously used Si host substrate. After the self-assembly experiment, the substrate is washed with HPLC water and TCE to remove excess

salt and black wax, respectively. In this case, I found devices holding onto the substrate but these devices were not properly aligned to the expected patterned regions. Again, we cannot confirm that these devices are holding due to the DNA hybridization, it might be still due to the remaining sticky black wax. It is clear that significant non-specific binding is occurring, and the intended DNA-mediated attachment has not been convincingly achieved. It is unclear why some microtiles are dark and others light. This could be due to orientation or to wax or other contaminant adhering to the tile.

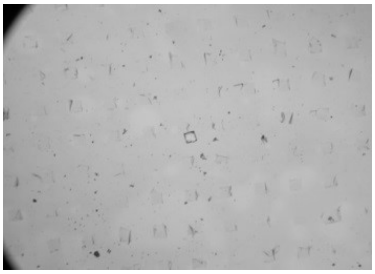

Figure 4-57: 25 μm devices self-assembled on a patterned silicon host substrate.

Figure 4-57 shows the result for 25 μm tiles under the same conditions as above but using a silicon substrate. Very little attachment of devices was observed, and wax contamination is evident in this case. The presence of black wax obviously contributes to the steric hindrance for the DNA strand to bind.

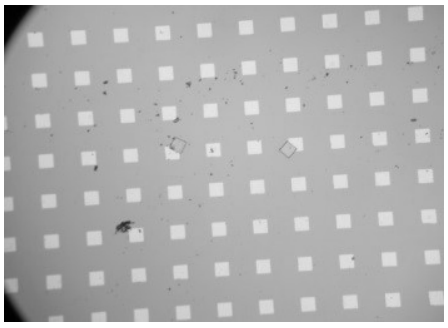

Figure 4-58: Assembly of 100 μm devices (right) on a Au patterned host substrate.

We also attempted the procedure with larger 100 μm devices. Some selectivity of attachment may have been observed on patterned gold pads (Figure 4-58), but so few tiles attached to the substrate that it is hard to be definitive. The role of device size on assembly success is explored further in the discussions below in section 4.4.5.2. Various wash and rinse procedures were explored to try to further reduce the visible contamination, but these were not yet successful at improving device attachment.

4.4.5.2 Possible causes and improvements

After performing the self-assembly experiment using 25 μm and 100 μm sized Si microtiles, it is clear that there are unresolved challenges to achieve selective attachment. From the characterization experiments it is evident that I was successful in achieving the attachment of DNA and self-assembly of DNA strands happened selectively at the molecular level. But I could not achieve the same selective attachment for the 25 μm and 100 μm sized Si microtiles. Some possible reasons for this unpersuasive result are described below.

1. **Steric effects**: One of the major challenges is to get enough DNA hybridization for the selective attachment of the Si devices. Getting far fewer hybridizations than expected might be the one of the issues. The reasons for reduced hybridization could be either steric effects or competitive binding. Dense packing of the DNA strands on the substrate or the DNA conformation might not be in upright position which would inhibit hybridization. Competitive binding is perhaps happening by preferentially binding up the surface by substances like the black wax. Using an extra spacer chain to the DNA strand tethered to the host

substrate might improve the chances of DNA hybridization by allowing the free chain of the probe DNA strands to be more available.

2. **Device release forces**: Another major challenge came across while performing the self-assembly experiment is the requirement of stirring and of wash cycles to remove excess salt and black wax using HPLC water and TCE respectively. These create hydrodynamic or other forces that could detach the devices. Forces involved in assembly include covalent, biological/molecular, electrostatic, gravitational, and viscous drag. The forces contributing to the attachment of the devices on the substrate must be greater than the forces that separate the particles from the substrate during subsequent processing steps. I performed order of magnitude calculations to understand how these forces depend on the size and shape of the devices, which is discussed in detail in section 4.4.5.3, below.

3. **Size of the devices:** The initial self-assembly experiment was performed using the 25 μm sized devices. Maybe it is too bulky for the DNA to handle this, especially given other competing forces involved in various steps such as the sample wash. To test this, I performed the self-assembly using 200 nm sized gold nano-particles. This experiment and the results are discussed in section 4.4.6 below.

4. **Impingement of the devices:** An additional challenge that came across while performing self-assembly is to allow the devices to circulate as well as to settle down to get the selective attachment. Initially, I used the magnetic stirrer to circulate the devices and used a timer (operate every 60 s interval) to turn on or off the stirrer for the devices to settle down to get the impingement onto the

substrate for hybridization to happen. But the forces and turbulence generated during magnetic stirring might contributes to the device release force rather than attachment mentioned above (1). I tried to solve this issue by getting the devices directly on top of the substrate, but in this case the agitation or the circulation of the devices were missing. Applying positive electric potential at the substrate to attract the negatively charged DNAs in the devices is possible future research focus [174, 175].

5. **Sticky black wax**: In the procedure, I use black wax to temporarily hold the devices before their release in TCE. It is evident that the black wax is present in the solution during the self-assembly (Figure 4-55). This will make the devices sticky to the substrate in unintended areas. An additional TCE wash steps were required to dissolve away the black wax after self-assembly. I confirmed the TCE wash does not affect the DNA hybridization in section 4.4.4. An alternative method of detaching the devices without using black wax is a future recommendation. Another approach is detailed in section 4.4.7 below.

6. **Oligonucleotide concentration**: An oligonucleotide concentration of 0.02 μM was used for each set of substrates and devices. But considering that factors like 30% hybridization efficiency [22] , and other dilution effects might reduce the availability of the DNA strands for the final self-assembly experiment.

7. **Length and sequence of DNA:** I performed all the experiments using the 16-mer (5'-TTCAGCAAATTTGGAG-3'). A longer sequence may be an option to be tested since it would enhance the availability of the DNA strand for hybridization [176], and this was the purpose of the spacer9 used in the experiment. In chapter 3, the binding energy of 9-mer<10-mer<pal10-mer<20-mer was found, so longer

sequenced DNA strands bind more strongly. It may be an option to try even longer spacers. Also, we saw more GC content in the sequence improve the binding energy due to extra hydrogen bonding (Figure 3-25). So choosing a DNA sequence which is palindromic or having more GC content is recommended.

8. **Salt concentration:** I used a hybridization buffer with a salt concentration of 0.3 M; from Chapter 3 we saw the hybridization binding improves with salt concentration. In Figure 4-54 the presence of lots of salt was found in the sample requiring a wash step to remove it. Lowering the salt concentration further by diluting the hybridization buffer is also a possible option.

9. **Settling rate:** Another issue might be slow particle settling rates. As the size of the devices decreases, there will be less gravitational force assisting the devices to settle. The gravitational force calculations were performed in section 4.4.5.3 below.

4.4.5.3 Device binding force calculation

The binding force of the single strand and its complementary strand is the force considered for the attachment of the device to the substrate. The gravitational and shear stress forces are contributing to the release of the devices during the wash step as well as during the circulation of devices using the magnetic stirrer. To better understand the scaling relationships, the force calculations were performed for device with a size range of 1 nm to 1 cm with the shape of tiles and spheres as well. Shear stress calculations were performed for the tiles and drag forces were accounted for the spherical device release.

Based on work of Desilva *et al.*, the binding force for a 12-mer DNA strand is 42

pN [177], so for 16-mer DNA strand has an approximate binding force of 50 pN. The density of DNA strands that get attached to Si substrate is in the order of ~10^{12} molecules/cm^2 [178].

Considering 30% hybridization efficiency [22], total attachment force F_{attach} can be calculated using Equation 4.1 given by:

$$F_{attach} = 0.3F_{bf}\rho_d x^2 \tag{4.1}$$

where x is the device size.

The wash velocity, v_w, was assumed to be 1 cm/s. The higher the wash velocity, the higher will be the chance of releasing the device or preventing attachment.

Device release force calculation for tiles

The two contributing factors to the release of the device from its attached state are body forces such as the gravitational force (F_g) and surface forces such as the shear stress force (F_s). For a Si micro tile with 0.08x thickness and density (ρ_d) of 2.33 g/cm3, the force of gravity can be calculated as:

$$F_{g,tiles} = 0.08\rho_d g x^3 \tag{4.2}$$

where g is the acceleration due to gravity.

The shear force is calculated using the equation:

$$F_s = \tau\, x^2 \tag{4.3}$$

where τ is the shear stress given by:

$$\tau = \mu \frac{du}{dy} \tag{4.4}$$

and μ is the dynamic viscosity of water. The average slope $\Delta u/\Delta y$ across the boundary layer was use to estimate du/dy in the vicinity of the surface. Assuming laminar flow across the tiles, the boundary layer thickness can be calculated using

Blasius solution [179, 180] given by:

$$\delta \approx 4.91x/\sqrt{Re_x} \tag{4.5}$$

where Re is the Reynolds number [181].

The total device release force $F_{release}$ for tiles was calculated using equations 4.2 and 4.3:

$$F_{release,tiles} = F_{g,tiles} + F_s \tag{4.6}$$

Device release force calculation for sphere shaped devices

In the case of devices shaped as spheres, the contributing factors for the release from the attached state are gravitational force (F_g) and drag force (F_d). The force of gravity can be calculated as:

$$F_{g,spheres} = \frac{\pi}{6} x^3 \rho_d g. \tag{4.7}$$

Assuming laminar flow, the drag force on the spherical device can be calculated using Stokes law [182] given by:

$$F_d = 6\pi\mu R\vartheta \tag{4.8}$$

where R is the equivalent sphere diameter of the device, and ϑ is the device velocity which is assumed to be 0.1 m/s.

Using equation 4.7 and 4.8 the total device release force for spherical devices was calculated:

$$F_{release,sphere} = F_{g,sphere} + F_d. \tag{4.9}$$

In Table 4-2 we can see the order magnitude of forces for holding the devices in attached state and the estimated release forces due to the gravity and the drag as well as shear force experienced on the device during the wash step. This indicates

that these release forces are contributing to the chance of devices getting detached from the assembled state. From the results obtained, I found that a wash is needed to remove the excess salt and black wax to clear the substrate. From these calculations, we could see that the DNA hybridization attachment force can handle the assembly of 25 μm sized devices.

Table 4-2 Forces calculated for various sizes of device

Device Size (x)	Attachment Force (N)	Release Force (N)	
	F_{attach}	$F_{release,tiles}$	$F_{release,spheres}$
1 nm	1.5E-13	6.40E-18	1.9E-13
10 nm	1.5E-11	2.00E-16	1.9E-12
50 nm	3.7E-10	2.30E-15	9.4E-12
100 nm	1.5E-09	6.50E-15	1.9E-11
1 μm	1.5E-07	2.30E-13	1.9E-10
10 μm	1.5E-05	2.90E-11	1.9E-09
25 μm	9.3E-05	5.40E-11	4.9E-09
50 μm	3.7E-04	3.00E-10	1.1E-08
100 μm	1.5E-03	2.00E-09	3.1E-08
200 μm	6.0E-03	1.50E-08	1.3E-07
1000 μm	1.5E-01	1.80E-06	1.2E-05
1 cm	1.5E+01	1.80E-03	1.2E-02

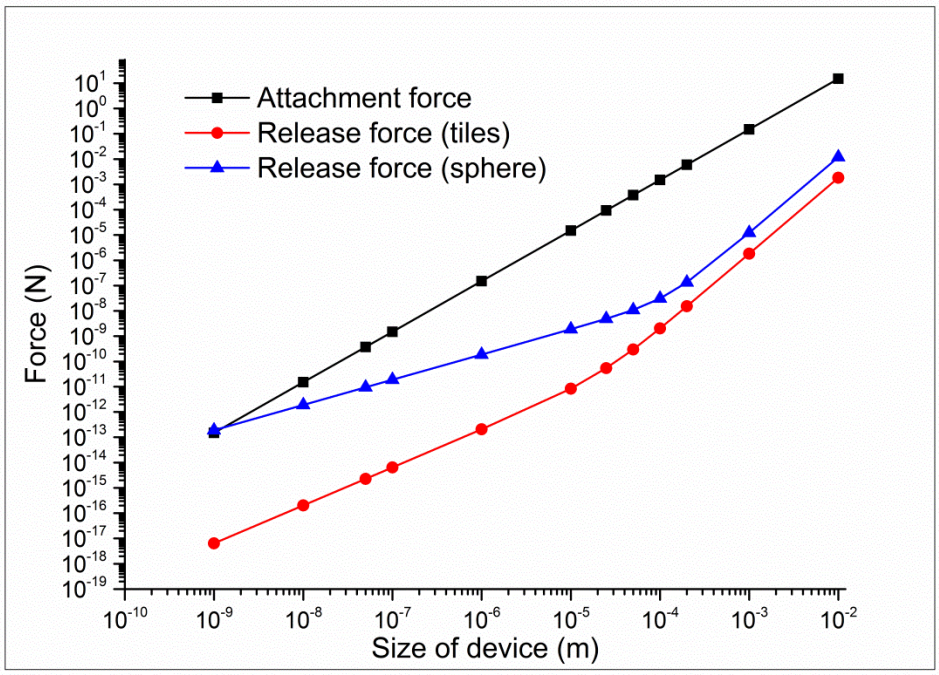

Figure 4-59: Forces assisting the attachment and the release of the devices onto the substrate are plotted against the size of the device.

To better understand the scaling relationships, the calculation is extended to forces acting on different sized devices ranging from 1 nm to 1 cm (Table 4-2). The log plot (Figure 4-59) clearly shows that the ratio of attachment to detachment increases until 100 μm and starts to diminish thereafter. In addition, it is clear that the shear stress on the tiles is predominant in releasing the device from the attached state. The gravitational force plays its role in releasing the device when the size is 100 μm and above. Devices in the size range of 10 nm to 100 μm should not be affected by the gravitational force, and this should be the optimum device size range recommended for DNA-assisted self-assembly.

The fluorescence microscopy and ToF-SIMS results confirmed that the DNA self-assembly is happening at the molecular level. While performing the same using the 25 μm devices, the results are not convincing to assure the self-assembly of the devices. Hence, it is interesting to see the behavior of the devices close to 1

μm and below in size. I performed the self-assembly experiment using 200 nm sized gold nanoparticles which is discussed in section 4.4.6 below.

Based on these calculations, we can observe that the DNA-assisted self-assembly technique is dependent on the shape of the devices as well as based on the release force calculations performed for devices with the shape of both tiles and spheres. For devices with size below 100 μm, the more spherical the shape of the device the greater is the chance of getting released. Since the surface contact area for a sphere is even less as compared to a tile, this will be another contributing factor for the release of the spherical device. But when we consider the impingement of the DNA strand attached device to the substrate, the spherical device has more advantages due to no orientation issues and potentially fewer steric effects.

4.4.6 Self-assembly of gold nanoparticles

To test DNA-assisted self-assembly using a different size range of devices, I performed the same experiments using 50 nm and 200 nm sized gold nanoparticles (0.01% Au, 20 mL) from Nanocs Inc with approximately 10^{10} and 10^{9} particles/mL concentration, respectively. Figure 4-60 is an outline of the procedure used to conduct this experiment.

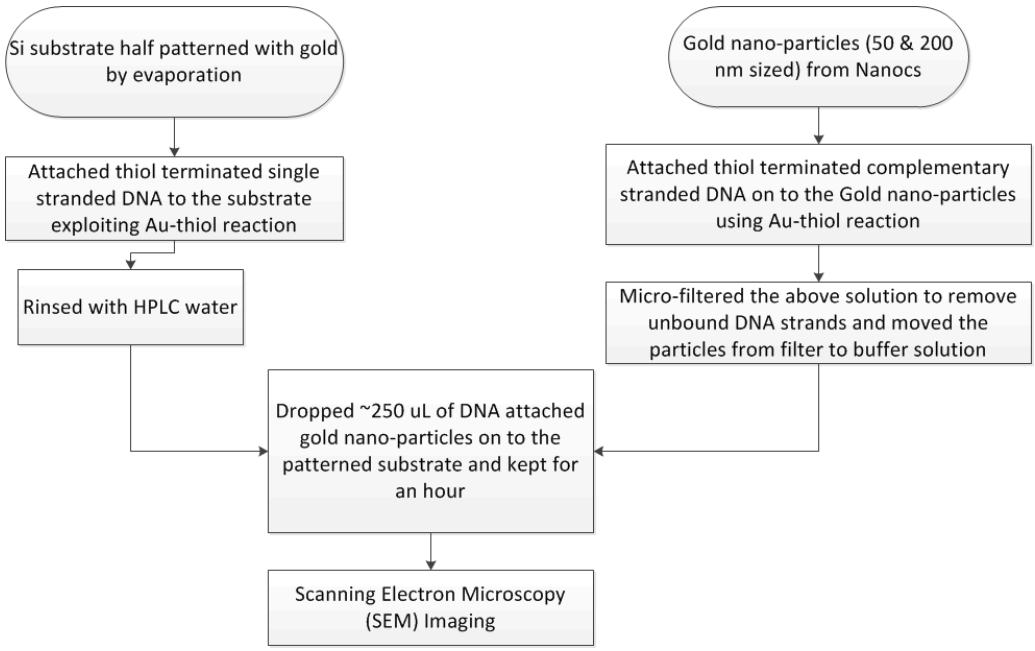

Figure 4-60: Flow chart for the procedure used to perform DNA-assisted self-assembly of gold nanoparticles onto a gold patterned Si substrate.

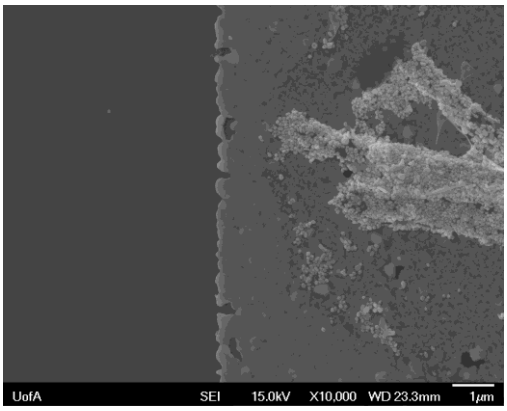

Figure 4-61 SEM image of 200 nm gold nanoparticles on a gold patterned silicon substrate after the first attempt.

Figure 4-61 shows the initial result in the form of an SEM (JAMP-9500F at ACSES, University of Alberta) image obtained by performing the DNA-assisted self-assembly using 200 nm sized gold nanoparticles onto a gold patterned silicon substrate.

We found selective attachment of the gold nanoparticles in the target DNA rich gold patterned region. But in the SEM image, we can also see that the gold

nanoparticles are attached to the Si substrate in an aggregated manner. I wondered if the gold nanoparticles were aggregated as purchased. To test this, I dropped around 250 μL of the original gold nanoparticle solution on a bare silicon substrate and stored it for two days, letting the sample dry in ambient conditions.

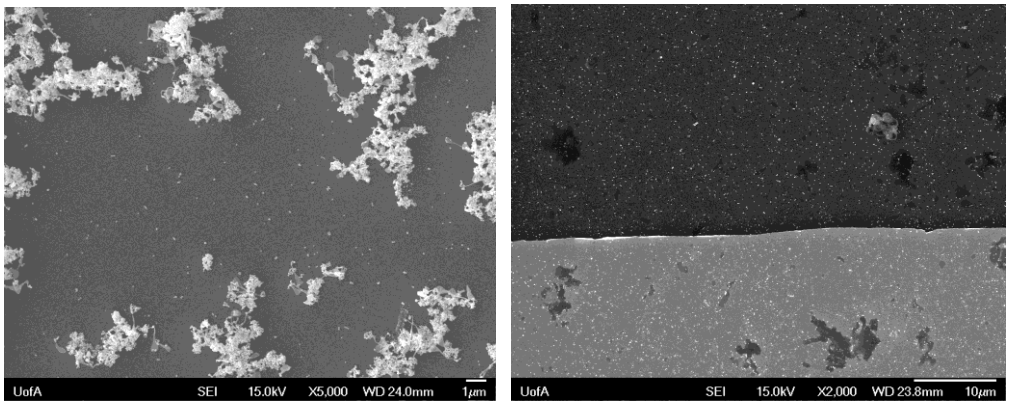

Figure 4-62: Gold nanoparticles aggregated (left). Gold nanoparticles well dispersed after sonication (right).

An SEM image (Figure 4-62, left) of the dried sample showed that the gold nanoparticles came as aggregates in solution. Because dispersed particles are expected to react more efficiently than aggregated particles, an ultrasonication step was performed additionally to disperse the gold nanoparticles. Figure 4-62 (right) shows an SEM image of the 200 nm gold nanoparticles after the ultrasonication step. Hereafter, a 10 minute ultrasonication step was added before experiments with gold nanoparticles. In addition, I performed a similar self-assembly experiment using 50 nm sized gold nanoparticles, but found it hard to distinguish between the gold film on the substrate and the smaller 50 nm sized gold nanoparticles during SEM analysis.

4.4.6.1 Gold nanoparticles on Si substrates half patterned with gold

To find the selectivity of the attachment of the gold nanoparticles, the Si substrate was half patterned with gold film, and single stranded target DNA was attached. The gold-thiol reaction allows DNA to preferentially attach to the gold rich region of the substrate. The complementary type 2 DNA strand attached to the gold nanoparticles (200 nm) was dropped onto the half patterned substrate and kept in humid conditions overnight. Before washing away the excess solution, the temperature of the substrate was raised to 55 °C, then cooled to room temperature (Figure 4-63) to perform a simulated hybridization.

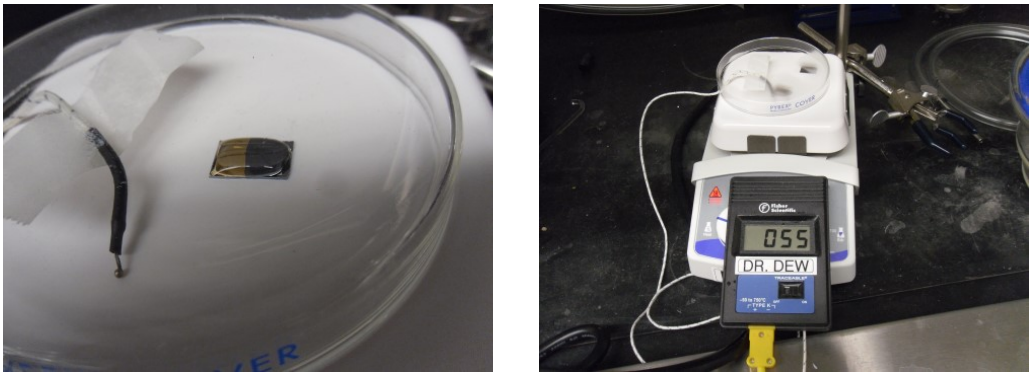

Figure 4-63: Gold half-patterned substrate with single stranded target DNA attached was reacted with complementary DNA attached to 200 nm gold nanoparticles (left). Experimental set up used to perform the annealing step by raising the temperature of the substrate to 55 °C (right).

After DNA hybridization, the substrate was rinsed with water then subjected to SEM imaging. The SEM image shows that most of the gold nanoparticles found were attached to the gold-rich areas on the substrate (Figure 4-64). Thus the annealing step improved the gold nanoparticle selectivity, and the self-assembly of 200 nm gold nanoparticles using the DNA hybridization technique was confirmed.

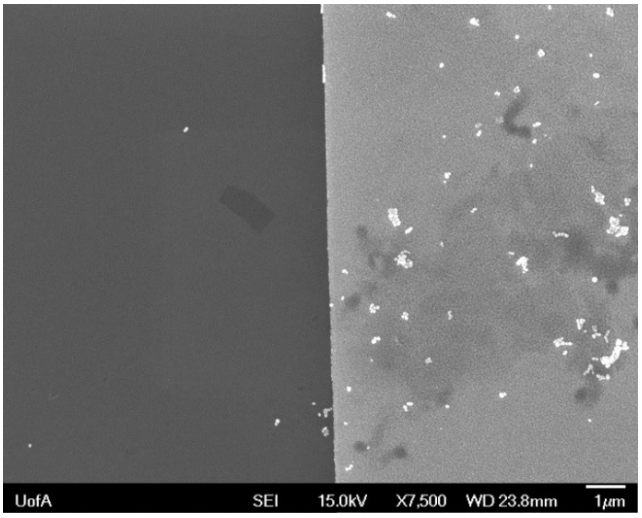

Figure 4-64 200 nm gold nanoparticles selectively attached to a Si substrate with a patterned gold surface.

4.4.6.2 Gold nanoparticles on Si substrate patterned using PR

Figure 4-65 shows the result obtained for another set of self-assembly experiments to attach the 50 nm sized gold nanoparticles to the patterned Si host substrate.

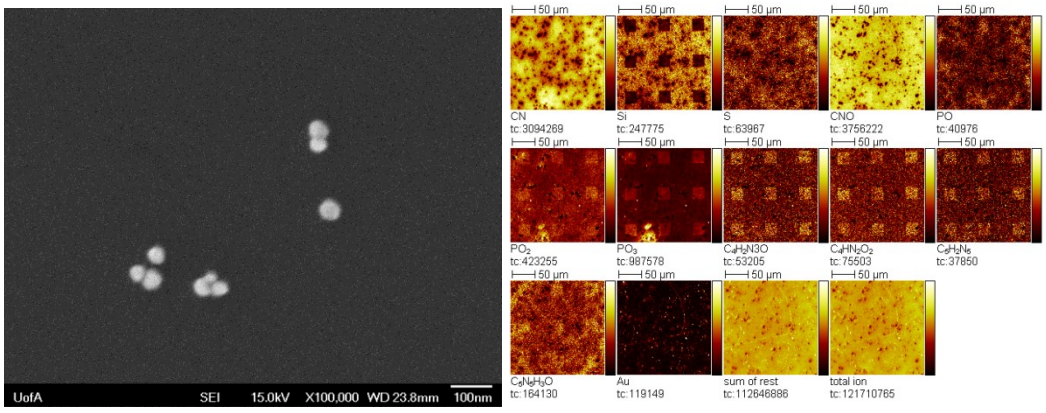

Figure 4-65 (left) SEM image showing the attachment of 50 nm gold nanoparticles onto Si substrate patterned with type 1 DNA using PR. (right) the ToF-SIMS result for the same sample after self-assembly experiment.

The type 1 DNA is covalently attached to the Si substrate using the method mentioned in section 4.3.3.1. In this case, I found a few 50 nm gold nanoparticles

attached to the substrate but not enough to observe a clear pattern. I subjected this sample to ToF-SIMS for further analysis (Figure 4-65 right). ToF-SIMS confirms the presence of DNA strands on the patterned region based on the signals from PO_2 and PO_3 groups, but randomized signal for the attached Au nanoparticles.

4.4.6.3 Gold nanoparticles on Si substrate patterned with gold lines

Another set of DNA-assisted self-assembly experiment was performed by preparing a Si host substrate patterned with approximately 100 and 25 μm thick lines of gold. Thiol terminated type 1 DNA strands were attached to the host substrate selectively on the gold lines. Type 2 DNA strands were attached to 200 nm sized gold nanoparticles which were then exposed to the host substrate for self-assembly.

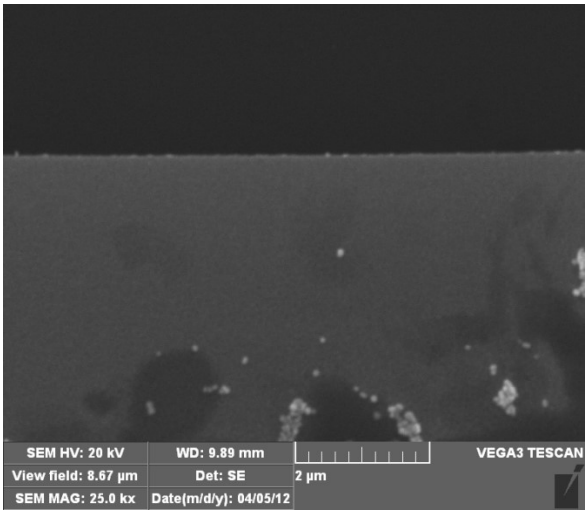

Figure 4-66 SEM image showing the attachment of 200 nm sized gold nanoparticle conjugated with type 2 DNA onto Si host substrate patterned with gold rich lines with complementary type 1 DNA.

Figure 4-66 shows the result obtained with the SEM image showing the selective attachment of the gold nanoparticles on the DNA rich gold region of the substrate.

This substrate was subjected for ToF-SIMS for further analysis, and the result is shown in Figure 4-67.

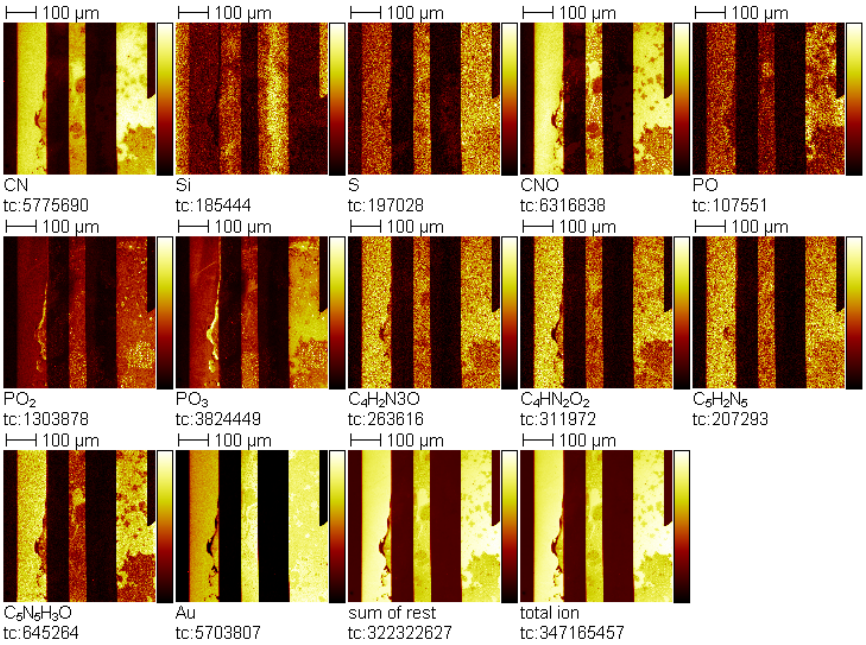

Figure 4-67 ToF-SIMS result after self-assembly experiment of 200 nm sized gold nanoparticle conjugated with type 2 DNA onto Si host substrate patterned with gold lines with complementary type 1 DNA.

From the ToF-SIMS result we can clearly see the Si and gold rich surface of the substrate differentially. It is evident that thiol terminated DNA is preferentially attached to the gold rich region with the presence of the PO_2, PO_3, $C_4H_2N_3O$, $C_4HN_2O_2$, $C_5H_2N_5$, $C_5N_5H_3O$ groups in the oligonucleotides. In the SEM result of Figure 4-66, we can see the preferential attachment of the gold nanoparticles onto the gold rich region. Conversely, from the ToF-SIMS, there is no signal indicating the presence of gold nanoparticles in the Si rich region. Hence, some degree of selectivity has been achieved through this procedure.

4.4.7 Self-assembly of microtiles fabricated without black wax using SSDNA

Based on the results obtained for self-assembly experiment using Si devices discussed in section 4.4.5 and comparing to the results obtained for the gold nanoparticles self-assembly discussed in above section 4.4.6, it is plausible that the presence of black wax, which was used as a release medium for the fabricated microchips could be the major possible chemical factor inhibited success of the Si devices assembly. An innovative work by Olsen *et al.* [93, 183] from our research group developed a technique to fabricate Si microchips from SOI wafer facilitating the release of the Si devices without involving black wax as opposed to the method discussed in section 4.3.1. Gold coated Si devices of 5 μm size fabricated using Olsen's front side release method were subjected to DNA-assisted self-assembly experiment. The same oligonucleotides mentioned in Table 4-1 were used but with a longer spacer group to add some extra compliance in the structure.

For performing the self-assembly experiment, the thiol terminated oligonucleotides were allowed to form gold-thiol based SAMs on the target gold pads and the gold coated microtiles. To functionalize the SOI microtile substrate 60 μL of the 1mM oligonucleotide solution was added to a clean 50 mL centrifuge tube and then added 16 μL of TCEP solution. The final volume was made to 6 mL using TEA buffer. The solution mixture is gently vortexed followed by submersing the SOI microtile substrate and left upright for an overnight. Similarly using 15 μL of 1mM oligonucleotide solution with 4 μL of TCEP solution and diluted to a final volume of 1.5 mL with TEA buffer. This solution mixture is used for submersing the target pad substrate upright for functionalization overnight. After removing

from the functionalization solution mixture, the microtiles substrate was rinsed with water and subjected to sonication method for 50 mins to release the microtiles into 2x SSPE hybridization buffer for assembly experiment. Removed from the functionalization solution, the target pad was lightly rinsed with water, dried and kept in the hybridization buffer with the release microtiles. With the help of small magnetic stir bar, the solution was cycled through stirring for 10 seconds and allowed 1 minute settling time using a timer for 24 hours. The target pad removed after 24 hours was rinsed with HPLC water, dried and imaged using SEM (Figure 4-68).

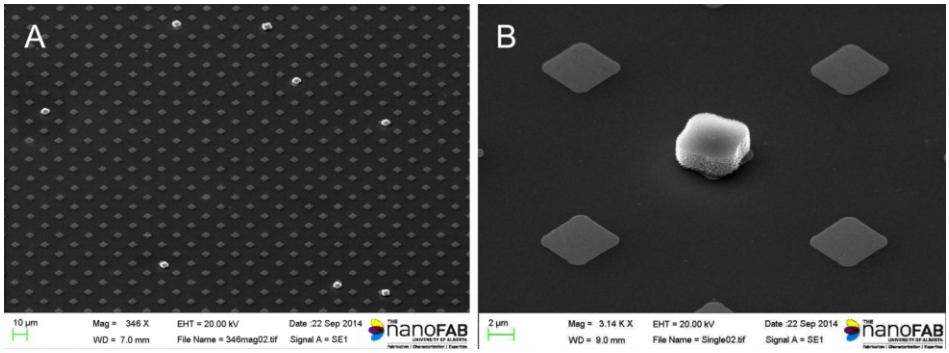

Figure 4-68 5 µm silicon microtiles (white) selectively attached to a Si (black) substrate with a patterned gold surface (grey) using the single stranded DNA hybridization interaction [183]. (A) Lower magnification SEM image showing the low yield but good selective assembly of microtiles on the target pads. (B) Higher magnification SEM image showing the microtile attached to the target gold pad.

As evident in Figure 4-68A, even though the yield of target pads covered by microtiles was low, the selective attachment of the microtiles on to the patterned target pad is noticeable. Further, all attached die was situated in contact with a bonding pad, indicating high selectivity, as hoped. The experiment succeeded in demonstrating that the DNA hybridization forces are strong enough to selectively assemble microscale silicon microtiles. In Figure 4-68B, we can see the Si microchip self-assembled in a well centered position onto the target pad exactly as

hoped at the outset. From this self-assembly experiment using 5 μm sized microtiles, the idea of using DNA hybridization as a technique to self-assemble Si devices is clearly validated. In addition, it also supports the hypothesis that the black wax was an inhibiting factor for Si device release procedure seen in section 4.3.1. Further studies, with additional changes to the procedure and experimental conditions could possibly further improve the yield of assembly of Si microchips using this DNA hybridization technique.

4.5 Conclusions

DNA-assisted self-assembly experiments have been performed using Si model devices. Microfabrication techniques were exploited to prepare 25 μm and 100 μm sized silicon micro/nanochip devices for DNA-assisted self-assembly. Black wax was used to free the devices from the mother substrate for self-assembly. DNA was attached covalently to patterned Si or to gold coated substrates using a thiol gold reaction and the intermediate experimental steps were characterized using various techniques including contact angle measurements. XPS and ellipsometry were used to confirm SAM and SSMCC linkages. ToF-SIMS and fluorescence microscopy were used to verify oligomer attachment and binding.

The characterization results confirmed the selective attachment of the DNA onto the host substrates. Self-assembly results using Si model devices seem to be more challenging than initially thought, and I came across various issues that need to be resolved for feasibility of this technique on an industrial level.

Insufficient contact between the devices and the host substrate for sufficient hybridization to occur was potentially an issue, so I tried delivering the devices

directly on top of the host substrate directly from the membrane filter. However, for experiments with Si model devices I could not get convincing selective attachment to the patterned substrate region. I tried to introduce an annealing step but did not find any improvement, for both 25 μm and 100 μm sized devices on both patterned Si and gold coated substrate.

Binding force calculations were performed to compare the attachment and release forces on the devices with different sizes and shapes. These suggest a wide range of viable sizes provided good binding can be achieved. Preventing such binding could be steric hindrance or the presence of black wax or salt contamination. Alternate procedures that reduce these factors are recommended.

Further studies were performed to understand possible causes to resolve the challenges for the DNA-assisted self-assembly method. To investigate size effects, I attempted self-assembly with smaller gold nanoparticles (50 and 200 nm sized). Selective attachment of 200 nm sized gold nanoparticles conjugated with DNA strands was achieved onto a Si substrate patterned with gold and conjugated with complementary DNA strands. The selective attachment observed with the 200 nm gold nanoparticles does validate the concept of DNA-based attachment of devices larger than molecular scale.

In addition, an alternate approach using Olsen's method to fabricate functionalized microtiles without involving any black wax produced promising results for 5 μm sized microtiles with good selectivity. Further work is recommended to better understand the respective roles of contributing factors like steric effects using different spacers, longer or shorter oligo sequences, and oligonucleotide concentration to improve the yield of device assembly.

5 Summary and Future Work

5.1 Summary

Packaging techniques involved in the heterogeneous integration of micro/nano-sized parts were reviewed in chapter 1. Current industrial integration techniques are limited as the size of the parts reduces to the nanoscale. Serial methods like robotic pick-and-place have limitations in the speed and size of the parts that can be handled. Commercialized fluidic self-assembly is limited to a size of 300 μm and above. A self-assembly technique is needed for the development of advanced MEMS/NEMS devices but the available self-assembly techniques have many limitations. Researchers are increasingly interested in biomolecule-assisted self-assembly techniques. This thesis reports the use of DNA for the self-assembly of micro/nanoelectronic devices to gain new understanding of this technique. DNA molecules were chosen for the self-assembly technique because of their ability to hybridize, the ease with which they are controlled by temperature, and the possibility of strong covalent attachment of DNA to Si substrates.

This thesis explored a theoretical modeling approach to better understand the DNA self-assembly mechanism to gain more control to utilize the technique. A theoretical modeling tool using MM/3D-RISM-KH method is introduced to calculate binding free energy of ds-DNA strands. The binding energy of the ds-DNA was calculated by employing the 3D-RISM-KH theory to calculate the solvation free energy and results obtained suggest that 3D-RISM-KH is better than the GB/PBSA method in the determination of solvation free energy on validation. DNA melting curve for the ds-DNA used for experiments were obtained, and a

temperature range to perform self-assembly using simulated hybridization to improve the non-specific binding of the DNA strands is predicted using the theoretical model of MM/3D-RISM-KH. In addition, the contribution of the salt concentration onto the binding of the ds-DNA was also investigated using MM/GBSA and a semi-empirical tool with Na+ and K+ ions, which should be a key factor in maintaining the original structure of the DNA strands to promote the hybridization and hence the selectivity of device assembly. The theoretical model could further evolve to calculate the energies of DNA strands tethered to various solid substrates like Si. Further, instead of just explicit water, this model could handle solvents like toluene, which might be part of the procedure to represent the DNA-assisted self-assembly experiments to provide more vital information for further steps of improvement of this technique.

Complementing the theoretical work, DNA-assisted self-assembly experiments were conducted using Si model devices onto patterned Si substrates. A method to fabricate devices assembled on a Si substrate was demonstrated. The steps to covalently attach DNA strands to a silicon substrate and to a gold-coated Si substrate were investigated using various characterization techniques and the results indicated that selective attachment of DNA to the host substrate surface was achieved. DNA-assisted self-assembly experiments were performed initially using fabricated 25 μm and 100 μm sized Si model devices but with limited success. The possible physical and chemical causes and some improvements were suggested. To further validate the procedure and the size of the devices a short-stranded DNA can handle, the experiment was performed using 200 nm sized gold nano-particles which provided positive results with less yield. This confirmed that

DNA-assisted self-assembly technique is working for devices in the molecular and nano-scale range. Also, a simulated hybridization performed showed improved selectivity. Since the presence of black wax is evident on the host substrate and source is from the Si microtiles fabrication and it seems to be the major factor hindering the DNA binding process. An alternate approach to fabricate the micro devices of 5 um sizes without using black wax for device release from the mother substrate is used. The DNA derivatized 5 um microtiles were successfully self-assembled onto the patterned host substrate with very good selectivity. The absence of black wax in this method is helping to get selective attachment of the microtiles to the host substrate. Further studies are recommended to better understand the role of various contributing factors to improve the yield of attachment of the devices onto the substrate.

5.2 Future work

In this thesis, theoretical modeling is performed using the DNA strands in a free state and using water as the explicit solvent. As this research progressed, several improvements were seen in the MD simulation study of the DNA strands tethered to various solid surfaces [36, 86, 184]. A similar study with a Si based substrate with the covalently attached DNA is recommended for creating trajectories for the binding energy calculations using MM/3D-RISM-KH model. Recently 3D-RISM-KH model is found applied for various studies using different solvent types like cyclohexane and toluene [81, 82]. This feature could further improve the calculations of the energies to represent the experimental conditions using various solvents instead of just water. Recent implementation of the 3D-RISM-KH module

in the newer version of AMBER molecular dynamics package with the improved force fields availability can speed up and improve the accuracy of the energy calculations and popularize this model. This could potentially contribute to facilitating further research in related fields to aid in minimizing the experimental expense and effort requirements.

Complementing the modeling, in the experimental part of this thesis, DNA-assisted self-assembly was successful applied to assemble Si model devices with good selectivity. It is recommended to fabricate model devices without using black wax for device release for further studies. Further research is recommended to improve the yield of assembly. Recent related research [174, 175] highlights the use of an electric field to increase the impingement of the complementary DNA strands to the target DNA attached to the substrate surface. This is based on the concept that negatively charged DNA would be attracted to a positive potential applied to the substrate. In addition, the experiments in thesis were implemented using microtiles and spherical shaped gold nanoparticles, but the use of devices with different sizes and geometrical shapes should give a better idea of their behavior in this technique. Furthermore, DNA-assisted self-assembly of devices was performed using only one pair of complementary DNA sequences. Multiple DNA sequences might provide information about the selectivity of DNA in device assembly. Further studies using different sized spacers or implementation of techniques like nanografting [185] or using nanofluidic filters [186] to immobilize DNAs are recommended to understand the role of steric effects on DNA-assisted self-assembly technique.

References

[1] M. Despont, "Heterogeneous device integration," *ibm.com,* [Online]. Available: http://www.zurich.ibm.com/st/server/microdevice.html. [Accessed: Feb. 12, 2010].

[2] K. Bohringer, K. Goldberg, M. Cohn, R. Howe and A. Pisano, "Parallel microassembly with electrostatic force fields," *Proceedings - IEEE International Conference on Robotics and Automation*, vol. 2, pp. 1204-1211, 1998.

[3] Humanrobo, "TOSY Parallel robot," *wikimedia.org,* [Online]. Available: https://commons.wikimedia.org/wiki/File:TOSY_Parallel_Robot.JPG. [Accessed: Jan. 12, 2018].

[4] R. E. Holmlin, M. Schiavoni, C. Y. Chen, S. P. Smith, M. G. Prentiss and G. M. Whitesides, "Light-driven microfabrication: Assembly of multicomponent, three-dimensional structures by using optical tweezers," *Angewandte Chemie - International Edition*, vol. 39, no. 19, pp. 3503-3506, 2000.

[5] G. Sinclair, P. Jordan, J. Laczik, J. Courtial and M. Padgett, "Semi-automated 3-dimensional assembly of multiple objects using holographic optical tweezers," *Proceedings of SPIE - The International Society for Optical Engineering*, vol. 5514, pp. 137-142, 2004.

[6] T. Yu, F. Cheong and C. Sow, "The manipulation and assembly of CuO nanorods with line optical tweezers," *Nanotechnology*, vol. 15, no. 12, pp. 1732-1736, 2004.

[7] K. C. Chhabra, D. K. Gupta and O. P. Arora, "FLIP CHIP BONDING." *J Inst Electron Telecommun Eng*, vol. 21, no. 5, pp. 292-294, 1975.

[8] Y. Takahashi, H. Fukuda, Y. Yoneshima, H. Kitamura and M. Maeda, "Solid-State Microjoining Mechanisms of Wire Bonding and Flip Chip Bonding," *J Electron Packag, Trans ASME*, vol. 139, no. 4, 2017.

[9] K. Kim, "Flip Chip," *amkor.com,* [Online]. Available: https://amkor.com/technology/flip-chip/. [Accessed: Jan 14, 2018].

[10] C. J. Morris, S. A. Stauth and B. A. Parviz, "Self-assembly for microscale and nanoscale packaging: Steps toward self-packaging," *IEEE Transactions on Advanced Packaging*, vol. 28, no. 4, pp. 600-611, 2005.

[11] D. B. Wolfe, A. Snead, C. Mao, N. B. Bowden and G. M. Whitesides, "Mesoscale self-assembly: Capillary interactions when positive and negative menisci have similar amplitudes," *Langmuir*, vol. 19, no. 6, pp. 2206-2214, 2003.

[12] H. J. Yeh and J. S. Smith, "Fluidic self-assembly for the integration of GaAs light-emitting diodes on Si substrates," *IEEE Photonics Technology Letters*, vol. 6, no. 6, pp. 706-708, 1994.

[13] L. Stiff, "Alien technology,"*alientechnology.com*, [Online]. Available: http://www.alientechnology.com/technology/ fsa_manufacturing.php. [Accessed: Jan. 11, 2010].

[14] U. Srinivasan, M. A. Helmbrecht, C. Rembe, R. S. Muller and R. T. Howe, "Fluidic self-assembly of micromirrors onto microactuators using capillary forces," *IEEE Journal on Selected Topics in Quantum Electronics*, vol. 8, no. 1, pp. 4-11, 2002.

[15] C. J. Morris, S. A. Stauth and B. A. Parviz, "Using capillary forces for self-assembly of functional microstructures," in *2nd Conference on Foundations of Nanoscience: Self-Assembled Architectures and Devices, FNANO 2005*, Snowbird, Utah, USA, April 24-28, 2005.

[16] S. Biswas, M. Mozafari, T. Stauden and H.O. Jacobs, "Surface tension directed fluidic self-assembly of semiconductor chips across length scales and material boundaries," *Micromachines*, vol. 7, no. 4, 2016.

[17] J. Xiao, R. R. Chaudhuri and S. Seo, "Heterogeneous Integration of Thin-Film Optical Devices Utilizing Fluidic Self-Assembly and Micro-Pick-and-Place Technique," *IEEE Trans.Compon.Packag.Manufact.Tech.*, vol. 6, no. 8, pp. 1283-1289, 2016.

[18] M. Porta, G. Fantoni and P. Lambert, "An integrated and compact device for microassembly exploiting electrostatic sorting and capillary grasping," *CIRP J.Manuf.Sci.Technol.*, vol. 3, no. 3, pp. 185-190, 2010.

[19] S. W. Lee and R. Bashir, "Dielectrophoresis and electrohydrodynamics-mediated fluidic assembly of silicon resistors," *Appl.Phys.Lett.*, vol. 83, no. 18, pp. 3833-3835, 2003.

[20] C. A. Mirkin, R. L. Letsinger, R. C. Mucic and J. J. Storhoff, "A DNA-based method for rationally assembling nanoparticles into macroscopic materials," *Nature*, vol. 382, no. 6592, pp. 607-609, 1996.

[21] S. C. Esener, D. Hartmann, M. J. Heller and J. M. Cable, "DNA assisted micro-assembly: a heterogeneous integration technology for optoelectronics," in *SPIE – the International Society for Optical Engineering, SPIE Critical Reviews Series*, St. Petersburg, Russian Federation, 1998, pp. 113, 1998.

[22] L. M. Demers, C. A. Mirkin, R. C. Mucic, R. A. Reynolds III, R. L. Letsinger, R. Elghanian and G. Viswanadham, "A fluorescence-based method for determining the surface coverage and hybridization efficiency of thiol-capped oligonucleotides bound to gold thin films and nanoparticles," *Anal.Chem.*, vol. 72, no. 22, pp. 5535-554, 2000.

[23] S. Tanaka, M. Taniguchi and T. Kawai, "Adsorption of DNA molecule and DNA patterning on Si Substrate," in *DNA-Based Molecular Electronics: International Symposium on DNA-Based Molecular Electronics*, Jena, Germany, May 13-15, 2004.

[24] D. M. Hartmann, M. Heller, S. C. Esener, D. Schwartz and G. Tu, "Selective DNA attachment of micro- and nanoscale particles to substrates," *J.Mater.Res.*, vol. 17, no. 2, pp. 473-478, 2002.

[25] H. McNally, M. Pingle, S.W. Lee, D. Guo, D.E. Bergstrom and R. Bashir, "Self-assembly of micro- and nano-scale particles using bio-inspired events," *Appl.Surf.Sci.*, vol. 214, no. 1-4, pp. 109-119, 2003.

[26] R. Bashir, S. Lee, D. Guo, M. Pingle, D. Bergstrom, H.A. Mcnally and D. Janes, "Basic: Bio-inspired Assembly of Semiconductor Integrated Circuits," in *Materials Research Society Symposium - Proceedings*, vol. 636, pp. D1176, 2003.

[27] M. Yasuda, T. Hayashi, M. Michihata and Y. Takaya, "A novel batch fabrication of micro parts using DNA pattern recognition," *Key Eng Mat*, vol. 523-524, 2012.

[28] Y. Kim, M. Kim, H. Jung, Y. Choi, C.J. Kang, T. Yoon and H. H. Lee, "Electrical charging characteristics of Au NPs embedded by sequence specific complementary DNA hybridization in metal-pentacene-insulator-silicon device," *Bioch.J.*, vol. 8, no. 4, pp. 275-28, 2014.

[29] N. Lammerhardt, S. Merzsch, J. Ledig, A. Bora, A. Waag, M. Tornow and P. Mischnick, "Toward three-dimensional microelectronic systems: Directed self-assembly of silicon microcubes via DNA surface functionalization," *Langmuir*, vol. 29, no. 26, pp. 8410-8416, 2013.

[30] S. C. Esener and D. Hartmann, "DNA assisted microassembly:a heterogeneous integration technology for optoelectronics," *SPIE Critical Rev.Optical Sci.Technol.*, pp. 13-40, 1998.

[31] M. Alberti, E. Yacoub-George, W. Hell, C. Landesberger and K. Bock, "Biomolecular self-assembly of micrometer sized silica beads on patterned glass substrates," *Appl.Surf.Sci.*, vol. 255, no. 17, pp. 7759-7765, 2009.

[32] T. Tanemura, G. Lopez, R. Sato, K. Sugano, T. Tsuchiya, O. Tabata, M. Fujita and M. Maeda, "Sequential and selective self-assembly of micro components by DNA grafted polymer," *Proc. IEEE Int. Conf. Micro Electro Mech. Syst. MEMS*, pp. 184-187, 2010.

[33] T. Kusakabe, T. Tanemura, Y. Higuchi, K. Sugano, T. Tsuchiya and O. Tabata, "DNA mediated sequential self-assembly of nano/micro components," *Proc. IEEE Int. Conf. Micro Electro Mech. Syst. MEMS*, pp. 1052-1055, 2008.

[34] A. Singh, S. Snyder, L. Lee, A. P .R. Johnston, F. Caruso and Y. G. Yingling, "Effect of oligonucleotide length on the assembly of DNA materials: Molecular dynamics simulations of layer-by-layer DNA films," *Langmuir*, vol. 26, no. 22, pp. 17339-17347, 2010.

[35] P. S. Randeria, M. R. Jones, K. L. Kohlstedt, R. J. Banga, Olvera De La Cruz, M, G. C. Schatz and C. A. Mirkin, "What Controls the Hybridization Thermodynamics of Spherical Nucleic Acids?" *J.Am.Chem.Soc.*, vol. 137, no. 10, pp. 3486-3489, 2015.

[36] S. Monti, I. Cacelli, A. Ferretti, G. Prampolini and V. Barone, "Simulating DNA hybridization on an amine-functionalized silicon substrate," *J Phys Chem B*, vol. 114, no. 25, pp. 8341-8349, 2010.

[37] S. Genheden, T. Luchko, S. Gusarov, A. Kovalenko and U. Ryde, "An MM/3D-RISM approach for ligand binding affinities," *J Phys Chem B*, vol. 114, no. 25, pp. 8505-8516, 2010.

[38] A. Kovalenko, "Three-dimensional RISM theory for molecular liquids and solid-liquid interfaces," in *Molecular Theory of Solvation*, vol. 24, Dordrecht, The Netherlands: Kluwer Academic Publishers, 2003, pp. 169-275.

[39] K. J. Breslauer, R. Frank, H. Blocker and L. A. Marky, "Predicting DNA duplex stability from the base sequence," *Proc.Natl.Acad.Sci.U.S.A.*, vol. 83, no. 11, pp. 3746-3750, 1986.

[40] N. Le Novère, "MELTING, computing the melting temperature of nucleic acid duplex," *Bioinformatics*, vol. 17, no. 12, pp. 1226-1227, 2001.

[41] A. Kovalenko, "*Three-dimensional RISM theory for molecular liquids and solid-liquid interfaces*," in *Molecular Theory of Solvation*, vol. 24, Dordrecht, The Netherlands: Kluwer Academic Publishers, 2003, pp. 169-275.

[42] N. C. Seeman, "DNA nanotechnology: Novel DNA constructions," *Annual Review of Biophysics and Biomolecular Structure*, vol. 27, 1998.

[43] N.C. Seeman, "From genes to machines: DNA nanomechanical devices," *Trends Biochem.Sci.*, vol. 30, no. 3, pp. 119-125, 2005.

[44] Jean-Marie Lehn, "Supramolecular chemistry: from molecular information towards self-organization and complex matter," *Reports on Progress in Physics*, vol. 67, no. 3, pp. 249, 2004.

[45] H. W. Fink, "Electrical conduction through DNA molecules,", vol. 544, pp. 457. in *ELECTRONIC PROPERTIES OF NOVEL MATERIALS—MOLECULAR NANOSTRUCTURES: XIV International Winterschool/Euroconference*, Kirchberg, 2000, pp. 457, 2000.

[46] B. Hartzell, B. McCord, D. Asare, H. Chen, J. J. Heremans and V. Soghomonian, "Comparative current-voltage characteristics of nicked and repaired λ-DNA," *Appl.Phys.Lett.*, vol. 82, no. 26, pp. 4800-4802, 2003.

[47] P. Tran, B. Alavi and G. Gruner, "Charge transport along the λ-DNA double helix," *Phys.Rev.Lett.*, vol. 85, no. 7, pp. 1564-1567, 2000.

[48] A. Y. Kasumov, M. Kociak, S. Guron, B. Reulet, V. T. Volkov, D. V. Klinov and H. Bouchiat, "Proximity-induced superconductivity in DNA," *Science*, vol. 291, no. 5502, pp. 280-282, 2001.

[49] H. Simchi, M. Esmaeilzadeh and H. Mazidabadi, "Proximity-induced superconductivity effect in a double-stranded DNA," *J.Appl.Phys.*, vol. 115, no. 5, 2000.

[50] P. J. De Pablo, F. Moreno-Herrero, J. Colchero, J. Gómez Herrero, P. Herrero, A. M. Baró, P. Ordejón, J. M. Soler and E. Artacho, "Absence of dc-conductivity in λ-DNA," *Phys.Rev.Lett.*, vol. 85, no. 23, pp. 4992-4995, 2000.

[51] E. Braun, Y. Eichen, U. Sivan and G. Ben-Yoseph, "DNA-templated assembly and electrode attachment of a conducting silver wire," *Nature*, vol. 391, no. 6669, pp. 775-778, 1998.

[52] A. J. Storm, J. Van Noort, S. De Vries and C. Dekker, "Insulating behavior for DNA molecules between nanoelectrodes at the 100 nm length scale," *Appl.Phys.Lett.*, vol. 79, no. 23, pp. 3881-3883, 2001.

[53] D. Porath, A. Bezryadin, S. De Vries and C. Dekker, "Direct measurement of electrical transport through DNA molecules," *Nature*, vol. 403, no. 6770, pp. 635-638, 2000.

[54] A. Rakitin, P. Aich, C. Papadopoulos, Y. Kobzar, A. S. Vedeneev, J. S. Lee and J. M. Xu, "Metallic conduction through engineered DNA: DNA nanoelectronic building blocks," *Phys.Rev.Lett.*, vol. 86, no. 16, pp. 3670-3673, 2001.

[55] J. Qian, S. Liao, S. Xu, M. A. Stroscio and M. Dutta, "Direct measurement of electrical transport through single DNA molecules," *J.Appl.Phys.*, vol. 106, no. 3, 2009.

[56] E. M. Conwell and S. V. Rakhmanova, "Polarons in DNA," *Proc.Natl.Acad.Sci.U.S.A.*, vol. 97, no. 9, pp. 4556-4560, 2000.

[57] G. B. Schuster, "Long-range charge transfer in DNA: Transient structural distortions control the distance dependence," *Acc.Chem.Res.*, vol. 33, no. 4, pp. 253-260, 2000.

[58] M. Bixon, B. Giese, S. Wessely, T. Langenbacher, M. E. Michel-Beyerle and J. Jortner, "Long-range charge hopping in DNA," *Proc.Natl.Acad.Sci.U.S.A.*, vol. 96, no. 21, pp. 11713-11716, 1999.

[59] C. Murphy, M. Arkin, Y. Jenkins, N. Ghatlia, S. Bossmann, N. Turro and J. Barton, "Long-range photoinduced electron transfer through a DNA helix," *Science*, vol. 262, no. 5136, pp. 1025-1029, 1993.

[60] K. S. Kim, S. K. Ahn, Y. Lee, J. M. Lee and Y. Roh, "Effects of gate voltage on the characteristics of source-drain current formed through DNA molecules," *Thin Solid Films*, vol. 515, no. 2 SPEC. ISS., pp. 822-826, 2006.

[61] H. Yan, P. Yin, S. H. Park, H. Li, L. Feng, X. Guan, D. Liu, J. H. Reif and T. H. LaBean, "Self-assembled DNA Structures for Nanoconstruction," *AIP Conf.Proc.*, vol. 725, no. 1, pp. 43-52, 2004.

[62] T. Strother, R. J. Hamers and L. M. Smith, "Covalent attachment of oligodeoxyribonucleotides to amine-modified Si (001) surfaces," *Nucleic Acids Res.*, vol. 28, no. 18, pp. 3535-3541, 2000.

[63] K. Ishibashi, K. Tanaka, A. Hirano-Iwata, K. Miyamoto, Y. Kimura and M. Niwano, "In situ study of DNA attachment and hybridization at silicon surfaces by infrared absorption spectroscopy," *Japanese Journal of Applied Physics*, vol. 47, no. 4 PART 2, pp. 3204-3208, 2008.

[64] J. A. Milton, S. Patole, H. Yin, Q. Xiao, T. Brown and T. Melvin, "Efficient self-assembly of DNA-functionalized fluorophores and gold nanoparticles with DNA functionalized silicon surfaces: The effect of oligomer spacers," *Nucleic Acids Res.*, vol. 41, no. 7, 2013.

[65] S. Tanaka, M. Taniguchi and T. Kawai, "Selective adsorption of DNA onto SiO2 surface in SiO 2/SiH pattern," *Jpn J Appl Phys Part 1 Regul Pap Short Note Rev Pap*, vol. 43, no. 10, pp. 7346-7349, 2004.

[66] K. Sarveswaran, W. Hu, P. W. Huber, G. H. Bernstein and M. Lieberman, "Deposition of DNA rafts on cationic SAMs on silicon 100," *Chem.Soc.Rev.*, vol. 22, no. 26, pp. 11279-11283, 2006.

[67] L. Häussling, H. Ringsdorf, F. Schmitt and W. Knoll, "Biotin-functionalized self-assembled monolayers on gold: Surface plasmon optical studies of specific recognition reactions," *Langmuir*, vol. 7, no. 9, pp. 1837-1840, 1991.

[68] M. Hegner, "Immobilizing DNA on gold via thiol modification for atomic force microscopy imaging in buffer solutions," *FEBS Lett.*, vol. 336, no. 3, pp. 452-456, 1993.

[69] A. Aviram and M.A. Ratner, "Molecular rectifiers," *Chemical Physics Letters*, vol. 29, no. 2, pp. 277-283, 1974.

[70] K. Keren, M. Krueger, R. Gilad, G. Ben-Yoseph, U. Sivan and E. Braun, "Sequence-specific molecular lithography on single DNA molecules," *Science*, vol. 297, no. 5578, pp. 72-75, 2002.

[71] J. P. Yesudas, T. Olsen, J. Ng, A. Kovalenko and S. K. Dew, "Deoxyribonucleic acid mediated heterogeneous integration of micro- and nanoscale devices," *J.Nanosci.Nanotechnol.*, vol. 16, no. 7, pp. 7301-7313, 2016.

[72] C. Holste, A. Sondermann, R. Moller and W. Fritzsche, "Coupling G-Wires To Metal Nanoparticles," *AIP Conf.Proc.*, vol. 725, no. 1, pp. 53-58, 2004.

[73] J. Kondo, Y. Tada, T. Dairaku, Y. Hattori, H. Saneyoshi, A. Ono and Y. Tanaka, "A metallo-DNA nanowire with uninterrupted one-dimensional silver array," *Nat.Chem.*, vol. 9, no. 10, pp. 956-960, 2017.

[74] C. Wlti, R. Sharma and G. Davies, "RecA protein mediated nano-scale patterning of DNA scaffolds," *INEC - Int. Nanoelectronics Conf., Proc.*, pp. 358-359, 2010.

[75] Y. Shacham-Diamand, A. Inberg, Y. Sverdlov, V. Bogush, N. Croitoru, H. Moscovich and A. Freeman, "Electroless processes for micro- and nanoelectronics," *Electrochim.Acta*, vol. 48, no. 20-22, pp. 2987-2996, 2003.

[76] E. Gazit, "Use of biomolecular templates for the fabrication of metal nanowires," *FEBS Journal*, vol. 274, no. 2, pp. 317-322, 2007.

[77] C. M. Niemeyer and M. Adler, "Nanomechanical devices based on DNA," *Angewandte Chemie - International Edition*, vol. 41, no. 20, pp. 3779-3783, 2002.

[78] M. Massey, I. L. Medintz, M. G. Ancona and W. R. Algar, "Time-Gated FRET and DNA-Based Photonic Molecular Logic Gates: AND, OR, NAND, and NOR," *ACS Sensors*, vol. 2, no. 8, pp. 1205-1214, 2017.

[79] Z. Lin, T. Strother, W. Cai, X. Cao, L. M. Smith and R. J. Hamers, "DNA attachment and hybridization at the silicon (100) surface," *Langmuir*, vol. 18, no. 3, pp. 788-796, 2002.

[80] G. Lopez, T. Tanemura, R. Sato, T. Saeki, Y. Hirai, K. Sugano, T. Tsuchiya, O. Tabata, M. Fujita and M. Maeda, "DNA-grafted-polymer mediated self-assembly of micro components," *IEEE Int. Conf. Nano/Micro Eng. Mol. Syst., NEMS*, pp. 245-249, 2010.

[81] S. Hlushak and A. Kovalenko, "Effective Interactions and Adsorption of Heterocyclic Aromatic Hydrocarbons in Kaolinite Organic Solutions Studied by 3D-RISM-KH Molecular Theory of Solvation," *J.Phys.Chem.C*, vol. 121, no. 40, pp. 22092-22104, 2017.

[82] W. Huang, G.K. Dedzo, S.R. Stoyanov, O. Lyubimova, S. Gusarov, S. Singh, H. Lao, A. Kovalenko and C. Detellier, "Molecule-surface recognition between heterocyclic aromatic compounds and kaolinite in toluene investigated by molecular theory of solvation and thermodynamic and kinetic experiments," *J.Phys.Chem.C*, vol. 118, no. 41, pp. 23821-23834, 2014.

[83] J. H. Parish, "Principles of Nucleic Acid Structure: by W Saenger. pp 556. Springer-Verlag, New York. 1984. DM 79. ISBN 3-540-90761-0," *Biochem.Educ.*, vol. 13, no. 2, pp. 92, 1984.

[84] K. Wong and B. M. Pettitt, "A study of DNA tethered to a surface by an all-atom molecular dynamics simulation," *Theoretical Chemistry Accounts*, vol. 106, no. 3, pp. 233-235, 2001.

[85] P. Várnai and K. Zakrzewska, "DNA and its counterions: A molecular dynamics study," *Nucleic Acids Res.*, vol. 32, no. 14, pp. 4269-4280, 2004.

[86] O. Lee and G. C. Schatz, "Interaction between DNAs on a gold surface," *Journal of Physical Chemistry C*, vol. 113, no. 36, pp. 15941-15947, 2009.

[87] T. Yamazaki, N. Blinov, D. Wishart and A. Kovalenko, "Hydration Effects on the HET-s Prion and Amyloid-β Fibrillous Aggregates, Studied with Three-Dimensional Molecular Theory of Solvation," *Biophys.J.*, vol. 95, no. 10, pp. 4540-4548, 2008.

[88] N. Blinov, L. Dorosh, D. Wishart and A. Kovalenko, "Association thermodynamics and conformational stability of β-sheet amyloid β (17-42) oligomers: Effects of E22Q (Dutch) mutation and charge neutralization," *Biophys.J.*, vol. 98, no. 2, pp. 282-296, 2010.

[89] I. Massova and P. A. Kollman, "Combined molecular mechanical and continuum solvent approach (MM-PBSA/GBSA) to predict ligand binding," *Perspect.Drug Discov.Des.*, vol. 18, pp. 113-135, 2000.

[90] P. A. Kollman, I. Massova, C. Reyes, B. Kuhn, S. Huo, L. Chong, M. Lee, T. Lee, Y. Duan, W. Wang and O. Donini, "Calculating structures and free energies of complex molecules: Combining molecular mechanics and continuum models," *Acc.Chem.Res.*, vol. 33, no. 12, pp. 889-897, 2000.

[91] H. Gohlke and D. A. Case, "Converging Free Energy Estimates: MM-PB(GB)SA Studies on the Protein-Protein Complex Ras-Raf," *Journal of Computational Chemistry*, vol. 25, no. 2, pp. 238-250, 2004.

[92] J. Ng and S.K. Dew, “Fabrication of silicon microtiles using epitaxial lift-off (ELO),” presented at iCORE AECEGRS, 2009, Edmonton, Canada. 2009.

[93] T. Olsen, J. Ng, M. Stepanova and S.K. Dew, “Programmed Self-Assembly of Microscale Components Using Biomolecular Recognition through the Avidin-Biotin Interaction,” *Journal of Vacuum Science and Technology B*. vol. 32, no. 6, 2014.

[94] L. Moiseev, M.S. Ünlü, A.K. Swan, B.B. Goldberg and C.R. Cantor, “DNA conformation on surfaces measured by flourescence self-interference,” *Proc.Natl.Acad.Sci.U.S.A.*, vol. 103, no. 8, pp. 2623-2628, 2006.

[95] D. Proudnikov and A. Mirzabekov, "Chemical methods of DNA and RNA fluorescent labeling,” *Nucleic Acids Res.*, vol. 24, no. 22, pp. 4535-4542, 1996.

[96] B. Lang, “Hybridization thermodynamics of DNA bound to gold nanoparticles,” *J Chem Thermodyn*, vol. 42, no. 12, pp. 1435-1440, 2010.

[97] L. A. Marky and K. J. Breslauer, “Calorimetric determination of base-stacking enthalpies in double-helical DNA molecules.” *Biopolymers*, vol. 21, no. 11, pp. 2185-2194, 1982.

[98] N. Sugimoto, S. Nakano, M. Yoneyama and K. Honda, “Improved thermodynamic parameters and helix initiation factor to predict stability of DNA duplexes,” *Nucleic Acids Res.*, vol. 24, no. 22, pp. 4501-4505, 1996.

[99] J. SantaLucia Jr., H. T. Allawi and P. A. Seneviratne, “Improved nearest-neighbor parameters for predicting DNA duplex stability,” *BIOCHEMISTRY*, vol. 35, no. 11, pp. 3555-3562, 1996.

[100] J. SantaLucia Jr., “A unified view of polymer, dumbbell, and oligonucleotide DNA nearest-neighbor thermodynamics,” *Proc.Natl.Acad.Sci.U.S.A.*, vol. 95, no. 4, pp. 1460-1465, 1998.

[101] A. Pérez, F. J. Luque and M. Orozco, “Frontiers in molecular dynamics simulations of DNA.” *Acc.Chem.Res.*, vol. 45, no. 2, pp. 196-205, 2012.

[102] M. Orozco, A. Noy and A. Pérez, “Recent advances in the study of nucleic acid flexibility by molecular dynamics,” *Curr.Opin.Struct.Biol.*, vol. 18, no. 2, pp. 185-193, 2008.

[103] T. E. Cheatham III, “Simulation and modeling of nucleic acid structure, dynamics and interactions,” *Curr.Opin.Struct.Biol.*, vol. 14, no. 3, pp. 360-367, 2004.

[104] O. Lee, T. R. Prytkova and G. C. Schatz, “Using DNA to link gold nanoparticles, polymers, and molecules: A theoretical perspective,” *Journal of Physical Chemistry Letters*, vol. 1, no. 12, pp. 1781-1788, 2010.

[105] D. Bashford and D. A. Case, “Generalized born models of macromolecular solvation effects,” *Annu Rev Phys Chem*, vol. 51, 2000.

[106] B. Honig and A. Nicholls, “Classical electrostatics in biology and chemistry,” *Science*, vol. 268, no. 5214, pp. 1144-1149, 1995.

[107] A. Onufriev, D. A. Case and D. Bashford, “Effective Born radii in the generalized Born approximation: The importance of being perfect,” *J.Comput.Chem.*, vol. 23, no. 14, pp. 1297-1304, 2002.

[108] Z. A. Sands and C. A. Laughton, “Molecular dynamics simulations of DNA using the generalized born solvation model: Quantitative comparisons with explicit solvation results,” *J Phys Chem B*, vol. 108, no. 28, pp. 10113-10119, 2004.

[109] J. Wagoner and N.A. Baker, "Solvation forces on biomolecular structures: A comparison of explicit solvent and poisson-boltzmann models," *Journal of Computational Chemistry*, vol. 25, no. 13, pp. 1623-1629, 2004.

[110] A. Kovalenko and F. Hirata, "Three-dimensional density profiles of water in contact with a solute of arbitrary shape: A RISM approach," *Chemical Physics Letters*, vol. 290, no. 1-3, pp. 237-244, 1998.

[111] T. Yamazaki, H. Fenniri and A. Kovalenko, "Structural water drives self-assembly of organic rosette nanotubes and holds host atoms in the channel," *ChemPhysChem*, vol. 11, no. 2, pp. 361-367, 2010.

[112] T. Imai, A. Kovalenko and F. Hirata, "Solvation thermodynamics of protein studied by the 3D-RISM theory," *Chemical Physics Letters*, vol. 395, no. 1-3, pp. 1-6, 2004.

[113] D. B. Abraham and H. Kunz, "Ornstein-Zernike theory of classical fluids at low density," *Phys.Rev.Lett.*, vol. 39, no. 16, pp. 1011-1014, 1977.

[114] A. Kovalenko, T. Luchko, S. Gusarov, D. R. Roe, C. Simmerling, D. A. Case and J. Tuszynski, "Three-dimensional molecular theory of solvation coupled with molecular dynamics in amber," *J.Chem.Theory Comput.*, vol. 6, no. 3, pp. 607-624, 2010.

[115] J. P. Yesudas, N. Blinov, S. K. Dew and A. Kovalenko, "Calculation of binding free energy of double stranded oligonucleotides using MM/3D-RISM-KH approach," *J. Mol. Liq.*, vol. 201, pp. 68-76, 2015.

[116] D. A. Case, T. E. Cheatham III, T. Darden, H. Gohlke, R. Luo, K. M. Merz Jr., A. Onufriev, C. Simmerling, B. Wang and R. J. Woods, "The Amber biomolecular simulation programs," *J.Comput.Chem.*, vol. 26, no. 16, pp. 1668-1688, 2005.

[117] D. A. Case, T. A. Darden, T. E. Cheatham III, C. L. Simmerling, J. Wang, R. E. Duke, R. Luo, M. Crowley, R. C. Walker, W. Zhang, K. M. Merz, B. Wang, B. Hayik, A. Roitberg, G. Seabra, I. Kolossv ry, K. F. Wong, F. Paesani, J. Vanicek, X. Wu, S. R. Brozell, T. Steinbrecher, H. Gohlke, L. Yang, C. Tan, J. Mongan, V. Hornak, G. Cui, G. G. Mathews, M. G. Seetin, C. Sagui, V. Babin and P. A. Kollman, "AMBER 10,", 2008.

[118] B. J. Alder and T. E. Wainwright, "Studies in molecular dynamics. I. General method," *J.Chem.Phys.*, vol. 31, no. 2, pp. 459-466, 1959.

[119] B. J. Alder and T. E. Wainwright, "Phase transition for a hard sphere system," *J.Chem.Phys.*, vol. 27, no. 5, pp. 1208-1209, 1957.

[120] M. P. Allen and D. J. Tildesley, *Computer Simulation of Liquids*. Oxford Science Publications, 1987.

[121] J. P. Hansen and I. R. McDonald, *Theory of Simple Liquids*. Elsevier Inc.
, 1986.

[122] F. Hirata, *Molecular Theory of Solvation*, vol. 24, Dordrecht, The Netherlands: Kluwer Academic Publishers, 2003.

[123] A. Kovalenko and F. Hirata, "Self-consistent description of a metal-water interface by the Kohn-Sham density functional theory and the three-dimensional reference interaction site model," *J.Chem.Phys.*, vol. 110, no. 20, pp. 10095-10112, 1999.

[124] A. Kovalenko, A.E. Kobryn, S. Gusarov, O. Lyubimova, X. Liu, N. Blinov and M. Yoshida, "Molecular theory of solvation for supramolecules and soft matter structures: Application to ligand binding, ion channels, and oligomeric polyelectrolyte gelators," *Soft Matter*, vol. 8, no. 5, pp. 1508-1520, 2012.

[125] Y. Maruyama, N. Yoshida and F. Hirata, "Electrolytes in biomolecular systems studied with the 3D-RISM/RISM theory," *Interdisciplinary Sciences: Computational Life Sciences*, vol. 3, no. 4, pp. 290-307, 2011.

[126] S. Phongphanphanee, N. Yoshida and F. Hirata, "On the proton exclusion of aquaporins: A statistical mechanics study," *J.Am.Chem.Soc.*, vol. 130, no. 5, pp. 1540-1541, 2008.

[127] S. Phongphanphanee, T. Rungrotmongkol, N. Yoshida, S. Hannongbua and F. Hirata, "Proton transport through the influenza A M2 channel: Three-dimensional reference interaction site model study," *J.Am.Chem.Soc.*, vol. 132, no. 28, pp. 9782-9788, 2010.

[128] N. Yoshida, T. Imai, S. Phongphanphanee, A. Kovalenko and F. Hirata, "Molecular recognition in biomolecules studied by statistical-mechanical integral-equation theory of liquids," *J Phys Chem B*, vol. 113, no. 4, pp. 873-886, 2009.

[129] J. S. Perkyns, G. C. Lynch, J. J. Howard and B. M. Pettitt, "Protein solvation from theory and simulation: Exact treatment of Coulomb interactions in three-dimensional theories," *J.Chem.Phys.*, vol. 132, 2010.

[130] A. Kovalenko, "Multiscale modeling of solvation in chemical and biological nanosystems and in nanoporous materials," *Pure and Applied Chemistry*, vol. 85, no. 1, pp. 159-169, 2013.

[131] K. Yoshida, T. Yamaguchi, A. Kovalenko and F. Hirata, "Structure of tert-butyl alcohol-water mixtures studied by the RISM theory," *J Phys Chem B*, vol. 106, no. 19, pp. 5042-5049, 2002.

[132] V. Shapovalov, T. N. Truong, A. Kovalenko and F. Hirata, "Liquid structure at metal oxide-water interface: Accuracy of a three-dimensional RISM methodology," *Chemical Physics Letters*, vol. 320, no. 1-2, pp. 186-193, 2000.

[133] J. Fafard, O. Lyubimova, S. R. Stoyanov, G. K. Dedzo, S. Gusarov, A. Kovalenko and C. Detellier, "Adsorption of indole on kaolinite in nonaqueous media: Organoclay preparation and characterization, and 3D-RISM-KH molecular theory of solvation investigation," *Journal of Physical Chemistry C*, vol. 117, no. 36, pp. 18556-18566, 2013.

[134] M. C. Stumpe, N. Blinov, D. Wishart, A. Kovalenko and V. S. Pande, "Calculation of local water densities in biological systems: A comparison of molecular dynamics simulations and the 3D-RISM-KH molecular theory of solvation," *J Phys Chem B*, vol. 115, no. 2, pp. 319-328, 2011.

[135] S. Genheden and U. L. F. Ryde, "How to obtain statistically converged MM/GBSA results," *J.Comput.Chem.*, vol. 31, no. 4, pp. 837-846, 2010.

[136] R. Galindo-Murillo, J. C. Robertson, M. Zgarbov, J. poner, M. Otyepka, P. Jurecka and T. E. Cheatham, "Assessing the Current State of Amber Force Field Modifications for DNA," *J.Chem.Theory Comput.*, vol. 12, no. 8, pp. 4114-4127, 2016.

[137] W. Huang, N. Blinov and A. Kovalenko, "Octanol-Water Partition Coefficient from 3D-RISM-KH Molecular Theory of Solvation with Partial Molar Volume Correction," *J Phys Chem B*, vol. 119, no. 17, pp. 5588-5597, 2015.

[138] J. Truchon, B. M. Pettitt and P. Labute, "A cavity corrected 3D-RISM functional for accurate solvation free energies," *J.Chem.Theory Comput.*, vol. 10, no. 3, pp. 934-941, 2014.

[139] T. Luchko, N. Blinov, G. C. Limon, K. P. Joyce and A. Kovalenko, "SAMPL5: 3D-RISM partition coefficient calculations with partial molar volume corrections and solute conformational sampling," *J.Comp.-Aided Mol.Des.*, vol. 30, no. 11, pp. 1115-1127, 2016.

[140] D. S. Palmer, A. I. Frolov, E. L. Ratkova and M. V. Fedorov, "Towards a universal method for calculating hydration free energies: A 3D reference interaction site model with partial molar volume correction," *J Phys Condens Matter*, vol. 22, no. 49, 2010.

[141] L. E. Morrison and L. M. Stols, "Sensitive fluorescence-based thermodynamic and kinetic measurements of DNA hybridization in solution," *Biochemistry (N.Y.)*, vol. 32, no. 12, pp. 3095-3104, 1993.

[142] X. Wu and B. R. Brooks, "Self-guided Langevin dynamics simulation method," *Chemical Physics Letters*, vol. 381, no. 3-4, pp. 512-518, 2003.

[143] T. Darden, D. York and L. Pedersen, "Particle mesh Ewald: An N [center-dot] log(N) method for Ewald sums in large systems," *J.Chem.Phys.*, vol. 98, no. 12, pp. 10089-10092, 1993.

[144] J. Ryckaert, G. Ciccotti and H. J. C. Berendsen, "Numerical integration of the cartesian equations of motion of a system with constraints: molecular dynamics of n-alkanes," *Journal of Computational Physics*, vol. 23, no. 3, pp. 327-341, 1977.

[145] G.M. Giambasu, T. Luchko, D. Herschlag, D.M. York and D.A. Case, "Ion counting from explicit-solvent simulations and 3D-RISM," *Biophys.J.*, vol. 106, no. 4, pp. 883-894, 2014.

[146] W. Yang, R. Bitetti-Putzer and M. Karplus, "Free energy simulations: Use of reverse cumulative averaging to determine the equilibrated region and the time required for convergence," *J.Chem.Phys.*, vol. 120, no. 6, pp. 2618-2628, 2004.

[147] K. Coutinho, R. Rivelino, H. George and S. Canuto, "The sequential QM/MM method and its applications to solvent effects in electronic and structural properties of solutes," *Solvation Effects on Molecules and Biomolecules*, pp. 158-189, 2008.

[148] N. J. English and E. T. Clarke, "Molecular dynamics study of CO2 hydrate dissociation: Fluctuation-dissipation and non-equilibrium analysis," *J.Chem.Phys.*, vol. 139, no. 9, 2013.

[149] A. Onufriev, D. Bashford and D.A. Case, "Exploring Protein Native States and Large-Scale Conformational Changes with a Modified Generalized Born Model," *Proteins: Structure, Function and Genetics*, vol. 55, no. 2, pp. 383-394, 2004.

[150] M. F. Sanner, A. J. Olson and J. Spehner, "Reduced surface: An efficient way to compute molecular surfaces," *Biopolymers*, vol. 38, no. 3, pp. 305-320, 1996.

[151] W. L. Jorgensen, D. S. Maxwell and J. Tirado-Rives, "Development and testing of the OPLS all-atom force field on conformational energetics and properties of organic liquids," *J.Am.Chem.Soc.*, vol. 118, no. 45, pp. 11225-11236, 1996.

[152] W. L. Jorgensen, J. Chandrasekhar, J. D. Madura, R. W. Impey and M. L. Klein, "Comparison of simple potential functions for simulating liquid water," *J.Chem.Phys.*, vol. 79, no. 2, pp. 926-935, 1983.

[153] J. A. Wagoner and N. A. Baker, "Assessing implicit models for nonpolar mean solvation forces: The importance of dispersion and volume terms," *Proc.Natl.Acad.Sci.U.S.A.*, vol. 103, no. 22, pp. 8331-8336, 2006.

[154] R. M. Levy, L. Y. Zhang, E. Gallicchio and A. K. Felts, "On the nonpolar hydration free energy of proteins: Surface area and continuum solvent models for the solute-solvent interaction energy," *J.Am.Chem.Soc.*, vol. 125, no. 31, pp. 9523-9530, 2003.

[155] Z. Lin, T. Strother, W. Cai, X. Cao, L. M. Smith and R. J. Hamers, "DNA attachment and hybridization at the silicon (100) surface," *Langmuir*, vol. 18, no. 3, pp. 788-796, 2002.

[156] "nanoFAB – Fabrication and Characterization Center" *ualberta.ca,* [Online] Available: https://www.nanofab.ualberta.ca/. [Accessed: Mar. 1, 2014]

[157] "ShipleyBPR™ Phototstripper" *dow.com*, [Online]. Available: https://www.dow.com/en-us/markets-and-solutions/products/SHIPLEYBPR/SHIPLEYBPRPhotostripper. [Accessed: Jan. 14, 2018].

[158] H. Khaleel, H. Al-Rizzo and A. and Abbosh, "Design, Fabrication, and Testing of Flexible Antennas, Advancement" in *Microstrip Antennas with Recent Applications*, InTech, 2013.

[159] "Solitec" *solitec-wp.com,* [Online]. Available: http://www.solitec-wp.com/. [Accessed: Mar. 1, 2014]

[160] "Cost Effective Equipment" *costeffectiveequipment.com* [Online] Available: http://www.costeffectiveequipment.com. [Accessed: Jan. 14, 2018]

[161] M. J. M. Vugts, M. F. A. Eurlings, L. J. F. Hermans and H. C. W. Beijerinck, "Si/XeF2 etching: Reaction layer dynamics and surface roughening," *Journal of Vacuum Science and Technology A: Vacuum, Surfaces and Films*, vol. 14, no. 5, pp. 2780-2789, 1996.

[162] S. Onclin, B. J. Ravoo and D. N. Reinhoudt, "Engineering silicon oxide surfaces using self-assembled monolayers," *Angewandte Chemie - International Edition*, vol. 44, no. 39, pp. 6282-6304, 2005.

[163] R. G. Nuzzo and D. L. Allara, "Adsorption of bifunctional organic disulfides on gold surfaces," *J.Am.Chem.Soc.*, vol. 105, no. 13, pp. 4481-4483, 1983.

[164] M. E. McGovern, K. M. R. Kallury and M. Thompson, "Role of solvent on the silanization of glass with octadecyltrichlorosilane," *Langmuir*, vol. 10, no. 10, pp. 3607-3614, 1994.

[165] W. A. ZISMAN, "Relation of the Equilibrium Contact Angle to Liquid and Solid Constitution,", vol. 43, pp. 1-51, 1964.

[166] "ramé-hart Contact Angle" *ramehart.com* [Online]. Available: http://www.ramehart.com/contactangle.htm. [Accessed: Mar. 1, 2014]

[167] S. Krummacher and D.D. Sarma, "XPS studies of the oxidation of USi compounds," *Surf Sci*, vol. 178, no. 1-3, pp. 842-849, 1986.

[168] G. N. Raikar, C. Klauber and S. M. Thurgate, "Auger and XPS study of band structure of zinc phosphide," *Surf Sci*, vol. 177, no. 3, pp. L1040, 1986.

[169] P. E. Vickers, M. E. Turner, M. Abel and J. F. Watts, "The interaction of organic molecules with carbon fibre surfaces: A ToF-SIMS study," *Composites Part A: Applied Science and Manufacturing*, vol. 29, no. 9-10, pp. 1291-1304, 1998.

[170] P. Fiorani, G. Margutti, G. Mariani, S. Matarazzo and G. Moccia, "TOF-SIMS: A tool for material characterisation, process control and improvement in a wafer fab," in *Proceedings of SPIE - The International Society for Optical Engineering*, vol. 3509, pp. 221-227, 1998.

[171] J. E. Hobbie, R. J. Daley and S. Jasper, "Use of nuclepore filters for counting bacteria by fluorescence microscopy," *Appl. Environ. Microbiol.*, vol. 33, no. 5, pp. 1225-1228, 1977.

[172] "Alexa Fluor dye 546" *thermofisher.com* [Online]. Available: https://www.thermofisher.com/us/en/home/life-science/cell-analysis/fluorophores/alexa-fluor-546.html. [Accessed: Jan. 14, 2018]

[173] C. W. Oatley, "The early history of the scanning electron microscope," *J. Appl. Phys.*, vol. 53, no. 2, pp. 13, 1982.

[174] D. A. Dehlinger, B. D. Sullivan, S. Esener and M. J. Heller, "Electric field assisted assembly of functionalized quantum dots into multiple layer thin films," in *2006 NSTI Nanotechnology Conference and Trade Show - NSTI Nanotech 2006 Technical Proceedings*, vol. 1, pp. 389-392, 2006.

[175] M. J. Heller, D. Dehlinger, B. Sullivan and S. Esener, "Electric field process for the fabrication of higher order structures form biomolecule derivatized nanoparticles (#1030)," in *2007 NSTI Nanotechnology Conference and Trade Show - NSTI Nanotech 2007, Technical Proceedings*, vol. 1, pp. 269-270, 2007.

[176] R. Peytavi, L. Tang, F. R. Raymond, K. Boissinot, L. Bissonnette, M. Boissinot, F. J. Picard, A. Huletsky, M. Ouellette and M.G. Bergeron, "Correlation between microarray DNA hybridization efficiency and the position of short capture probe on the target nucleic acid," *BioTechniques*, vol. 39, no. 1, pp. 89-96, 2005.

[177] L. De Silva, L. Yao, Y. Wang and S. Xu, "Well-defined and sequence-specific noncovalent binding forces of DNA," *J Phys Chem B*, vol. 117, no. 25, pp. 7554-7558, 2013.

[178] K. Rück-Braun, M. A. Petersen, F. Michalik, A. Hebert, D. Przyrembel, C. Weber, S. A. Ahmed, S. Kowarik and M. Weinelt, "Formation of carboxy- and amide-terminated alkyl monolayers on silicon(111) investigated by ATR-FTIR, XPS, and X-ray scattering: Construction of photoswitchable surfaces," *Langmuir*, vol. 29, no. 37, pp. 11758-11769, 2013.

[179] H. Blasius, "Grenzschichten in flüssigkeiten mit kleiner reibung," *Z.Math.Phys.*, vol. 56, pp. 1-37, 1908.

[180] S. Bhattacharjee and S. Sarma, "Numerical analysis of laminar incompressible viscous flow over a flat plate," *ESTIJ*, vol. 3, no. 1, pp. 143, 2013.

[181] O. Reynolds, "An experimental investigation of the circumstances which determine whether the motion of water shall be direct or sinuous, and of the law of resistance in parallel channels," *Philosophical Transactions of the Royal Society*, vol. 174, pp. 935, 1883.

[182] K. J. Laidler, J. H. Meiser, Physical chemistry Benjamin/Cummings Pub. Co., 1982.

[183] T. Olsen, *Using Biomolecular Recognition to Selectively Self-Assemble Microscale Components onto Patterned Substrates*. Edmonton: Aka, 2014.

[184] Z. Wang, X. Zeng, Y. Deng, N. He, Q. Wang and J. Huang, "Molecular dynamics simulations of end-tethered single-stranded dna probes on a silica surface," *J.Nanosci.Nanotechnol.*, vol. 11, no. 10, pp. 8457-8468, 2011.

[185] M. Castronovo, S. Radovic, C. Grunwald, L. Casalis, M. Morgante and G. Scoles, "Control of steric hindrance on restriction enzyme reactions with surface-Bound DNA nanostructures," *Nano Letters*, vol. 8, no. 12, pp. 4140-4145, 2008.

[186] J. Man and J. Fu, “Biomolecule separation by steric hindrance using nanofluidic filters,” in *Annual International Conference of the IEEE Engineering in Medicine and Biology - Proceedings*, vol. 26 IV, pp. 2611-2614, 2004.

Appendix I: MD simulation details

1. Building the ds-DNA structure using NAB

AMBER command:

```
nab 10mer.nab
./a.out
```

Input File: *10mer.nab*

```
molecule m;
m = bdna("ttggtgatcc");
putpdb("10mer.pdb", m, "-wwpdb");
```

2. Preparing topology files using Xleap

AMBER command:

```
xleap -s -f $AMBERHOME/dat/leap/cmd/leaprc.ff99bsc0
dna =loadpdb "10mer.pdb"
addions dna Na+ 0
solvateoct dna TIP3PBOX 8.0
saveamberparm dna complex.prmtop complex.inpcrd
```

3. Energy Minimization of the solvated ds-DNA

AMBER command:

```
sander -O -i min1.in -o min1.out -p complex.prmtop -c
complex.inpcrd -r min1.rst -ref complex.inpcrd
```

Input File: *min1.in*

```
Minimisation: Holding the solute fixed
&cntrl
 IMIN=1,
 MAXCYC=1000,
 NCYC=500,
 NTB=1,
 NTR=1,
 CUT=10
/
Hold DNA fixed
500.0
RES 1 10
```

```
END
END
```

4. MD (Heating) with restraints on solute

AMBER command:

```
sander -O -i heat.in -o heat.out -p complex.prmtop -c min1.rst -r
heat.rst -x heat.mdcrd -ref min1.rst
```

Input File: *heat.in*

```
Molecular Dynamics with restraints in the solute: First
Equilibration step to adjust the system to temp of 298.15 K for
20ps
&cntrl
 IMIN=0,
 IREST=0,
 NTX=1,
 NTB=1,
 CUT=10,
 NTR=1,
 NTC=2,
 NTF=2,
 TEMPI=0.0,
 TEMP0=298.15,
 NTT=3,
 GAMMA_LN=2.0,IG=-1,
 NSTLIM=10000, DT=0.002,
 NTPR=100, NTWX=100, NTWR=1000
/
Keep DNA fixed with weak restraints
200.0
RES 1 10
END
END
```

5. MD (Density) with weaker restraints on solute

AMBER command:

```
sander -O -i density.in -o density.out -p complex.prmtop -c
heat.rst -r density.rst -ref heat.rst -x density.mdcrd -inf
mdinfo
```

Input File: *density.in*

```
MD Equilibration step to adjust the pressure to 1 atm with
restraints on solute for 100ps
&cntrl
 IMIN=0,
 IREST=1,
```

```
 NTX=7,
 NTB=2,
 PRES0=1.0,
 NTP=1,
 TAUP=2.0,
 CUT=8,
 NTR=1,
 NTC=2,
 NTF=2,
 TEMPI=298.15,
 TEMP0=298.15,
 NTT=3,
 GAMMA_LN=2.0,IG=-1,
 NSTLIM=10000, DT=0.002,
 NTPR=100,
 NTWX=100,
 NTWR=1000
/
Keep DNA fixed with weak restraints
10.0
RES 1 10
END
END
```

6. MD Equilibration on the whole system

AMBER command:

```
sander -O -i equil.in -o equil.out -p complex.prmtop -c
density.rst -r equil.rst -x equil.mdcrd -inf mdinfo
```

Input File: *equil.in*

```
MD Equilibration step to adjust the pressure to 1 atm without
restraints on solute for 100ps
&cntrl
 IMIN=0,
 IREST=1,
 NTX=7,
 NTB=2,
 PRES0=1.0,
 NTP=1,
 TAUP=2.0,
 CUT=8,
 NTR=0,
 NTC=2,
 NTF=2,
 TEMPI=298.15,
 TEMP0=298.15,
 NTT=3,
 GAMMA_LN=2.0,IG=-1,
```

```
 NSTLIM=50000, DT=0.002,
 NTPR=100,
 NTWX=100,
 NTWR=1000
/
```

7. MD Production simulation

AMBER command:

```
sander -O -i prod.in -o prod.out -p complex.prmtop -c equil.rst -
r prod.rst -x prod.mdcrd -inf mdinfo
```

Input File: *prod.in*

```
MD Production step to adjust the pressure to 1 atm without
restraints on solute for 1ns
&cntrl
 IMIN=0,
 IREST=1,
 NTX=7,
 NTB=2,
 PRES0=1.0,
 NTP=1,
 TAUP=2.0,
 CUT=8,
 NTR=0,
 NTC=2,
 NTF=2,
 TEMPI=298.15,
 TEMP0=298.15,
 NTT=3,
 GAMMA_LN=2.0,IG=-1,
 NSTLIM=500000, DT=0.002,
 NTPR=100,
 NTWX=100,
 NTWR=1000
/
```

Appendix II: Post processing MD trajectories details

1. Extracting trajectories from MD Production simulation

AMBER command:

```
perl $AMBERHOME/bin/mm_pbsa.pl extract_coords.mmpbsa >
extract_coords.log
```

Input File: *extract_coords.mmpbsa*

```
##########################################################
PREFIX                  snapshot
PATH                    ./
COMPLEX                 1
RECEPTOR                1
LIGAND                  1
COMPT                   ./complex.prmtop
RECPT                   ./receptor.prmtop
LIGPT                   ./ligand.prmtop
GC                      1
AS                      0
DC                      0
MM                      0
GB                      0
PB                      0
MS                      0
NM                      0
##########################################################
@MAKECRD
BOX                     YES
NTOTAL                  9255
NSTART                  1
NSTOP                   5000
NFREQ                   20
NUMBER_LIG_GROUPS       1
LSTART                  328
LSTOP                   651
NUMBER_REC_GROUPS       1
RSTART                  1
RSTOP                   327
##########################################################
@TRAJECTORY
TRAJECTORY              ./../../prod.mdcrd
#TRAJECTORY              ./prod3.mdcrd
#TRAJECTORY              ./prod4.mdcrd
##TRAJECTORY              ./prod2.mdcrd
##########################################################
```

```
@PROGRAMS
#############################################################
```

2. Calculating Binding energies from extracted snapshots

AMBER command:

```
perl $AMBERHOME/bin/mm_pbsa.pl binding_energy.mmpbsa >
binding_energy.log
```

Input File: *binding_energy.mmpbsa*

```
#############################################################
@GENERAL
PREFIX                  snapshot
PATH                    ./
COMPLEX                 1
RECEPTOR                1
LIGAND                  1
COMPT                   ./../complex2.prmtop
RECPT                   ./../receptor2.prmtop
LIGPT                   ./../ligand2.prmtop
GC                      0
AS                      0
DC                      0
MM                      1
GB                      1
PB                      1
MS                      1
NM                      1
#############################################################
@PB
PROC                    2
REFE                    0
INDI                    1.0
EXDI                    80.0
SCALE                   2
LINIT                   1000
PRBRAD                  1.4
ISTRNG                  0.0
RADIOPT                 0
NPOPT                   1
CAVITY_SURFTEN          0.0072
CAVITY_OFFSET           0.00
SURFTEN                 0.0072
SURFOFF                 0.00
#############################################################
@MM
DIELC                   1.0
#############################################################
@GB
```

```
IGB                     2
GBSA                    1
SALTCON                 0.00
EXTDIEL                 80.0
INTDIEL                 1.0
SURFTEN                 0.0072
SURFOFF                 0.00
#########################################################
@MS
PROBE                   0.0
#########################################################@NM
DIELC                   1.0
MAXCYC                  1
DRMS                    5.0
#################################################
@PROGRAMS
#########################################################
```

3. Calculating Binding energy using 3D-RISM-KH

Command used:

```
./rism3d dsDNA
```

Input File: *dsDNA.inp*

```
'm'    'KH'  'NON-PERIODIC'  'OLD' 'ALL'
 'water_25C.xvv'
   2.5 1.0  1.0e-30  1.0e-8
   10   0.5   1.0e-4
  100    1    10000
  128.0 128.0 128.0
  256   256   256
651   sites'NO-CHARGE' in DNA
0.4422    0.0000    0.0000     35.703  24.897  27.911   !     1   H5T   DT5   HO
..............
1.0000    3.3284    0.0028     40.400  20.366  34.350   !   651  Na+    Na+   IP
```

Solvent File used: *water_25C.xvv*

Appendix III: Error Analysis

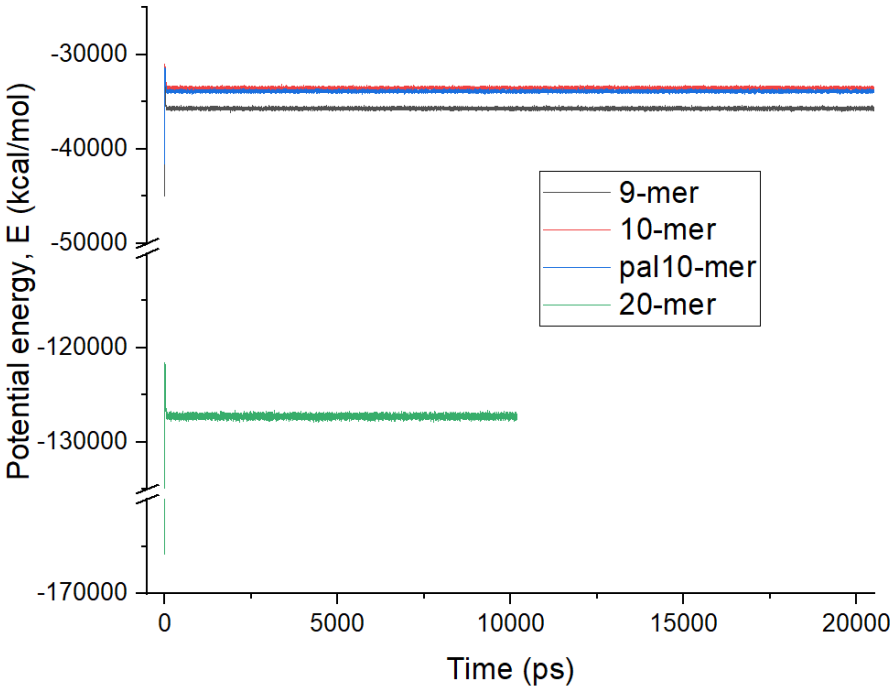

Figure A: Potential energy plots after the MD simulation production run of 20 ns for 9-mer, 10-mer, pal10-mer and 10 ns run for 20-mer ds-DNA used for the theoretical comparison study confirming convergence of potential energy and no systematic error during the MD simulation.

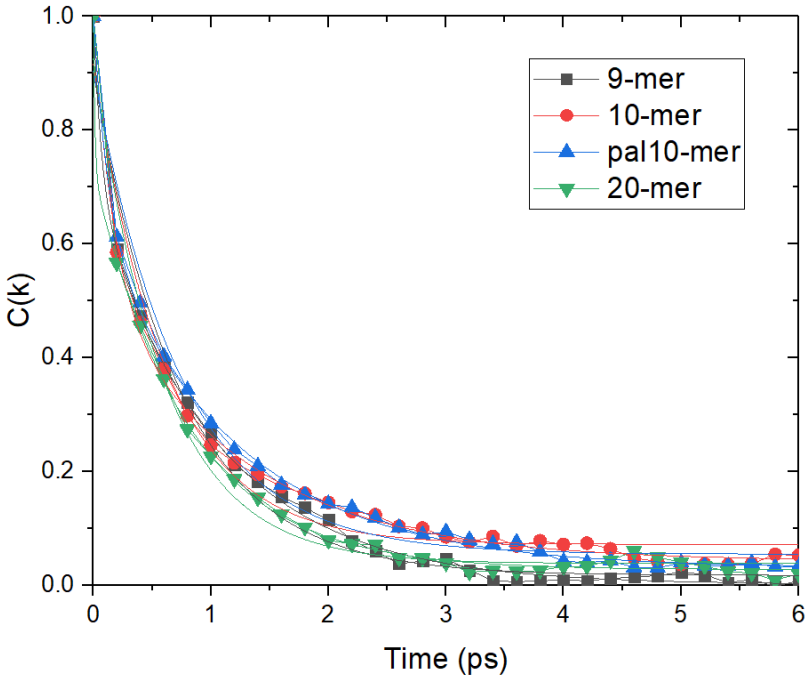

Figure B: Distribution of the correlation coefficient with correlation time intervals chosen to estimate the statistically converge interval for all ds-DNA strands configurations obtained from MD simulation.

Appendix IV: Matlab script for DNA Melting curve

```
% create an empty structure to hold the results
ideal = struct();

% temperature axis in Kelvin: 100 points (0-99 C)
ideal.temperature = (0:99) + 273.15;

ideal.deltaS = -81;                    % cal/mol

ideal.deltaH = -50.85E3;                   % cal/(mol K)
ideal.concentration = 1E-15;

% call DnaFraction function
% arguments: concentration, temperature vector, delta S, delta H

ideal.ds-DNAFraction = DnaFraction(ideal.concentration,
ideal.temperature, ...
                                ideal.deltaS, ideal.deltaH);

%plotting the curve Temperture vs DNA Fraction
plot(ideal.temperature, ideal.ds-DNAFraction);
title('Ideal DNA Melting Curve');
xlabel('Temperature (K)');
ylabel('ds-DNA Fraction');
```

%Function DnaFraction

```
% Returns the fraction of ds-DNA in a solution containing equal
concentrations
% of two complementary DNA oligos as a function of total DNA
concentration,
% temperature, entropy change, and enthalpy change.
% Gas constant is an optional parameter.
%
% USAGE: f = DnaFraction(Ct, T, DeltaS, DeltaH, <GasConstant>)
% RETURN VALUE: fraction of ds-DNA
%
% Default units are molar, Kelvin, cal/mole, and cal/(mole-
Kelvin). For
% other unit systems, supply the appropriate value of R in the
optional
% fifth parameter. The default value is 1.987 cal/(degree K *
mole).

function f = DnaFraction(Ct, T, DeltaS, DeltaH, GasConstant)
```

```
% Gas constant
if(nargin < 5)              % determine if caller supplied R
value or not
    R = 1.987;              % set to default: cal/(degree K *
mole)
else
    R = GasConstant;        % otherwise use caller's value
end

% Compute Ct * Keq
CtKeq = Ct * exp(DeltaS / R - DeltaH ./ (R * T));

%now compute f
f = (1 + CtKeq - sqrt(1 + 2 * CtKeq)) ./ CtKeq;
```